AN INVESTIGATION INTO FLUID FLOW AND HEAT TRANSFER OF HIGH FREQUENCY SYNTHETIC JETS FOR ELECTRONICS COOLING

A Dissertation

by

Omidreza Ghaffari

Submitted to the

Graduate School of Sciences and Engineering

In Partial Fulfillment of the Requirements for

the Degree of

Doctor of Philosophy

in the

Department of Mechanical Engineering

Özyeğin University

April 2016

AN INVESTIGATION INTO FLUID FLOW AND HEAT TRANSFER OF HIGH FREQUENCY SYNTHETIC JETS FOR ELECTRONICS COOLING

Approved by:

Professor Mehmet Arik, Advisor
Department Mechanical
Engineering
Özyeğin University

Associate Professor Stephen A.Solovitz
Department of Mechanical
Engineering
Washington State University Vancouver

Associate Professor Göksenin Yaralıoğlu
Department of Electrical
Engineering
Özyeğin University

Professor Ali Koşar
Department of Mechatronics
Engineering
Sabanci University

Assistant Professor Altuğ Başol
Department of Mechanical
Engineering
Özyeğin University

Date Approved: 30 March 2016

To my wife Azadeh,

To our son Artin,

& to my parents

ABSTRACT

Modern electronics have been decreasing in size for decades, so their cooling systems must continually improve in efficiency too. In particular, compactness is vital, which is challenging because typical thermal management uses relatively large fans and heat sinks. For more advanced liquid cooling, additional coolant and structure are required, somewhat counteracting the improvement with liquid heat transfer. Ideally, thermal management should be economical, low volume, and localized on the powered devices. Fortunately, some recent advances in synthetic jet devices may provide a potential solution.

Synthetic jets use an oscillating structure near an orifice, which produces a periodic jet outflow and sink inflow. When averaging over time, this leads to an axial jet, which can be directed towards a powered device. Unlike traditional impingement cooling, the jet is supplied by ambient fluid, as opposed to an additional coolant.

We developed a series of thermal, structural and flow experimental setups in order to test two distinct in house manufactured synthetic jet devices along with one commercial ultrasonic jet.

The in house manufactured slot synthetic jets used in this study have a different topology than the previous slot actuators, sandwiching two circular disks together. While a large number of earlier devices placed their orifices normal to the oscillating piezoelectric disk, this new approach placed the orifice along the circumference of the sandwiched pair. Hence, the jet direction was perpendicular to the piezoelectric disk deflection.

We later performed a series of CFD simulations to examine the performance of in-house made novel slot synthetic jet and validated it with experimental data. Along with measurements of deflection and thermal performance, we used time-averaged and phase-locked PIV to study the flow physics and their effects on heat transfer. We focused on synthetic jet behavior at several

frequencies, both at and away from resonant conditions, which may help in selecting device conditions with lower acoustic noise.

For a slot synthetic jet the degradation of heat transfer for small jet-to-surface spacings, like $H/D_h = 2$, was due to the reduced growth of the vortices. In addition, there was re-entrainment of warm air next to the impinging plate by the vortex back into the jet flow, and some warm fluid was sucked back into the orifice.

In a slot jet case the heat transfer is maximum for a jet-to-surface spacing for $5 \leq H/D_h \leq 10$, which is associated with flow dominated by coherent vortices that grow to full strength before detachment or impact with the wall. At the diaphragm resonant condition and below, the flow structure was similar at all phases, with a single vortex present between the orifice and the wall. This response suggests that there is a critical jet-to-surface spacing for this behavior, $H_{crit} = U_o/2f$, which should relate to the optimal thermal condition. By tuning the actuator frequency to the wall spacing, the vortices can reach the wall in phase at the end of the outstroke. When well-tuned, the thermal response is governed primarily by Reynolds number. There is a superior cooling performance at high Stokes number with the same Re_{U0} number.

The maximum cooling performance of a circular synthetic jet at the close heater to jet distance was not observed at the structural frequency of the jet where the maximum velocity occurs. It occurs at frequencies greater than the structural frequency.

Based on efficiency (COP) comparison, a slot synthetic jet has a better cooling performance compared to a circular jet and ultrasonic micro-blower due to the difference in the flow physics of the two jets so the slot synthetic jet is a better candidate for electronics cooling applications. For the micro blower jet the preferred

operating frequency of the piezoelectric actuator occurs at an ultrasonic frequency of 25 kHz, meaning that this device can function with low noise. The micro-blower axial velocity profile shows similar behavior to high Reynolds number turbulent free jets in the far field, including a self-similar profile. But in the near field, there has been a significant deviation with turbulent free jets. The average Nusselt number increases sharply up to H/D = 10, and then it shows a gradual increase till H/D=15. There is a fairly flat maximum region for $15 \leq H/D \leq 30$, followed by a gradual decay for $H/D >$ 30. The heat transfer increases more than three times by moving the jet from H/D = 2 to H/D = 10. This reveals that the jet performance is highly sensitive to the jet-to-surface spacing. The jet cooling performance is sensitive to the frequency, though there is a 1 kHz wide band of similar thermal response about the peak. The coefficient of performance at the best operating heat transfer condition is about 2, which is less than the value of 14 seen for a slot synthetic jet. Thus, while this micro-blower can greatly reduce noise, it has a significant performance penalty.

ÖZETÇE

Modern elektroniklerin boyutu yüzyıllardır küçülmekte dolayısıyla soğutma sistemleri de sürekli verimliliğini geliştirmek zorundadır. Özellikle, tipik olarak kullanılan büyük boyutlu ısı atacakları ve fanlardan dolayı zorlayıcı olsa da kompaktlık çok önemlidir. Daha ileri sıvı soğutma için sıvı ısı transferini geliştirebilmek için ek soğutucu sıvı ve yapı gerekmektedir. İdeal olarak, ısıl yönetim tasarımı ekonomik, küçük boyutlu olmalı ve güç cihazlarının üzerinde konumlandırılmalıdır. Bu durumlar göz önüne alındığında sentetik jetler uygun bir çözüm oluşturmaktadır.

Periyodik jet dış akış ve alıcı (sink) iç akış üreten, sentetik jetler ağız (orifice) yanında salınımlı bir yapı gösterirler. Zamanla, güç kaynağına doğru eksenel bir jet oluştururlar. Jetler çarpmalı soğutmalardan farklı olarak ortamdaki akışkan ile beslenirler ve ek bir soğutucu akışkana ihtiyaç duymazlar.

Kendi üretimimiz olan iki ayrı sentetik jet ile bir ticari ultrasonik jeti test etmek için bir seri termal, yapısal ve akış deney düzeneği geliştirdik. Bu çalışmada, önceki slot aktüatörlerden farklı topolojiye sahip olan, iki dairesel diski sıkıştırarak bir araya getiren kendi üretimimiz slot jetler kullanıldı. Önceki cihazların büyük çoğunluğunda ağızlar (orifice) salınımlı piezoelektrik diskin yüzeyine dik olarak yerleştirilirken, bu yeni yaklaşım ağzı, sıkıştırılan disk çiftinin çevresi boyunca yerleştirir. Bu yüzden, jet yönü piezoelektrik disk eğilimine (deflection) diktir.

Daha sonra, bu yeni slot sentetik jetlerimizin performansını incelemek ve deneysel verilerle doğrulamak için, bir seri HAD simülasyonları gerçekleştirdik. Defleksiyon ve termal performans ölçümleri ile birlikte, akış fiziği ve bunların ısı transferi üzerindeki etkisini çalışabilmek adına, zamana göre ortalaması alınmış ve faz kilitlemeli PIV tekniği kullandık. Düşük akustik sesli cihaz seçimlerinde yardımcı olabilecek, rezonant koşullarında ve uzağında birçok frekansta jet davranışlarına odaklandık.

Girdapların büyümesinin azalmasından dolayı, H/D_h = 2 gibi azalmış girdaplar (vorteksler) küçük jet – yüzey aralıkları için slot sentetik jetin ısı transferinde bir azalma gerçekleşmesine sebep olmuştur. Buna ek olarak, girdabın jet akışına geri dönmesiyle, sıcak hava yeniden çarpma levhasının yanına sürüklenir ve sıcak havanın bir kısmı ağzın içine geri emilir.

Bir slot jette ısı transferi duvardan ayrılmadan veya etkileşmeden önce düzenli olarak büyüyen uyumlu girdaplar tarafından, domine edilen akışla ilişkilendirilmiş $5 \leq H/D_h \leq 10$ aralığında olan jet- yüzey boşluğu için maksimum değere ulaşır. Diyaframın rezonant koşulunda ve altında, akış yapısı tüm fazlarda aynıdır. Ağız ve duvar arasında, yalnızca bir tek girdap vardır. Bu yanıta göre, bu davranış için kritik bir jet- yüzey aralığı, $H_{crit} = U_o/2f$ vardır. Bu da en uygun termal durum ile bağdaştırılmalıdır. Duvar aralığı için aktüatör ayarlanarak, girdaplar outstroke – akışkanın jet dışına itilmesi sonundaki fazda duvara ulaşabilirler. İyi ayarlandığında, ısıl yanıt öncelikli olarak Reynolds sayısı tarafından bulunur. Aynı Re_{U0} sayısı ve yüksek Stokes sayısında üstün soğutma performansı elde edilir.

Yakın ısıtıcı jet mesafelerinde, jetin maksimum hıza ulaştığı yapısal frekansta, dairesel sentetik jetin maksimum soğutma performansı gözlemlenmez. Bu durum yapısal frekanstan daha büyük frekanslarda gözlemlenmektedir.

Verim katsayısı karşılaştırması baz alınarak; slot sentetik jet dairesel jet ve mikro üfleyici ile karşılaştırıldığında iki jetin de akış fiziğinde farklılık olmasına rağmen daha iyi soğutma performansına sahiptir, bu yüzden slot sentetik jet elektronik soğutma uygulamaları için daha iyi bir adaydır. Mikro üfleyici jet için, tercih edilen piezoelectric uyarıcının işletim frekansı 25 kHz ultrasonik frekansta gerçekleşir, bu cihazın düşük sesli görev yaptığı anlamına gelir. Kendi benzer profilini içeren mikro üfleyici eksenel

hız profili yüksek Reynold sayılı türbülanssız uzun menzilli jetler ile benzer özellik gösterir. Fakat kısa menzilde türbülanssız jetlerde kayda değer sapmalar oluşur. Ortalama Nusselt sayısı H/D = 10'a kadar hızla artar ve sonra H/D=15'e kadar kademeli bir artış gösterir. $15 \leq H/D \leq 30$ arasında tamamen stabil maksimum bir aralık vardır. H/D > 30'den büyük olan koşullarda ise ortalama Nusselt sayısı kademeli olarak azalmaya devam eder. Jetin H/D = 2'den H/D = 10'a hareketiyle ısı transferi üç katından fazlaya çıkar. Bu durum gösteriyor ki jet performansı jet-yüzey aralığına yüksek derecede duyarlıdır. En yoğun çalışma koşulunda, 1 kHz geniş banda sahip benzer ısıl yanıtın olmasına karşın, jetin soğutma performansı frekansa duyarlıdır. En iyi ısı transferi çalışma koşulunda, performans katsayısı, slot sentetik jetlerde görülen 14 değerinden küçük ve 2 civarındadır. Bu nedenle, bu mikro üfleyici gürültüyü büyük ölçüde giderebilecekken, önemli bir performans hatasına da yol açabilir.

ACKNOWLEDGMENT

Financial support for the research project was provided by a Turkish National Science Foundation (TUBITAK) under the contract number 112M154. First, I would like to thank to my advisor, Professor Mehmet Arik for his continual guidance and support giving me the motivation and encouragement that made this work possible.

Many thanks to Professor Steven A.Solovitz for his guideness and hospitality during my short visit to Washington State University.

I would also like to express my gratitude especially to all the thesis committee members and Dr. Mehmet Baris Dougroz, Enes Tamdogan, Muhammad Ikhlaq and to other members of ART group.

Finally, thanks go to my family and friends, from the USA, Turkey and from Iran, for always encouraging me to pursue my interests and for making that pursuit possible, Special thanks to great teacher of every time Mr. Mohammad Bahmanbeigi (Founder of tribal education and winner of UNESCOU prize) who educated hundred thousands of children in Iran and provide them the new way of thinking and life.

Table of contents

List of Figures

List of Tables

NOMENCLATURE

A	Area of the orifice	(m^2)
c	Speed of sound	(m/s)
C_p	Pressure coefficient, $c_p = \frac{P-P_{amb}}{0.5\rho u_j^2}$	
Cf	Friction coefficient	
D	Diameter of orifice	(m)
D_h	Hydraulic diameter	(m)
E	Modulus of elasticity	(Pa)
EF	Enhancement factor	
f	frequency	(s^{-1})
f_d	Driving frequency	(s^{-1})
f_h	Helmholtz resonant frequency	(s^{-1})
Gr	Grashof number	
H	Jet to target plate spacing	(m)
h	Heat transfer coefficient	(m)
k_f	Fluid Thermal conductivity	(m)
K	Turbulent kinetic energy per unit mass	(m^2/s^2)

L	Length of heater	(m)
L_o	Jet stroke length	(m)
m	Mass	(Kg)
Nu	Nusselt number	
p	Pressure	Pa
Q_{front}	Heat coming from front surface	$kg \cdot m^2/s^3$
Q_{loss}	Heat loss	$kg \cdot m^2/s^3$
Q_{total}	Total heat removed by heater	$kg \cdot m^2/s^3$
Re	Reynolds number	
Re_j	Jet Reynolds number	
Re_{U0}	Reynolds number base on outstroke velocity	
Ri	Richardson number	
r	Radius	(m)
S	Stokes number	
T	Temperature	K
t	Time	s
U	Velocity	(m/s)

V	Cavity Volume	(m^3)
W	Orifice width	(m)
x	X direction	
y	Y direction	
Z	cavity height	(m)

Greek Symbols

Γ	Circulation	(m^2/s)
Δ	Diaphragm deflection	(m)
ξ	Time period	(s)
μ	Dynamic viscosity	
υ	Kinematic viscosity	
π	Pi number	
ρ	Density	(kg/m^3)
ω	Vorticity	(S^{-1})

Subscripts

amb	Ambient
ave	Average

cl	Central
max	Maximum
p	Peak
r	Radial direction
W	Wall

CHAPTER I

INTRODUCTION

1.1Synthetic jet technology

Liquid cooling is typically applied for high-power electronics problems because of its high heat transfer coefficients. Even so, most designers would prefer to use air cooling, which has benefits such as availability, low cost, reliability, and previous understanding in implementation. As electronic components continue to shrink over time, it is critical that thermal management methods be compact. Successful cooling technology must feature a low cost, very thin profile and a small footprint area. In this regard, synthetic jet devices [1–4] may provide an effective solution.

Synthetic jets operate on the zero-net mass flow rate principle. Typically, they inhale and expel high speed working fluid through an orifice, producing a net positive momentum flow[5] (for more information about synthetic jet formation criterion please check Appendix A) . Synthetic jets have been explored for flow control, low-speed maneuvering, and propulsion for traditional propeller-driven underwater vehicles [6,7]. In addition they have been used to enhance boundary layer turbulence [8,9]. Recently, these devices have been explored for heat transfer applications. Here, the cooling may be improved in multiple ways, such as impingement of ejected vortices onto hot surfaces [10–13] and enhancement of the primary cooling methodology [14,15].

Synthetic jets are mainly compatible with miniature devices, such as those on circuit boards. In these applications, free convection is insufficient, and traditional forced convection with

fans is limited by volume and acoustic concerns. On the contrary, synthetic jets use the environmental fluid during operation, eliminating the need for complex plumbing issues [16]

Recently, He et al. [4]compared the cooling effect of a mesoscale synthetic jet to a steady impinging jet. They found that synthetic jets could provide 20% enhancement over a steady jet for the same amount of ejected mass. There was also a significant benefit when comparing performance at the same exit speed and diameter. Different numerical studies on impinging synthetic jets also concluded that synthetic jets can lead to considerable improvement of the local heat transfer from heated surfaces, as strong mixing disturbs the surface thermal boundary layer [17,18].

Synthetic jet cooling operates similar to traditional impingement cooling [19], where a jet is directed towards a heated surface. This results in stagnation flow at the surface, which produces high local heat transfer. As a result, impingement has been considered for electronics cooling, particularly at hot spots. The traditional method requires additional coolant and a pumping mechanism, which have significant volume and mass. However, a synthetic jet needs no additional coolant, simply using the surrounding fluid as it oscillates. In addition, many synthetic jet actuators require relatively low power input, with higher coefficients of performance than other air movers [2].

Although synthetic jets have some similarity to steady jets, their transient variation produces some significant differences in their behavior. Much of this deviation is related to the prominent vortex ring produced in the ejection stroke, which increases the entrainment of ambient fluid into the jet [12,16,20–22].

Because of this potential, there have been a number of heat transfer studies with synthetic jets. The initial research used pulsating jets generated by acoustic speakers, which produced convective heat transfer four times above that of natural convection alone [23,24]. During the

mid-1990s, compact piezoelectric disks were used to drive synthetic jets, and these too produced a fourfold increase in heat transfer for a cellular phone application [25]. Through modifications in actuator topology, later synthetic jets provided more significant thermal enhancement, raising the heat transfer to 10 times that of natural convection [1]. Computational results suggested that this would be increased to over 15 times [26] More recently, Persoons et al. [13]combined many synthetic jet studies into a general correlation for predicting stagnation point Nu number as a function of Re number, wall spacing, and actuator stroke length.

Cooling performance of an impinging synthetic jet is highly sensitive to the distance between the nozzle exit and the wall [2,4,12,13,18,27–29]. In the case of impinging synthetic jets, the flow structure also depends on this distance. This variable determines the propagation distance of the vortices, the level of jet confinement, and the amount of recirculation. Typically, the vortex pairs remain coherent for some distance before decaying. This distance depends on how close the impingement surface is to the orifice, H, as well as the stroke length, L_0 [12,16]], which is related to the amount of fluid ejected per stroke.

Gillepsie et al. [11] and Pavlova and Amitay [12] each experimentally studied the influence of jet-to-surface spacing on impinging synthetic jet heat transfer. In each study, the peak heat transfer occurs for a nondimensional spacing from $4 < H/D < 11$.

Pavlova and Amitay [12] conducted a thorough study of the heat transfer and fluid dynamics for an impinging, circular synthetic jet, and they used flow information to explain the thermal performance. By varying the actuator frequency and position, they found two optimal frequencies for heat transfer. At the lower frequency, the optimal heat transfer occurred for wall spacing-to-jet diameter ratios, H/D, on the order of 10. At the higher frequency, the best heat transfer occurred for closer positions, with H/D ~ 5. Using time-averaged and phase-

locked particle image velocimetry for $H/D \sim 10$, they examined how the vortex structures promoted this thermal performance at these optimal frequencies. Individual vortex rings impinged directly on the heater at the lower frequency, while they broke down into more turbulent structures at the higher frequency. Interestingly, neither frequency corresponded exactly with the resonant frequency of the actuator.

In a similar study, Valiorgue et al. [28] considered the performance for a round synthetic jet very near a wall, with H/D of 2. At this position, heat transfer is generally lower than observed further away. Here, the researchers used thermal measurements and phase-locked PIV to examine the response. By following the motion of the ejected vortex rings, they demonstrated that the vortex circulation falls off after impingement with the wall, likely reducing the heat transfer.

However, relatively few studies have considered smaller distances, where $H/D < 4$ [2,28]. Here, the cooling performance degrades by approximately 40% [2], but the fundamental mechanism for this behavior is not well understood yet.

There has been significantly less study of non-circular synthetic jets. Gillespie et al. [11] examined the thermal and flow performance for a long slot orifice, with an aspect ratio of 25. Through time-averaged PIV (particle image velocimetry), they demonstrated significant blooming of the jet about 7 slot widths downstream of the orifice, which impacted the optimal wall location. Chaudhuri et al. [30] conducted a thermal study for a range of orifice shapes, from a square to a long rectangular slot with an aspect ratio of 20. Close to the wall, they found that long aspect ratios had better thermal performance, and they suggested that a moderate aspect ratio of around 6 is preferred. Hot-wire anemometry and smoke visualization techniques were also used to support this conclusion.

Very recently, Ghaffari et al. [2] examined the thermal performance of an impinging slot synthetic jet with an aspect ratio of 8. The device enhanced the heat transfer by a factor of 14 times that of natural convection at its optimal frequency and wall spacing, exceeding the performance for a comparably scaled round jet. However, when operating at other frequencies, the slot jet had a more rapid decrease in heat transfer than the round jet, showing more sensitivity to this variable. Unsteady simulations of this slot jet confirmed the optimal frequency and position, and they demonstrated that the heat transfer was non-uniform on the surface due to the locations of impinging vortices [17,31].

There are a number of jet constructions available by different research groups. Figure 1 depicts an in house designed and manufactured slot synthetic jet called ART 4000s impinging on a flat vertical heater, which has been utilized in this study. The slot synthetic jet used in the present study consists of a piezoelectric actuator and a circular plate, which are attached along the most of their perimeter using an elastomeric material. In one small section of the perimeter, there is a rectangular opening, which has an aspect ratio of 8. This jet used a different topology than the previous slot actuators, sandwiching two circular disks together. While earlier devices placed their orifices normal to the oscillating piezoelectric disk, this newer actuator placed the orifice along the circumference of the sandwiched pair. Hence, the jet direction was perpendicular to the piezoelectric disk deflection.

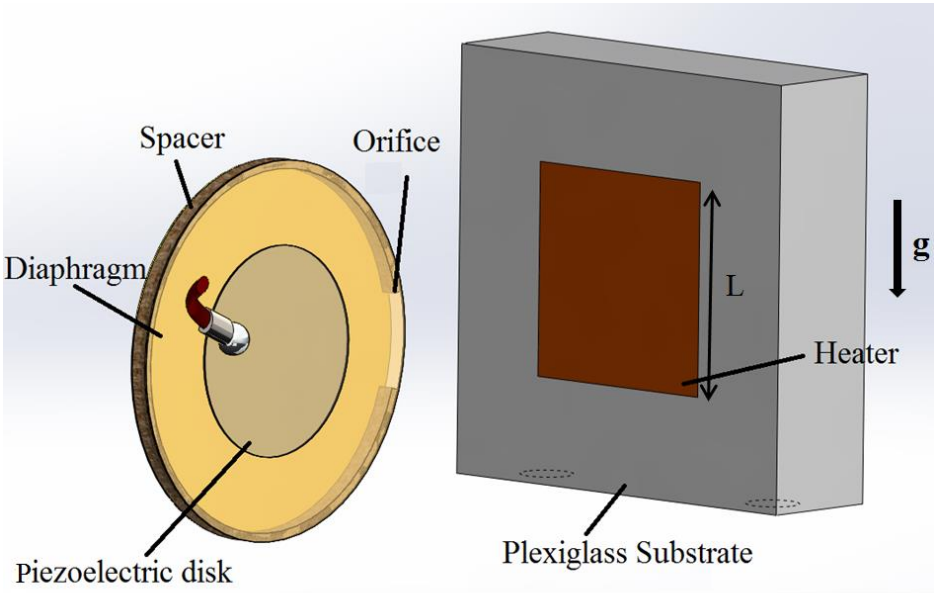

Figure 1.Isometric view of an impinging slot synthetic jet(ART 4000s) used in this study

This rectangular orifice is the sole location where internal fluid may interact with the outside environment. Figure 2 shows an in house designed and manufactured central orifice called ART4000 synthetic jet that is formed by a piezoelectric actuator and an orifice plate, attached with an elastomeric material applied along the perimeter of the cavity. The Orifice is the only path to have communication with the external ambient. While orifice may have different shapes and sizes, it strongly affects the fluid-structure interaction in the synthetic jet chamber resulting in a poor or strong thermal performance.

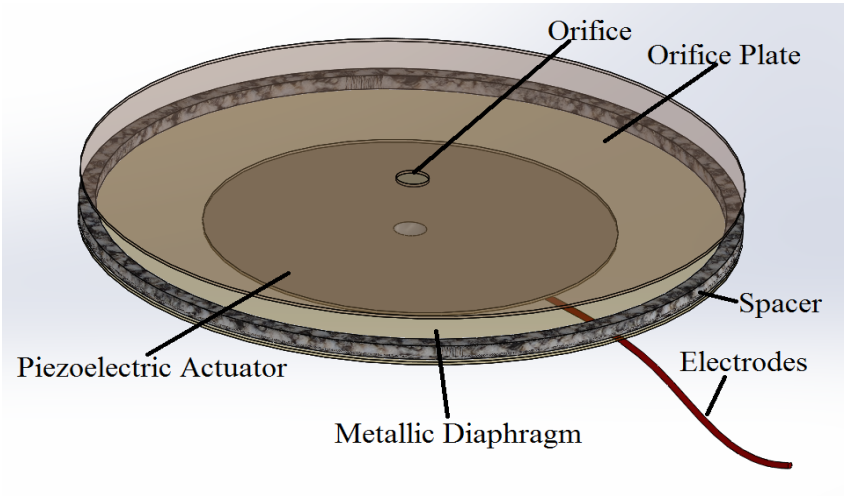

Figure 2 .Schematic diagram of a circular orifice synthetic jet (ART4000) .

In operation, the piezoelectric material is excited by an AC power source at a specific frequency, which inhales and exhales air at the opening. Through appropriate selection of the actuator frequency and geometry, a specific jet flow rate can be obtained. In application, the lower frequency limit usually relates to the lowest operating frequency where the jets produce heat transfer exceeding natural convection. The upper frequency limit corresponds to a fundamental frequency for the actuator, usually a structural resonance for the piezoelectric diaphragm or the Helmholtz frequency for the cavity. At one of these conditions, the exit velocity reaches its peak value.

1.2 Ultrasonic micro blower

One of the prime limitations of synthetic jet piezoelectric actuators are their significantly high noise output generated from the motion of the diaphragm and high velocity jet stream mixing with the atmosphere. Unfortunately, synthetic jet effectiveness often dictates operation at the actuator resonant frequency to maximize jet exit velocity, which coincides with the highest noise output [32, 33]. It was observed by Arik [34] that synthetic jet noise can be as high as 73 dBA when operating at a resonant frequency of 3.6 kHz for a peak jet velocity of 90 m/s out of a 1 mm orifice.

They may be some methods to decrease the noise level. It is possible to use slightly off-resonant actuation conditions to produce lower noise. But the best method should reduce the noise generated by piezoelectrically driven synthetic jets without decreasing peak jet velocity. Jabbal and Kykkotisa [35] reported a 32% noise reduction (20 dBA) from operating a single chamber, circular orifice jet to a double-chamber, corrugated-lobed orifice jet at the Helmholtz resonant frequency. Results also showed there was a small reduction in peak jet velocity of 7% (~3 m/s) between these two cases based on orifices of the same discharge area.

One of the other possible solutions is operating the jet at the frequency which is higher than the audible sound level of human 22 kHz [36–38]. Figure 3 shows an image of the ultrasonic piezoelectric micro blower used in this study. This blower is manufactured by Murata Manufacturing Co. Ltd. [36]. The blower is made up of a chassis, an exhaust nozzle, a diaphragm, a piezoelectric disk and electrical connection. The casing has a footprint area of 20 mm x 20 mm and a thickness of 2 mm. This device has two nozzles; one is placed at the Inner cavity, which has the 0.5 mm diameter and the exhaust one which has 1 mm diameter. By applying an alternating current as a sine wave, the piezoelectric disk that is bonded to the diaphragm expands and contracts. When the piezoelectric disk contracts, the diaphragm is pulled and the inner cavity expands. Then the chamber sucks the air from the air inlet. When the piezoelectric element expands, the diaphragm is pushed and the inner cavity contracts. Then, air is pushed out from the diaphragm. These actions continually repeat according to the frequency of the vibration of the piezoelectric element. This mechanism generates the flow stream. It is important to note that having two nozzles make this device unique and let the device suck in the air from the backside of the device unlike synthetic jets which suck the air from the exhaust nozzle.

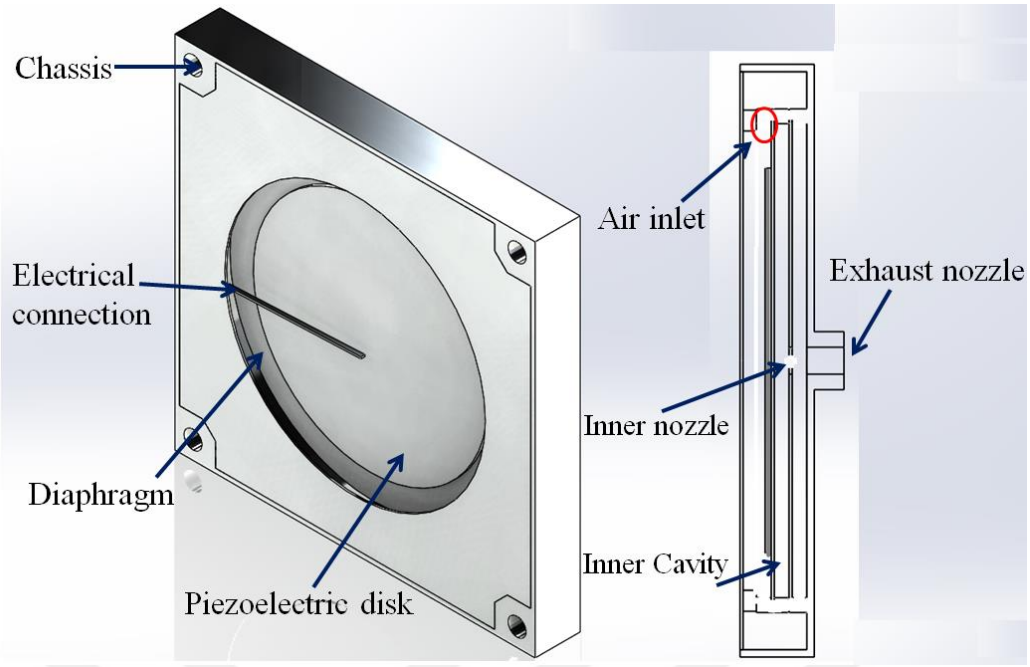

Figure 3. Schematic of the piezoelectric ultrasonic micro blower used in this study.

1.3 Motivation and novelty of the current study

1.3.1Slot synthetic jets

Previous studies of synthetic primarily focused on the heat transfer response, leaving the underlying mechanisms behind their performance unclear. When examining the current literature, there are several issues that invite further exploration. First, while the slot synthetic jet has shown promise for impingement cooling, its transient fluid response has not been analyzed. In particular, only smoke visualization and time-averaged PIV have been used, which prevents detailed study of the vortex pair development. Second, there is limited transient flow analysis at different operating frequencies, even with round jets. Third, there is a limited number of studies of off-resonance response, even though most synthetic jets have comparable heat transfer over a band of frequencies.

The in house manufactured synthetic jets used in this study have a different topology than the previous slot actuators, sandwiching two circular disks together. While a large number of

earlier devices placed their orifices normal to the oscillating piezoelectric disk, this new approach placed the orifice along the circumference of the sandwiched pair. Hence, the jet direction was perpendicular to the piezoelectric disk deflection. A brief list of motivations for the current study is given as follows:

- Find the fundamental frequency and best operating conditions of the novel synthetic jet by measuring the diaphragm deflection.
- Examine the flow mechanisms of both the free and impinging slot synthetic jet, particularly at the fundamental frequency by means of particle image velocimetry(PIV) and computational fluid dynamics (CFD) tools.
- Determine the reason for the significant degradation of heat transfer at small orifice-to-plate ratios, specifically by investigating the effect of jet-to-surface distance on the flow field.
- Investigate the wall jet profile of the synthetic jet, comparing it with laminar and fully turbulent profiles.
- Calculate the coefficient of performance (COP) to find the best operating condition for this slot synthetic jet.
- Investigate the heat transfer of slot synthetic jet compared to central orifice circular synthetic jet.

1.3.2. Ultrasonic micro blower

Earlier studies of this ultrasonic micro blower primarily focused on the heat transfer response, leaving the underlying mechanisms behind its performance unclear. Thus, we have examined the flow physics for this device using particle image velocimetry (PIV). We have conducted time-averaged flow analysis in order to understand the driving mechanisms that affect the heat

transfer of free and impinging jets. Here, we summarize the goals of the study of the ultrasonic micro blowers:

- Find the best operating conditions of the ultrasonic micro blower by measuring the diaphragm deflection.
- Examine the flow mechanisms of both the free and impinging blower jet, particularly at the best operating frequency.
- Examine the heat transfer performance of the impinging micro blower jet and compare to synthetic jet and continuous jet.
- Calculate the coefficient of performance (COP) to find the best operating condition for this micro blower

CHAPTER II

EXPERIMENTAL STUDY

2.1 .Deflection and Thermal Measurements

Synthetic jet performance is strongly dependent on the cavity volume. The cavity has a dynamic size during the operation, changing with contraction and expansion of the actuator. Disk deflection is critical in obtaining the optimal device frequency and corresponding outflow performance. However, high deflection does not always correlate with good thermal effectiveness, so impingement cooling must also be assessed. Thus, we developed an experimental apparatus to determine both disk deflection and impingement heat transfer.

An experimental system has been designed and manufactured for this research. The test apparatus, as shown in Figure 4, includes several individual components, which are mounted to an optical table within an enclosure. These exterior features isolate the instruments from environmental disturbances. The jet actuator is attached to a 3D robotic traverse, which is used to position the device to within ±7 μm. A function generator provides a sinusoidal waveform to the synthetic jet, and a signal amplifier increases the voltage to a desired level. A Polytech laser vibrometer measures the movement of the piezoelectric disk.

The heat transfer is examined using a square heater of 25.4-mm side length, comparable to electronic device sizes . Heater temperature was set at 60 °C for all tests, and it was controlled by a LABVIEW computer program.

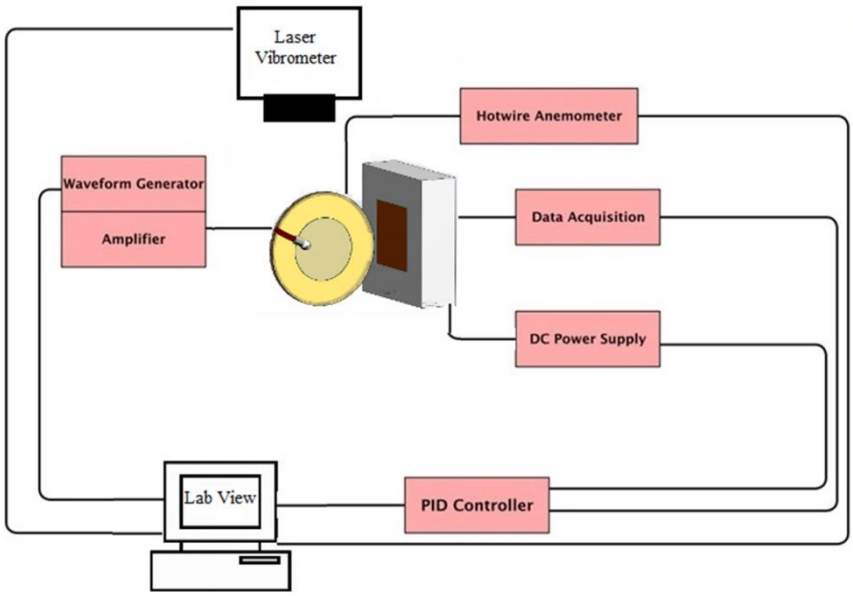

a)

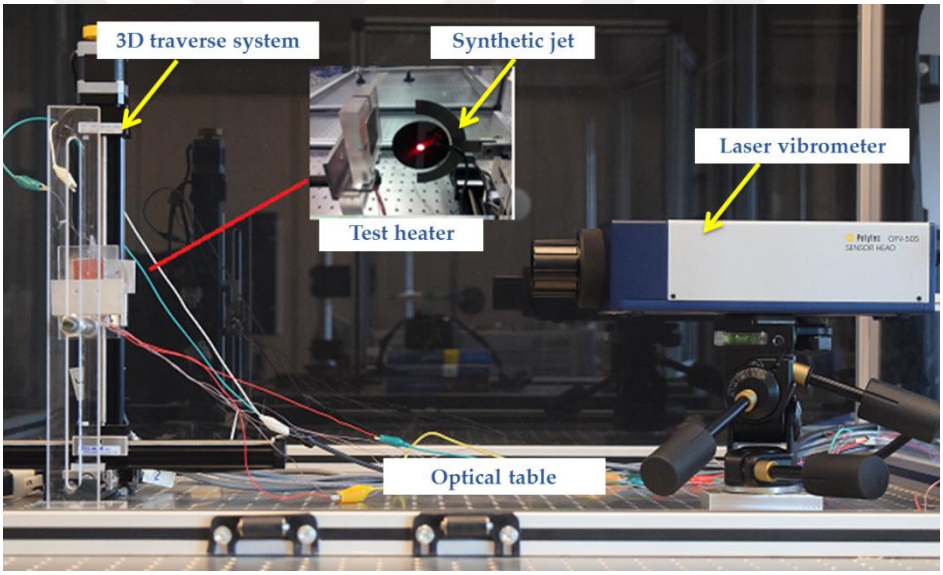

b)

Figure 4. (a) Schematic diagram of experimental setup. (b) Picture of the actual test system with synthetic jet and vertical heater.

2.1.1. Deflection measurements and fundamental frequencies

A synthetic jet is a coupled system of electromechanical and fluidic domains. There are two different types of resonance frequencies associated with synthetic jets, one with the mechanical part and the other with the fluid known as structural resonance and Helmholtz resonance respectively. Before experimental measurements structural and Helmholtz resonance frequencies were calculated using a simple formula given in the literature. The following formula was used for the calculation of the fundamental structural resonance frequency for a clamped circular diaphragm[39];

$$f_d = 0.4705 \frac{b}{r^2} \sqrt{\frac{E}{\rho(1-vp^2)}} \quad (1)$$

Where E is the modulus of elasticity, ρ is density, b is thickness of diaphragm, υ_p is Poisson ratio of material and r is the radius of diaphragm. Equation (1) is for a simply clamped diaphragm, and it has a shortcoming in capturing the effect of piezoelectric layer on the top metallic plate. It is also noteworthy to mention that the slot jet can be assumed as a partially clamped diaphragm, so equation 1 is only applicable for *ART4000* circular synthetic jets.

Helmholtz resonance frequency of a cavity is another parameter that affects the performance of a synthetic jet. The following expression is used for the Helmholtz resonance frequency of a typical cavity [39];

$$f_h = \frac{c}{2\pi} \sqrt{\frac{A}{(Z+0.85D)V}} \quad (2)$$

Where c is the speed of sound, Z is cavity height, D is orifice diameter, V is cavity volume,and A is the area of the orifice. For slot jet, instead of hydraulic diameter (D_h), the width of the nozzle was used. Table 1 displays the geometry and specifications of *ART4000* (circular) and *ART4000s* (slot) synthetic jets.

Table 1.Features of manufactured synthetic jets (ART4000 and ART4000s)

	Property	ART4000	ART4000s
Geometry	Shim diameter (mm)	40	40
	Shim thickness (mm)	0.11	0.11
	Piezoelectric diameter (mm)	25	25
	Piezoelectric thickness (mm)	0.1	0.1
	Cavity diameter (mm)	38	38
	Cavity height (mm)	1.2	1
	Orifice diameter (mm)	2	1.778
Shim	Young's modulus (Pa)	2.00E+11	2.00E+11
	Poisson's ratio	0.3	0.3
	Density (kg/m^3)	7750	7750
Frequency	f_d (Hz)	689	Partially clamped
	f_h (Hz)	1540	3443

Synthetic jet behavior depends on multiple physical effects, including electro-mechanical, fluidic and acoustic elements. Most synthetic jets experience two different fundamental frequencies: one related to the mechanical domain, and the other to the fluidic. These are referred to as the structural resonant frequency and the Helmholtz resonant frequency, respectively. To examine these responses, the deflection of the slot jet (*ART 4000s*) was measured for a range of frequencies from 100 Hz to 2500 Hz. During the experiments, the sample rates had an interval of 50 Hz in order to capture the deflection at the different modes, which is used to find the best operating frequency for the jet. Figure 5 displays the change of the deflection at the center of the diaphragm at different frequencies. Here, the applied

voltage is 35 V_{pp} (Voltage peak-to-peak). Three different peaks are observed at f = 450, 1000 and 2000 Hz. The maximum defection occurred at 450 Hz, which is related to the first mode of vibration of the diaphragm. The diaphragm for a slot jet is a thin circular plate with partially free and partially clamped edges, as seen in Figure 1a. Thus, the position of maximum deflection is not exactly at the center of diaphragm, but rather is located slightly towards the partially free part of the diaphragm.

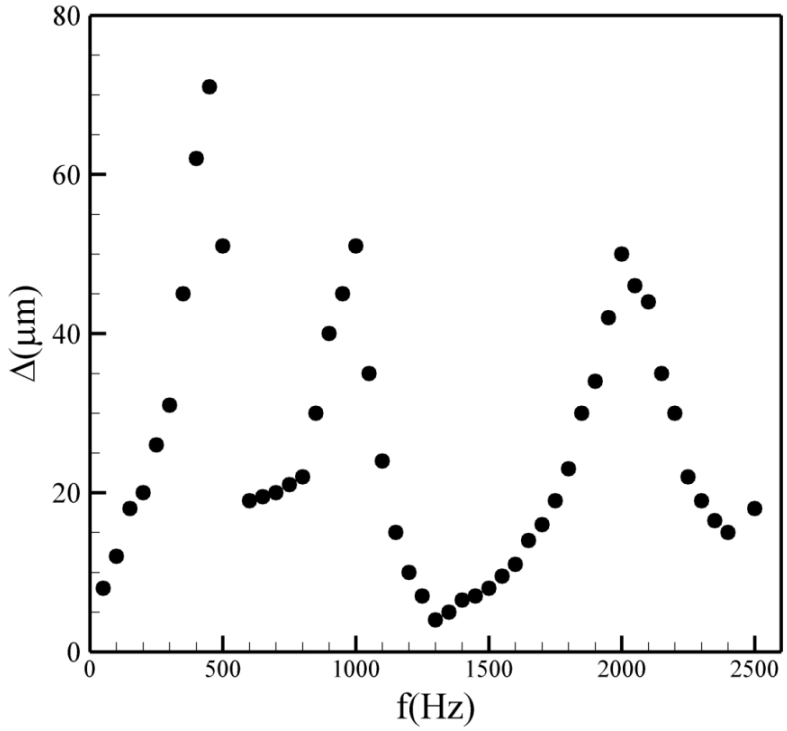

Figure 5 .Variation of deflection at the center of the actuator diaphragm versus applied frequency at 35 *Vpp* (Voltage peak to peak) for *ART4000s*.

The maximum deflection should correspond to the first resonant mode of this partially-clamped diaphragm, when the membrane vibrates like a drum without angular or radial nodes. For a similar geometry [40], the second mode has an angular node line across its diameter, with a natural frequency of approximately twice the first resonant frequency. This agrees with

the ratio seen in Figure 5, with the second peak at 1000 Hz being 2.2 times that of the first mode. Using a similar frequency scaling, the third peak at 2000 Hz would correspond to the sixth resonant mode, which features axisymmetric vibration with a single radial node [40]. Each of the other intermediate modes is radially asymmetric. The flow coming out from the orifice was found to be the strongest at both 450 Hz and 2000 Hz, but it was weak at 1000 Hz. The strong air flows correspond to the two axisymmetric modes, while the 1000 Hz peak should have an angular node. In addition, this weak flow at 1000 Hz may also be due to complex fluid-structure interactions inside the cavity.

The analytically measured structural frequency of ART4000 jet was observed to be slightly deviating from experimental findings. Figure 6 shows the variation of the deflection at the center of diaphragm with driving frequency for the circular jet. The maximum deflection occurred at 700 Hz that is close to the analytical value. Since the diaphragm for ART4000 is completely clamped, the location of the maximum deflection is at the center of the diaphragm.

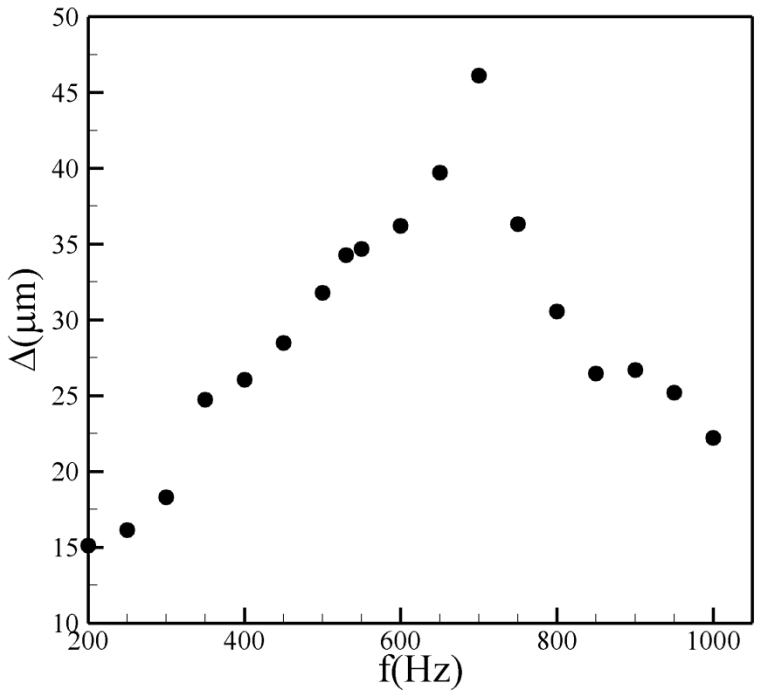

Figure 6 .Variation of deflection with driving frequency for ART4000 synthetic jet. (driven at *V*=20Vpp)

The Helmholtz resonance frequency of micro blower was calculated to be around 21 kHz for the inner cavity of micro blower. Since the jet operates at the non-audible frequency *f*>22kHz, it would be ideal to match diaphragm resonance frequency and cavity Helmholtz resonance frequency to have jet best performance.

While the first mode shape of the diaphragm usually was chosen to operate synthetic jets, the third mode shape was preferred for the ultrasound micro blower jet based on the manufacturer's suggestions [36]. Table 2 shows the features of the high frequency ultrasonic micro blower.

Table 2.Features of ultrasonic micro blower

Geometry	Shim diameter (mm)	13
	Shim thickness (mm)	0.08
	Piezoelectric diameter (mm)	10
	Piezoelectric thickness (mm)	0.15
	Cavity diameter (mm)	12
	Cavity height (mm)	0.1
	Orifice diameter (mm)	1
Shim	Young's modulus (Pa)	2.00E+11
	Poisson's ratio	0.3
	Density (kg/m3)	7750
Frequency response	f_d (Hz)	8894
	f_h (Hz)	21100

To examine these responses, the deflection of jet was measured for a range of frequencies from 23 kHz to 27 kHz. The samples had an interval of 100 Hz in order to capture the deflection at the third mode of the actuator, which is used to find the best operating frequency for the jet. Figure 7 displays the change of the deflection at the center of the diaphragm at different frequencies. Here, the applied voltage is 20 V_{pp} (Voltage peak-to-peak). The maximum deflection obtained during experimental study was around 13 μm at 25 kHz. We set the best operating condition of the micro blower at 25 kHz due to the high stream velocity at this condition.

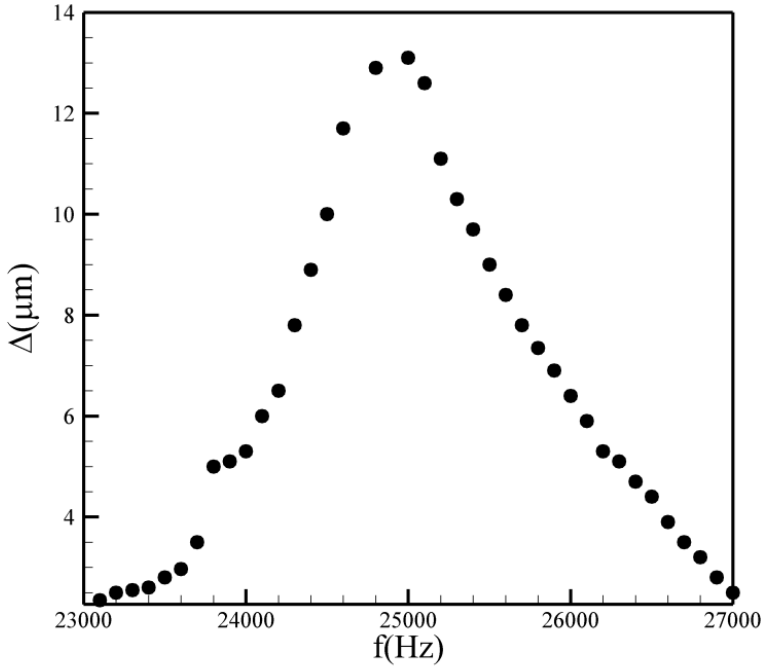

Figure 7: Variation of deflection at the center of the actuator diaphragm versus applied frequency at 20 Vpp.

2.2.Heat transfer mesurments and heater design

An in-house designed and manufactured square heater, mimicking a typical electronic component (L=25.4 mm), was used to examine the heat transfer enhancement. A kapton

heater (A polyimide, film-insulated, flexible heater) was placed in between two highly conductive plates in order to keep the temperature uniform on the front surface (copper surface) and avoid local temperature gradients(see figure 8).

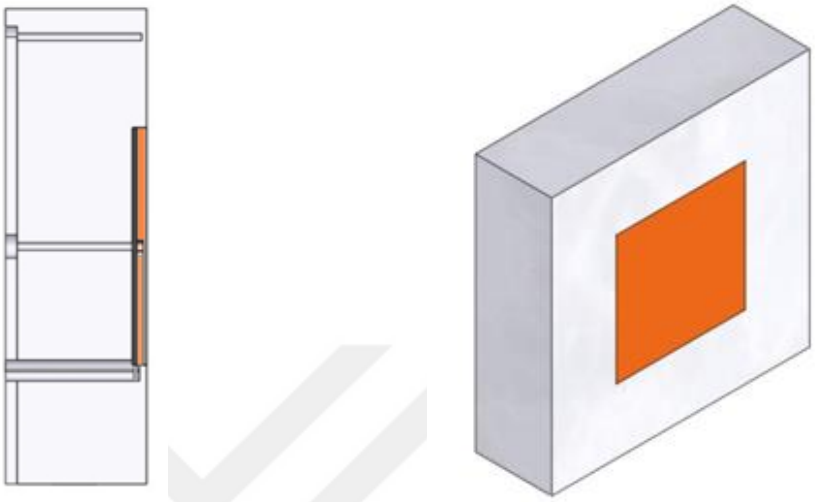

Figure 8.Heater construction

We have performed a three dimensional CFD modeling of heater with ANSYS Icepak [41] by considering these assumptions :

- Steady state incompressible flow
- Natural convection with radiation
- Conduction heat transfer with generation
- The thermal interface materials between the heater assembly layers.
- Three dimensional modeling

Figure 9 shows the heater and solution domain along with mesh. We use structured hex mesh to perform CFD analysis.

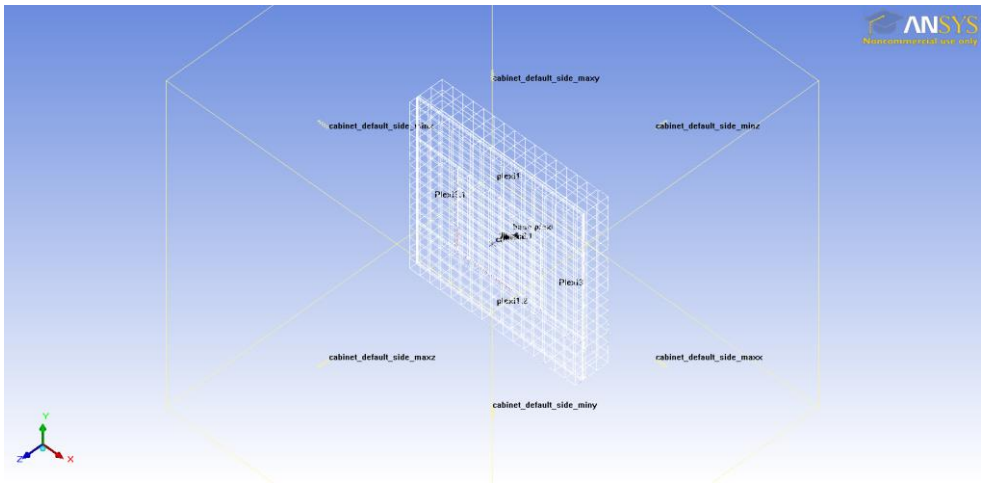

Figure 9: Mesh and geometric configuration in CFD models

We have also studied mesh dependency to assure that our models do not depend on the mesh count. Figure 10 and 11 shows the mesh sensitivity analysis for temperature along vertical and horizontal heater centerline. Results are no longer changing after 137500 mesh elements which reveal that the calculation is independent of the mesh. The applied power to the heater is 0.4 watt .Later we verified the results with heat transfer.

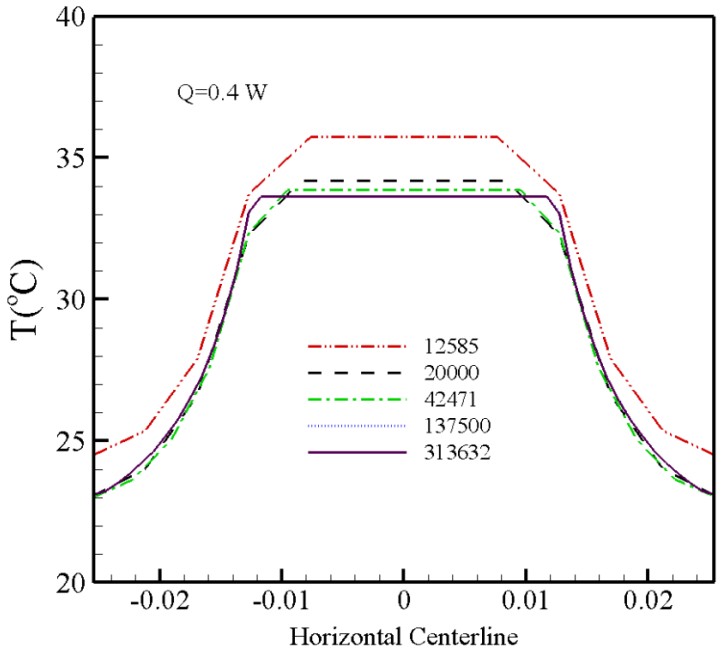

Figure 10. Temperature distribution along the horizontal centerline on the front surface for Q=0.4 W.

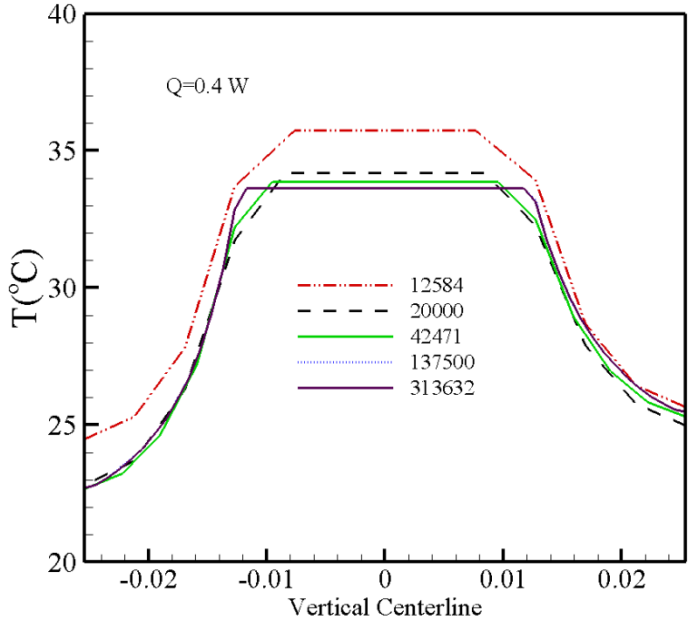

Figure 11: Temperature distribution along the horizontal centerline on the front surface for Q=0.4 W.

Figure 12 presents the temperature distribution for a sample CFD study for our test heater. It is found that central part of the heater is warmer than plexiglass section. This is expected, and it serves for the purpose of the insulating plastic substrate.

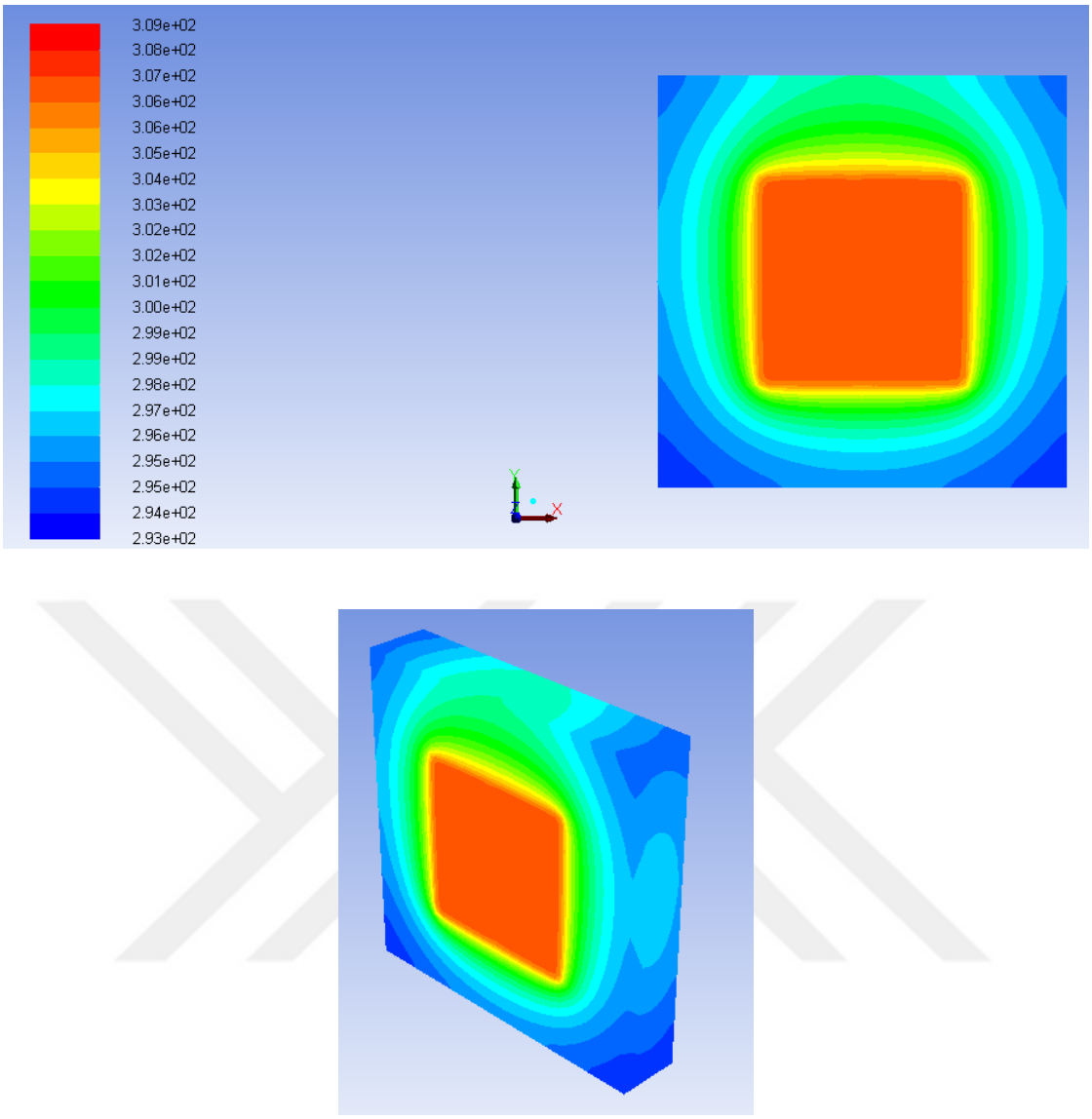

Figure 12:Temperature contour plots of the heater for Q= 0.4W,T_{amb}=293.15 K.

The heater was modeled three dimensionally in ANSYS Icepak by considering the natural convection and radiation. Models are validated with the experimental results. Experimental and computational findings are found to be very close to each other(Figure13). Here ΔT is temperature rise over ambient.

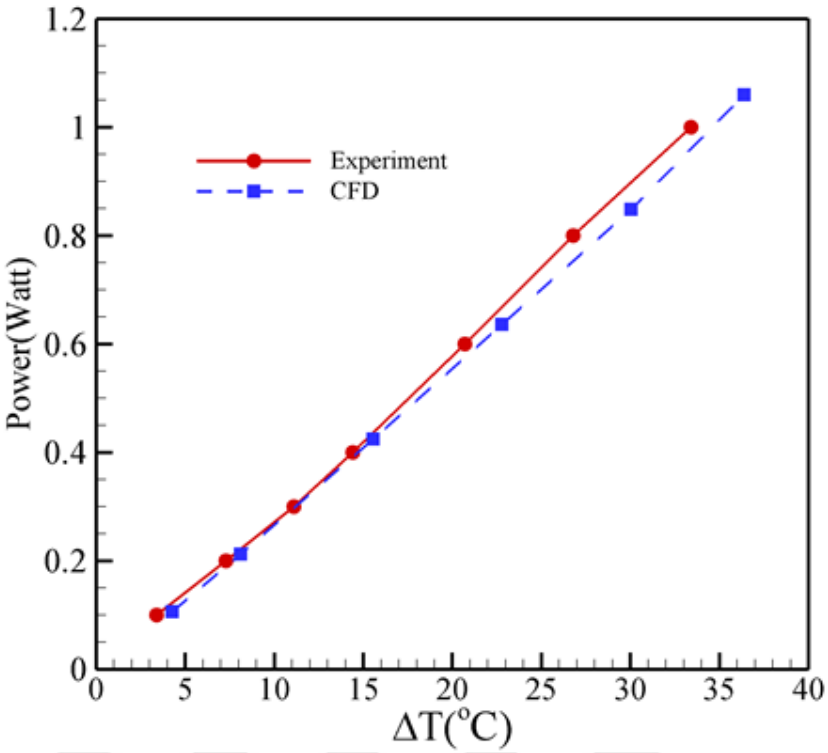

Figure 13: CFD validation with experimental data.

A guard heater was used to quantify the heat loss from low conductivity plastic substrate for a range of heater temperatures and heater to ambient temperature gradients. Figure 14 shows characteristic curves of the test heater showing variation of the heat transfer with temperature differences. One of them shows the total heat transfer from the heater while the next is heat loss from other faces except for the front face. Third one shows the net heat transfer to ambient from front surface. All three curves are linear with R-squared value near to 0.99 giving a high confidence level.

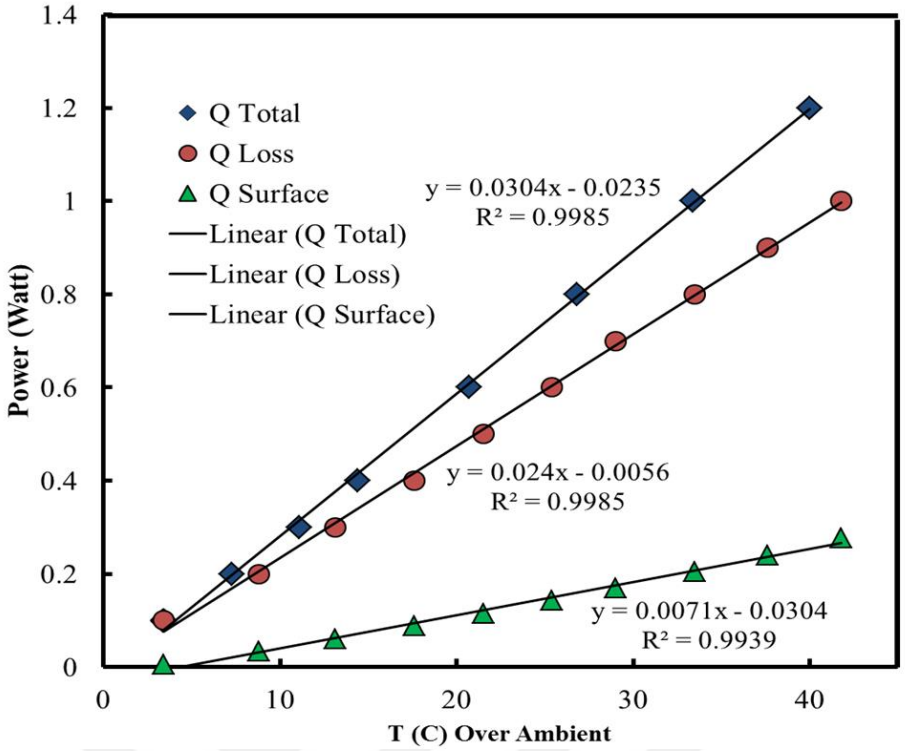

Figure 14: Heater characteristic curve showing the variation of cooling with heater surface temperature rise over ambient.

This information is used to calculate the heat loss from substrate except for the heater frontal surface so that a correct amount of heat can be calculated from front surface. The heat transfer on the copper surface ($Q_{surface}$) is calculated as:

$$Q_{surface} = Q_{total} - Q_{loss} \quad (3)$$

While earlier studies have presented combined synthetic jet convection and radiation heat transfer, in this study we aim to separate the radiation heat transfer. The average synthetic jet convection heat transfer coefficient on the copper surface is calculated as:

$$\overline{h} = \frac{Q_{surface} - Q_{radation}}{A_s \cdot (T_w - T_{amb})} \quad (4)$$

where A_s is the target heated wetted surface area, T_w is the heater wetted surface temperature calculated by averaging the temperatures measured by four thermocouples attached along the

target at the backside of the copper plate,and T_{amb} is the air temperature in the test chamber. Heater temperature was set at 60 °C for all tests, and it was controlled by a LABVIEW computer program. The steady state condition was assumed to be satisfactory when the standard deviation of surface temperature measurements for the last 30 readings was less than 0.1 ^{o}C.

When a synthetic jet is cooling a surface, three modes of heat transfer-forced convection, natural convection and radiation- will be in effect. The combination of natural and forced convection results in a mixed convection condition so the particular impacts of each convection have to be understood. Habibi et al [42–44] investigated the mixed convection of a slot impinging jet and showed the Richardson Number (i.e. Gr/Re^2) 0.01 <Ri < 0.4 satisfied mixed convection regime. They used inlet conditions and hydraulic diameter as a characteristic length for calculation of Ri number. The maximum Ri number in the present study was below 0.001 revealing that all the jets operate in forced convection regime.

2.2.1.Uncertainty Analysis

We used the methodology described by Moffat [45] to calculate the uncertainties in the experimental study, as seen in Table 3. Based on these values, the relative uncertainty in Nusselt number, $Nu = hD_h/k$, is approximately 6%. Here, D_h is the hydraulic diameter, and k represents the thermal conductivity of air.

Table 3.Estimated uncertainty for the thermal experiments

Parameter	Uncertainty (%)
Hydraulic diameter	2
Applied voltage	1
Applied current	1

Applied heater power	1
Thermocouples (T-type)	0.4
Deflection of actuator	3

2.3.Jet air velocity measurements

A velocity measurement test system was developed (see Figure 15(a)). Jet exit velocity measurements were taken using a TSI IFA300 constant-temperature hot-wire anemometer system[46] with a TSI 1210A single-axis hot wire probe (Figure 15 (b)). The sensing element length was 12.7 mm with a diameter of 3.8 μm.

The hotwire was calibrated prior to each test using a TSI 1129 velocity calibrator. The hot wire signal was correlated to the velocity by a fourth-order polynomial equation. Figure 16 shows a typical velocity mesurment at the center of the jet located at 1 mm away from nozzle exit in the absence of the heater. Peak velocity of the jet is found to be in excess of 26 m/s during the ejection phase.

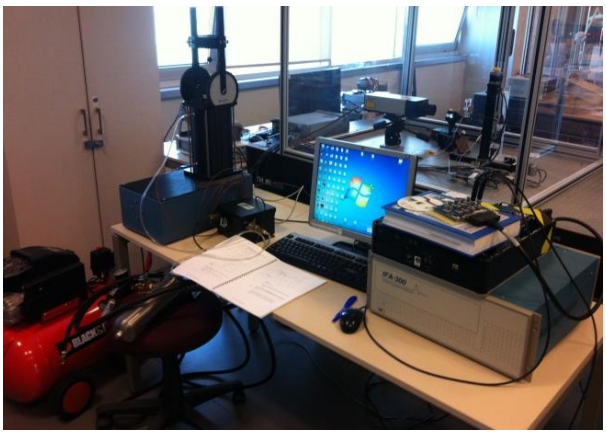

a)

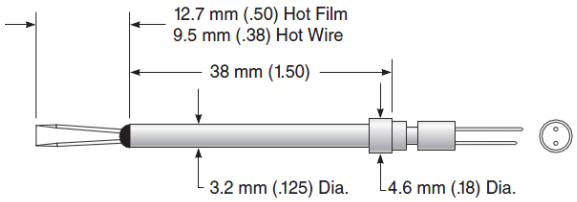

b)

Figure 15a) IFA300 hotwire anemometer setup (b) Single wire hot wire probe

Figure 16 displays a typical instantaneous velocity profile with respect to time for ART4000s (slot jet) jet at the resonance frequency of 450 Hz. Since a single axis probe was used, only one component is measured for the present study. The periodic nature of the air stream was quite clear where the peak velocity was observed during the ejection phase and dropped afterwards. This is an expected velocity profile for synthetic jet devices.

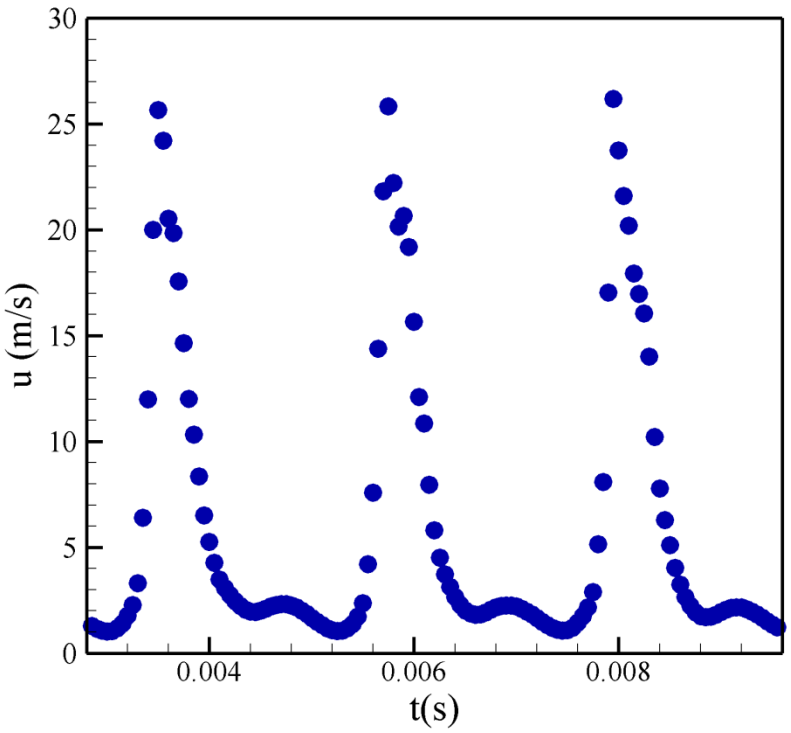

Figure 16:Variation of the absolute velocity with time for ART4000s at 450 Hz.

For heat transfer performance, peak exit velocity plays an important role and demands more attention. Figure 17 illustrates the peak velocity mesurments for different driving frequencies of both a slot and a circular jet. It is noteworthy to mention that the maximum velocity for slot and circular jet occurs at 450 Hz and 700 Hz respectively. While the jet outer dimensions are the same, it is observed that resonance frequency is shifted towards left for a slot synthetic jet due to unclamped part of diaphragm. In addition, a circular jet has a strong ejection velocity for a wider spectrum, while a slot jet has a steep behavior.

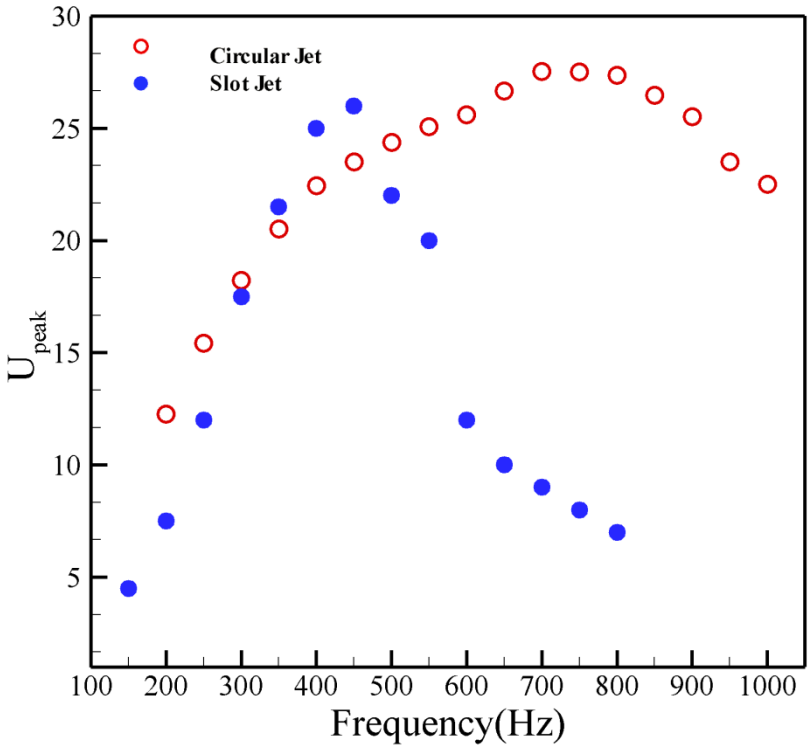

Figure 17: Effect of driving frequency for the peak velocities of ART4000 and ART4000s (slot jet).

2.4 Particle image velocimetry experiment

Particle Image Velocimetry (PIV) is a common technique for non-intrusive, quantitative and qualitative flow visualization. In PIV, the flow is visualized by illuminating a thin sheet of fluid containing reflective and neutrally buoyant(not all particles are neutrally buoyant, but they should not be heavy enough that they disturb the flow) tracer particles. A digital image sensor is positioned perpendicular to the illuminated sheet, capturing the movement of the particles (see Figure 18). In most PIV analyses, two images of the illuminated plane are captured at times t and t + Δt. Velocities in the sheet can hence be derived from Δt and the distance that the particles travelled from image A to B (particle displacement). In PIV, the particle displacement is calculated for groups of particles by evaluating the cross-correlation

of many small sub-images (interrogation regions). The correlation yields the most probable displacement for a group of particles travelling in a straight line between image A and image B [47].

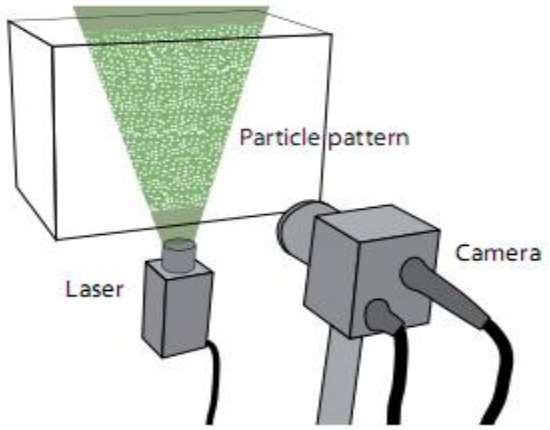

Figure 18:A laser sheet illuminates the particles contained in the fluid with a high speed camera recording the displacement of the particle pattern [47].

The experimental apparatus is depicted in figure19 and schematically in Figure 20, which shows the test section, the synthetic jet location, and PIV system. The test section consists of a nearly cubical chamber composed of thin-walled aluminum, with interior dimensions of 61.0 cm x 61.0 cm x 55.9 cm. The chamber is open at its top, and a square viewing port is cut into one side, permitting optical measurements from multiple directions. Opposite the viewing port, there is a 3.6-cm diameter hole for the synthetic jet actuator, centered in the middle of a side wall. A narrow, 1.27-cm wide slot is located in a perpendicular sidewall, aligned with the actuator centerline. This slot provides access for the PIV laser sheet. Each of these openings is covered with 1.27-cm thick acrylic plates, isolating the interior from the rest of the laboratory

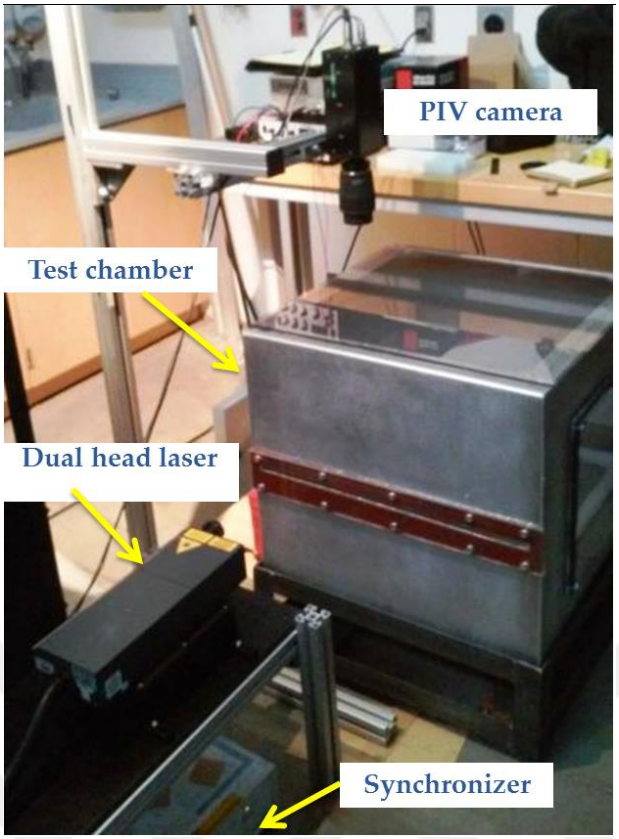

Figure 19: Image of the experimental apparatus for flow measurements .

The entire actuator is mounted on a ring stand, which projects it through the side wall opening into the test section. The orifice orientation is inwardly normal from the chamber wall.

Downstream of the actuator, a thin acrylic plate is mounted perpendicular to jet centerline, providing an impingement target. The edges of the plate are more than 50 slot widths from the target, so they should not have a significant three-dimensional effect on the response. We use a commercial PIV system to examine the flow response. This system features a dual-head Nd:YAG laser, which produces two 50 mJ pulses of 532 nm wavelength at two successive instants. For the experiments here, the pulses are applied 10 μs apart, which permits optimal particle motion for PIV analysis at the test conditions [47].

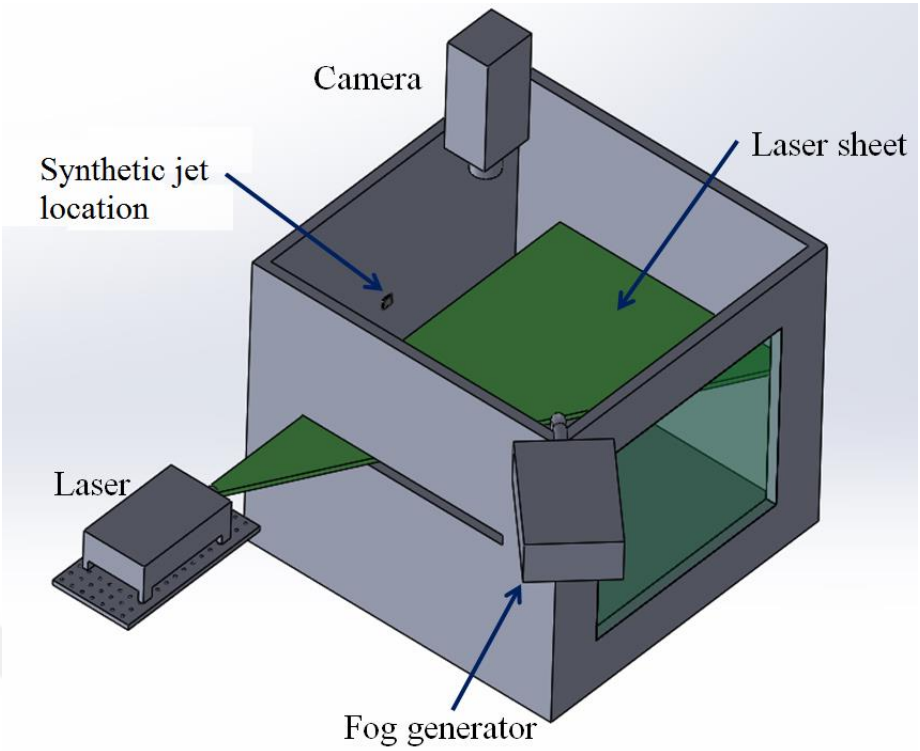

Figure 20.Schematic of the experimental apparatus, showing the cubical test section, the synthetic jet location, and the PIV system

The laser pulses are converted to a laser sheet using a pair of lenses, resulting in a 0.5-mm thick sheet projected along the actuator centerline. This sheet cuts across the shorter side of the rectangular orifice, where the near-exit region is comparable to two-dimensional slot flow.

The light illuminates 1-μm diameter oil tracers, which are produced using a fog machine. In each test, the fog is supplied to the test section prior to the experiment, and then the chamber is closed for several minutes to allow the particles to disperse uniformly. A 1.4-megapixel digital camera is mounted directly above the test chamber, and it captures images of the illuminated particles at each instant. Both the laser and the camera are controlled by a commercial synchronizer, whose time control is accurate to 200 ns. This synchronizer can also be operated with a delayed trigger, permitting phase-locked measurements during the actuator motion.

We analyze the image pairs using PIVlab, an open-source analytical PIV code based in MATLAB [48]. This software divides the images into smaller interrogation regions, and it cross-correlates these regions to determine the local velocity vectors throughout the measurement plane. The analysis is iterative, successively decreasing the interrogation region size to produce finer resolution. The smallest region considered here was approximately 0.4 mm x 0.4 mm. For the free jet cases, the size was 1 mm x 1 mm. Using a propagation of uncertainties based on the processor and synchronizer accuracy, the uncertainty in instantaneous velocity is estimated as ±0.52 m/s, or ±2% of peak speeds. The corresponding uncertainty in vorticity is ±6.1% of peak values.

Chapter III

PIV JET FLOW FIELD STUDY

In order to understand the flow field associated with slot synthetic jet impingement cooling, flow behavior was investigated using PIV measurements. In this section, we first present the time-averaged results for a free slot synthetic jet. Then, we present phase-locked measurements for an impinging slot synthetic jet, followed by time-averaged results for an impinging slot synthetic jet.

We studied four different actuator frequencies: 350, 450, 600, and 2000 Hz. Two of these (450 and 2000 Hz) are selected because the Nu number reaches a peak in impingement heat transfer . These levels correspond approximately to the first two axisymmetric natural frequencies for this partially-clamped diaphragm [40]. The other frequencies (350 and 600 Hz) have heat transfer reduced by approximately 30% from the peak at 450 Hz. These latter cases provide information about the performance off of resonance. Later we investigated the effect of jet-to-surface distance on the flow field at H/D_h = 2, 5 and 10.

Table 4 shows details about these four test conditions, including two forms of the Reynolds number, Re, and Stokes number, S. Here, Re = UD_h/ν, where U is the characteristic velocity, D_h is the hydraulic diameter of the jet, and ν is the kinematic viscosity. The velocities used in the parametrization are the peak jet velocity, *Up*, and the average velocity during the outstroke, U_o.

Here, Re_{U0} number is calculated based on the work of Smith and Glezer [16]as:

$$Re_{U_0} = \frac{D_h U_0}{\upsilon} \qquad (5)$$

Here, D_h is the orifice hydraulic diameter, v is the kinematic viscosity and U_o is the average orifice velocity during the ejection portion of the actuation cycle, defined as:

$$U_0 = fL_0 \quad (6)$$

L_o is the jet stroke length defined as

$$L_0 = \int_0^{1/2f} u(t)\, dt \quad (7)$$

Reynolds number based on the peak velocity U_p is defined as

$$Re_{U_p} = \frac{D_h U_p}{\upsilon} \quad (8)$$

and Stokes number is:

$$S = D_h\sqrt{2\pi f/\upsilon} \quad (9)$$

These values are determined using D_h *=1.778 mm and* $\upsilon = 15.8*10^{-6}$ m^2/s.

Table 4.Test conditions

f (Hz)	Re_{Up}	Re_{Uo}	S
350	2470	730	21
450	2800	900	24
600	1350	500	27
2000	1400	840	50

At each frequency, a total of 500 image pairs were acquired without synchronizing the PIV system and the synthetic jet actuator. These images were processed to determine the instantaneous vector fields, and then they were ensemble-averaged to provide an approximate

time-averaged field. For the lower three frequencies, we also conducted phase-locked measurements by triggering the PIV synchronizer with the same function generator that operated the synthetic jet actuator. By applying delay times, we considered 8 separate phases during the actuator motion, spaced 45° apart. Based on the trigger accuracy, the uncertainty in the phase angle is ±0.5°. Since the function generator controls the piezoelectric disk, the trigger delays are synchronized to the mechanical deflection rather than the flow ejection at the orifice. As will be seen, this does lead to phase shifts in the outflow, which likely impacts the actuator performance. At each phase, we acquired 100 image pairs, whose corresponding vector fields were ensemble-averaged to determine the phase-locked flow response. Because the 2000 Hz case operated nearer to the Helmholtz resonant frequency, we did not acquire phase-locked data due to the acoustic noise.

PIV measurements examine a 2-D slice along the centerline of the jet. For the impinging jet, the minimum aspect ratio to obtain two-dimensionality is about 6:1 [19]. Therefore, at the aspect ratio of 8:1, the rectangular (slot) synthetic jet is treated as two-dimensional within the near field. Figure 21shows the schematic of the impinging slot synthetic jet. Here *W* is jet width and *H* is jet to surface spacing.

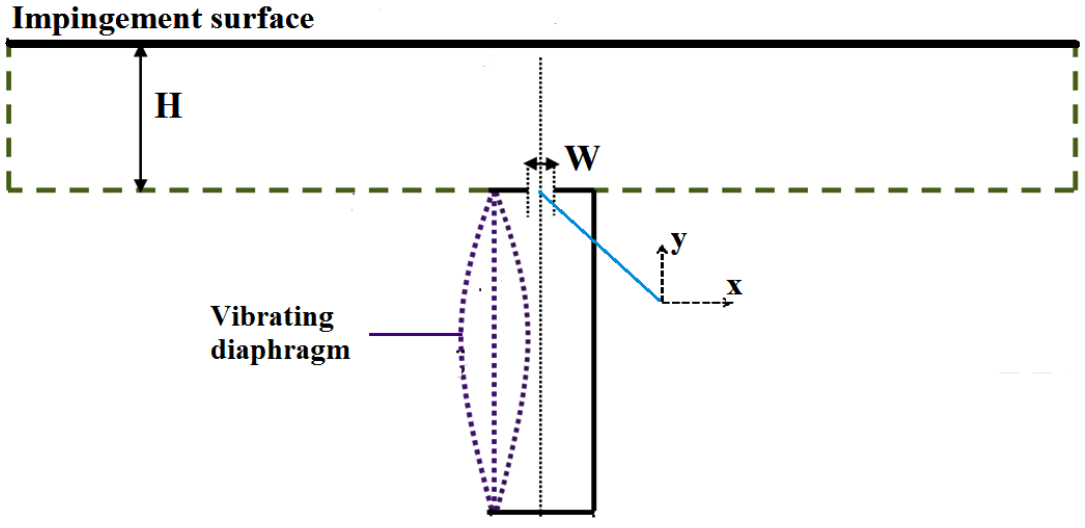

Figure 21:Schematic of impinging slot synthetic jet

3.1.Free slot synthetic jet

Figure 22 shows the time-averaged velocity vectors and vorticity contours for an upward-directed, free synthetic jet. Here, the jet operates at Re_{U0} = 900 and S = 24, which is the peak resonance at 450 Hz. Velocity is normalized by the average outstroke velocity, while vorticity is also normalized by the slot width.

The jet half-width grows slowly over the first 4 slot widths, and then it gradually rises to about $5W$ at y/W = 51 above the nozzle, the most downstream location in the PIV image. Both contour plots show near symmetric behavior.

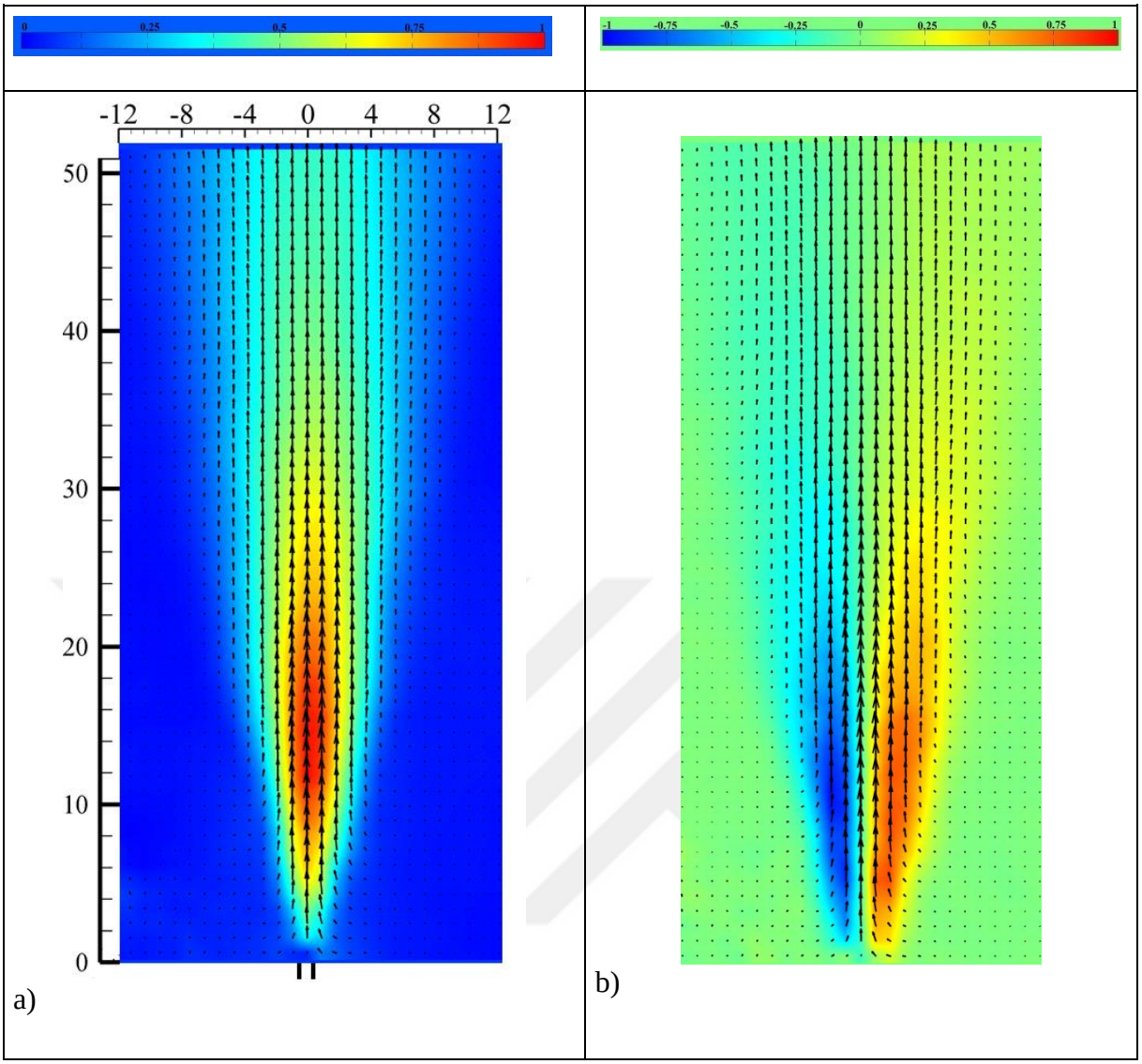

Figure 22.a.) Time-averaged dimensionless velocity vectors (U/U_0) and b.) dimensionless vorticity ($\omega W/U_0$) for a free, slot synthetic jet at Re_{U0}=900

Figure 23a shows the streamwise variation of normalized centerline velocity in the free jet. The velocity values are near zero at the exit because the oscillating flow in the synthetic jet balances over time. Downstream, the velocity reaches a maximum, demonstrating the time-averaged axial jet flow. This peak occurs in the region where the vortex pairs remain coherent, as shown later. Then, the jet spreads more in the transverse direction, which results in a decrease of the centerline velocity. Ultimately, the decrease in the far field deviates only slightly from 1/y, as might be expected from a steady, axisymmetric jet. Unlike in previous studies at low Re numbers and higher aspect ratio, the centerline velocity does not show any

secondary peak downstream from the orifice [11,22]. This suggests that the jet vortices are blurring more rapidly, resulting in downstream flow more similar to a steady jet.

Figure 23b shows the transverse distribution of streamwise velocity at different locations downstream from the nozzle. By comparing between these locations, we can see how the jet spreads away from the nozzle. Between y/W = 6 and 51, the jet width increases by a factor of approximately 4, and it becomes more bell-shaped. A previous study of a high-aspect ratio and lower-Re number jet showed much faster growth, though its profile was more uniform [11]. This further suggests that our lower-aspect ratio jet is becoming three- dimensional very rapidly.

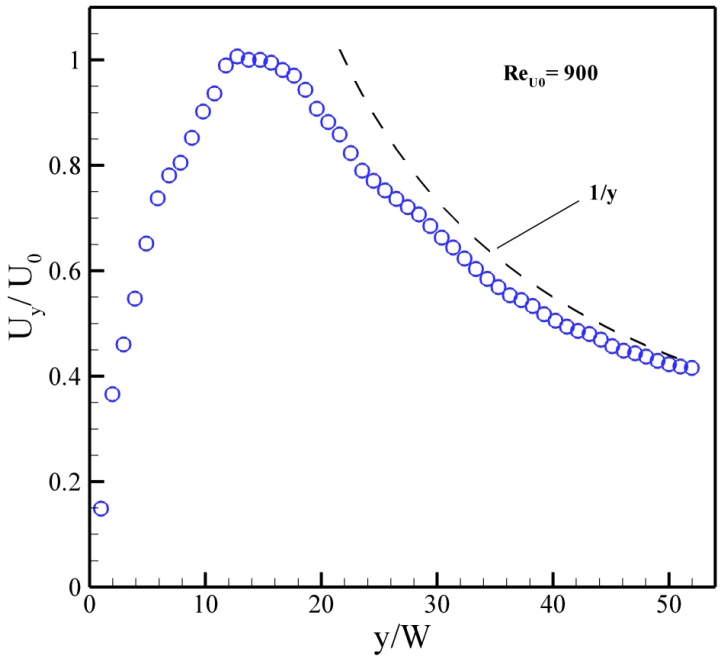

a)

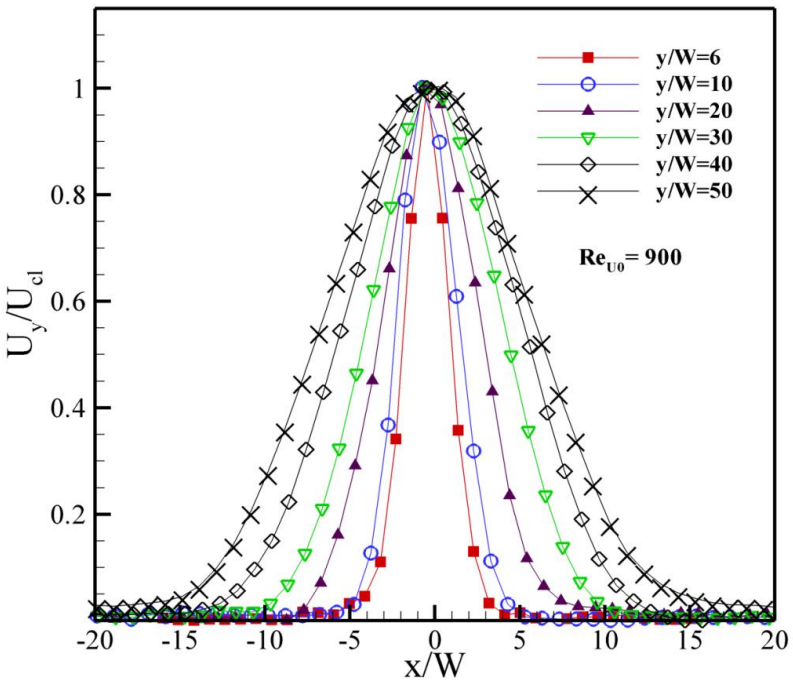

b)

Figure 23:a.) Streamwise variation of normalized centerline velocity in the free jet and b.) Transverse distributions of streamwise velocity in the free jet

3.2 Effect of the jet –to surface spacing

Figure 24 shows the velocity vectors and vorticity contours at $H/D_h = 2$ for eight phases. This wall location is nearer to the jet than the optimal condition for heat transfer. Vortex pairs need some streamwise distance to grow to their peak strength. When the impingement plate is close to the surface, there is less room for growth, and thus the flow is affected by the impinging plate. This is clear from figure 24, as the vortex pairs reach the surface at an early stage of ejection, at a phase angle less than $\Phi = 45^o$. Within phase angles between $45 \leq \Phi \leq 180^o$, air next to the impinging plate is moved by the vortex and re-entrained to the jet flow. In a case involving a heater, these vortices would recirculate warm air back into the jet, reducing the temperature difference and resulting heat transfer.

During the suction stroke, where $\Phi > 180^o$, the vortex pair travels away from the centerline. However, at $\Phi = 225^o$ and 270^o, the re-circulating flow is close enough to the orifice that fluid

may be drawn back into it. Since this is warm air from near the heater, this directly impacts the temperature of the jet flow before it reaches the target plate. When combined with the re-entrainment of warm fluid described earlier, it is clear that heat transfer should decrease at this close jet-to-surface spacing

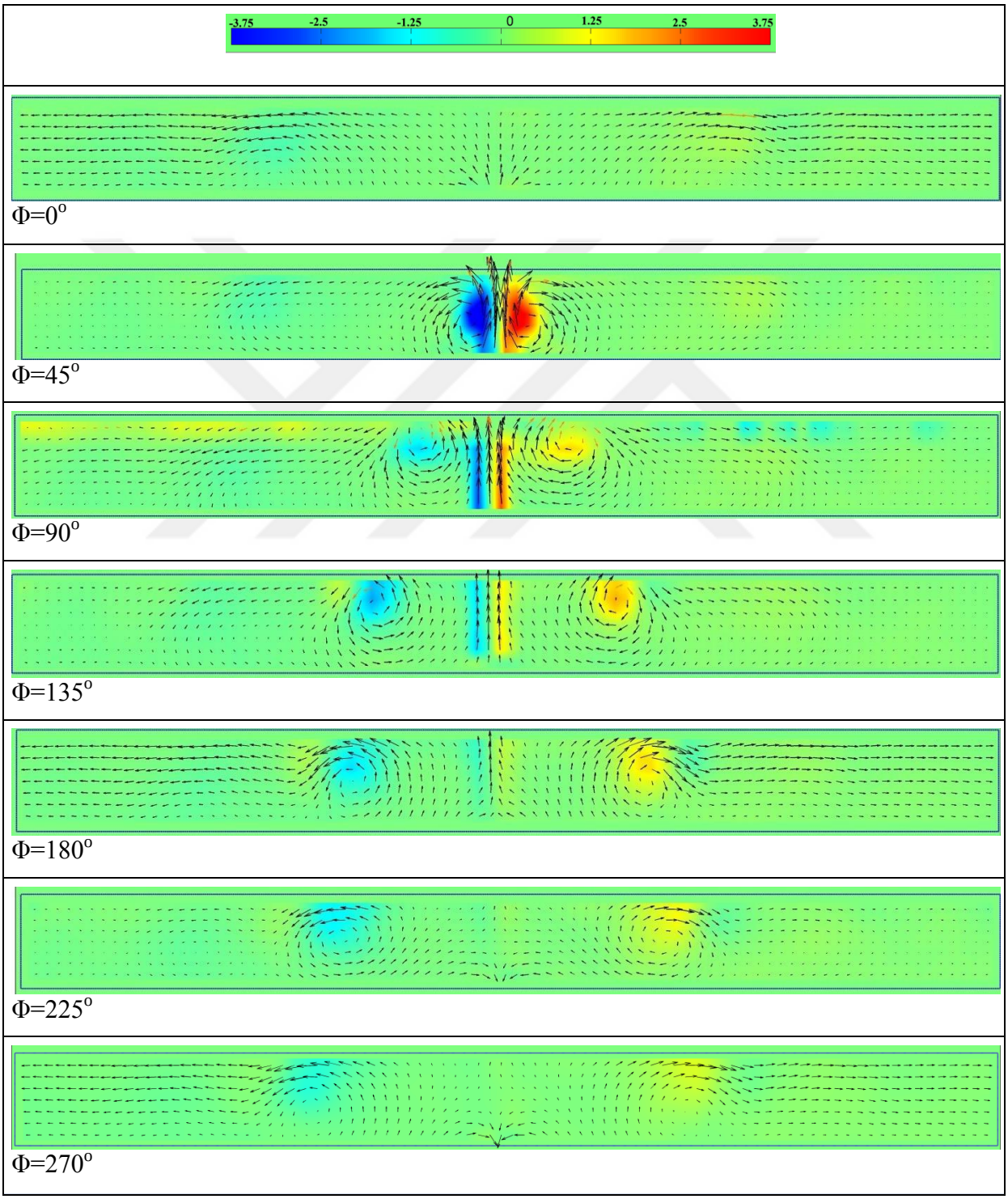

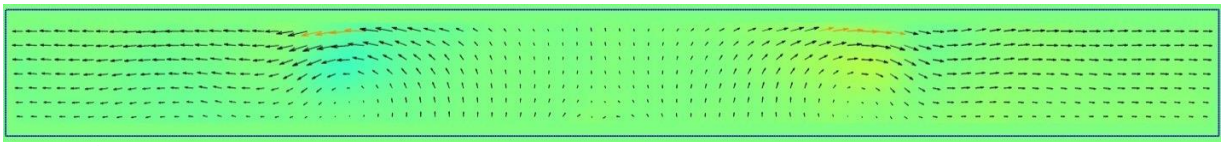

Φ=315^o

Figure 24.Phase-averaged velocity vectors and dimensionless vorticity contours, $\omega W/U_0$, for an impinging slot synthetic jet at Re_{U0} = 900, S = 24, and H/D_h = 2.

Figure 25 shows phase-locked vorticity contours at a greater jet-to-surface spacing, H/D_h = 5, for the same Reynolds number, Re_{U0} = 900. Here, four phase angles are shown, spaced 90^o apart. The beginning of the outflow is seen at Φ = 0^o, which leads to a strong vortex pair emanating from the nozzle exit by Φ = 90^o. At this phase, the vortices have nearly reached the wall, yet the trailing jet is still attached to the nozzle. This means that the normalized stroke length L_0/H > 1 at this operating condition. In addition, it also suggests that smaller wall spacings modify the vortex growth before the outflow has finished.

The vortex pair detaches from the orifice exit at the beginning of the suction phase, at Φ = 180^o. As the vortex pair moves outward along the target surface, the vortex/wall interaction is strong enough to create a small, secondary vortex in the boundary layer with an opposite rotation direction from the main vortex. This is partly because of the associated image vortex, which has the opposing sign. Further, the boundary layer growing on the wall has vorticity opposite from the primary vortex pair. The strength and scale of the secondary vortex decreases gradually as it breaks down due to the turbulence. The secondary vortex is the consequence of near wall shear layer disturbance, and as a result there is more heat transfer from the surface. In the final phase shown, Φ = 270^o, the primary vortex has become more concentrated again, and it travels further away from the stagnation point.

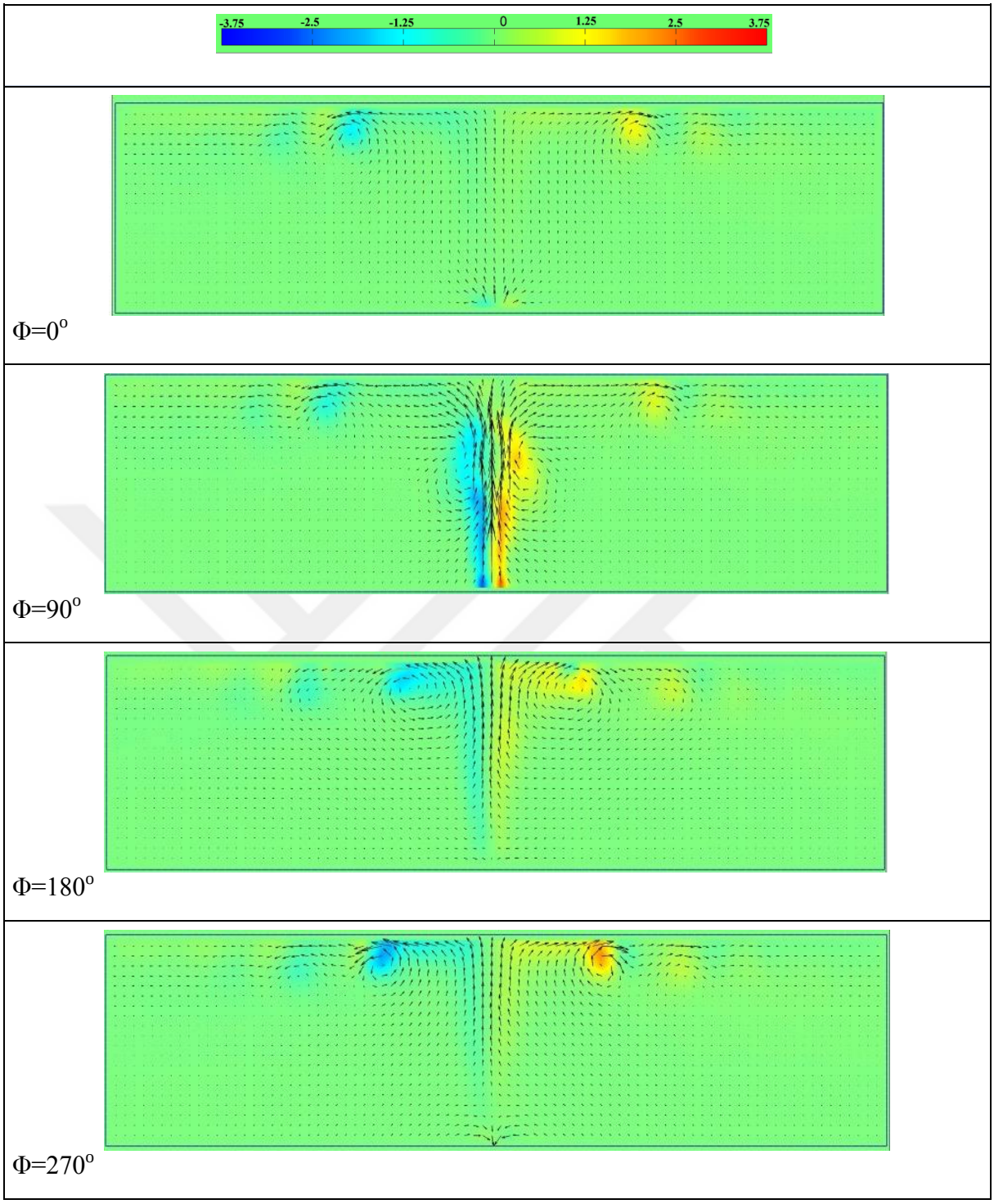

Figure 25:Phase-averaged velocity vectors and dimensionless vorticity contours, $\omega W/U_0$, for the impinging slot synthetic jet at Re_{U0} = 900, S = 24, and H/D_h = 5.

Figure 26 displays the phase-averaged vorticity contours at the same Reynolds number, Re_{U0} = 900, and a larger jet-to surface spacing, H/D_h = 10. Now that the impinging plate is located

farther away from the nozzle, the jet grows and spreads more compared to the two other wall locations. When the vortex pair is about to detach from the nozzle at $\Phi = 180^o$, the tip of the vortex almost reaches to the target plate. This means that at this target plate location, $L_0 \approx H$. It is likely that the jet experiences edge effects at this downstream distance, as H is larger than the slot length of $8W$. This would reduce the coherence of the ejected structures as they approach the wall.

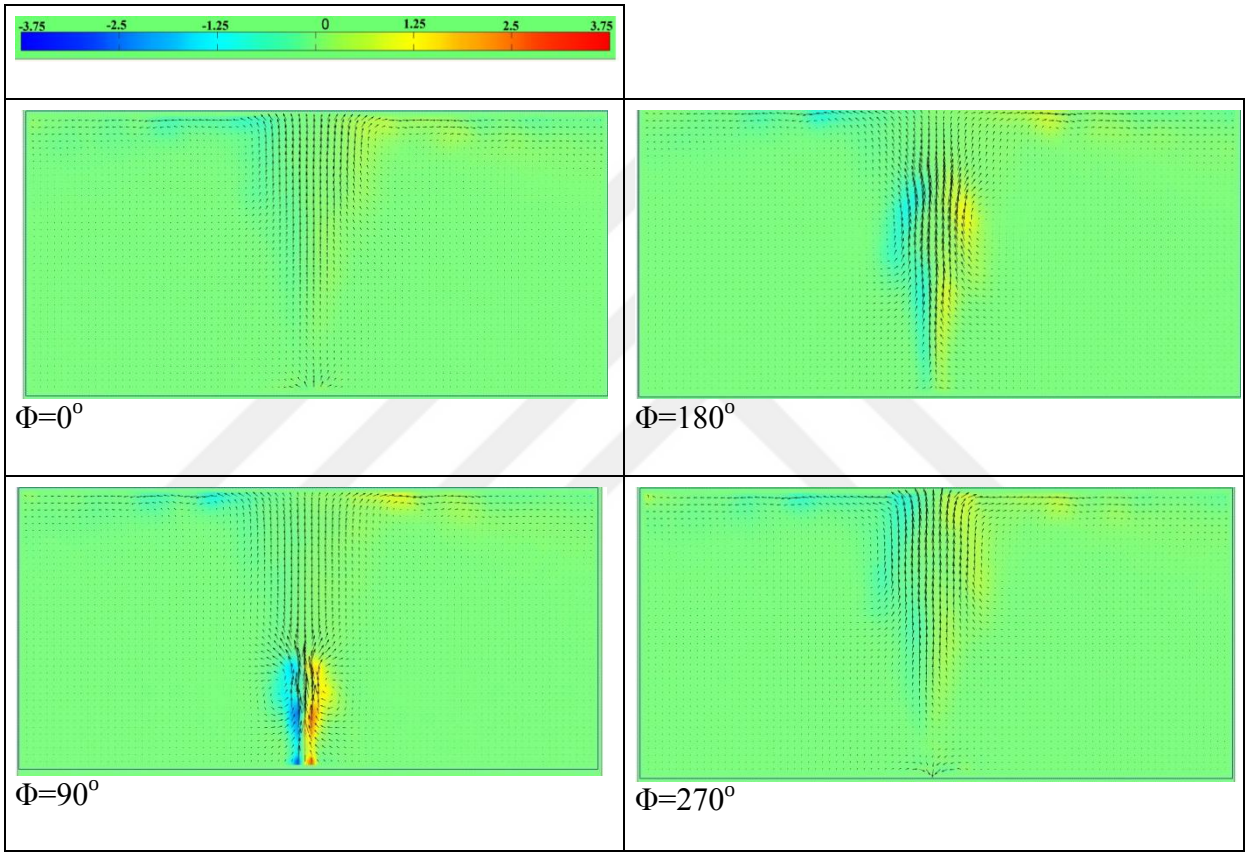

Figure 26: Phase-averaged velocity vectors and dimensionless vorticity contours, $\omega W/U_0$, for an impinging slot synthetic jet at Re_{U0} = 900, S = 24, and H/D_h=10.

As the outflow grows, the vortices decrease from their peak vorticity value, but their overall strength remains nearly constant.

Figure 27a shows the transverse vorticity profile at the center of the vortices at different phase angles for $H/D_h = 10$. The vorticity reaches its maximum value at $\Phi = 45^o$, and it decreases at later phase angles. However, the total vortex circulation does not change significantly, as seen in Figure 27b. In this figure, the total circulation is calculated within circular regions about the center of the vortex on the left side of the orifice. As the circle radius is increased, it contains more of the vortex, eventually reaching a plateau at its edge. For these same four phase angles, the peak circulation is nearly the same, even though the vortex radius grows by approximately three times. Hence, the vortices maintain their strength throughout the ejection stroke.

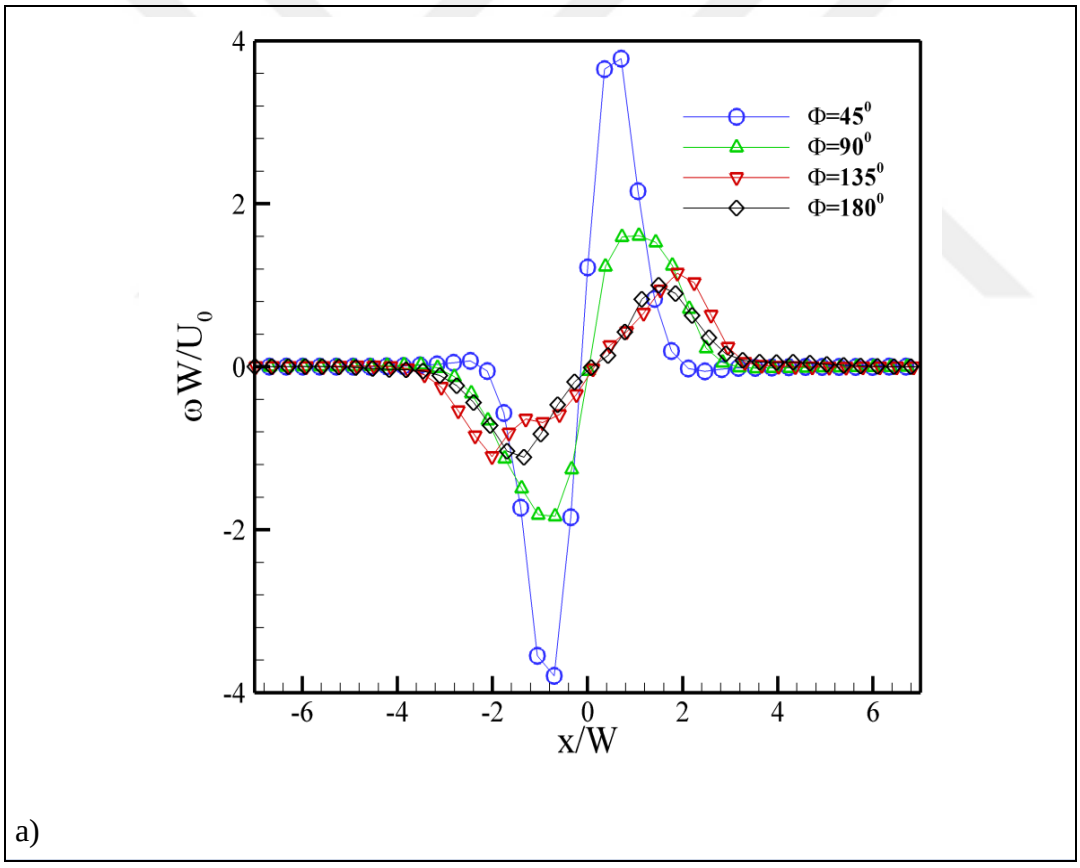

a)

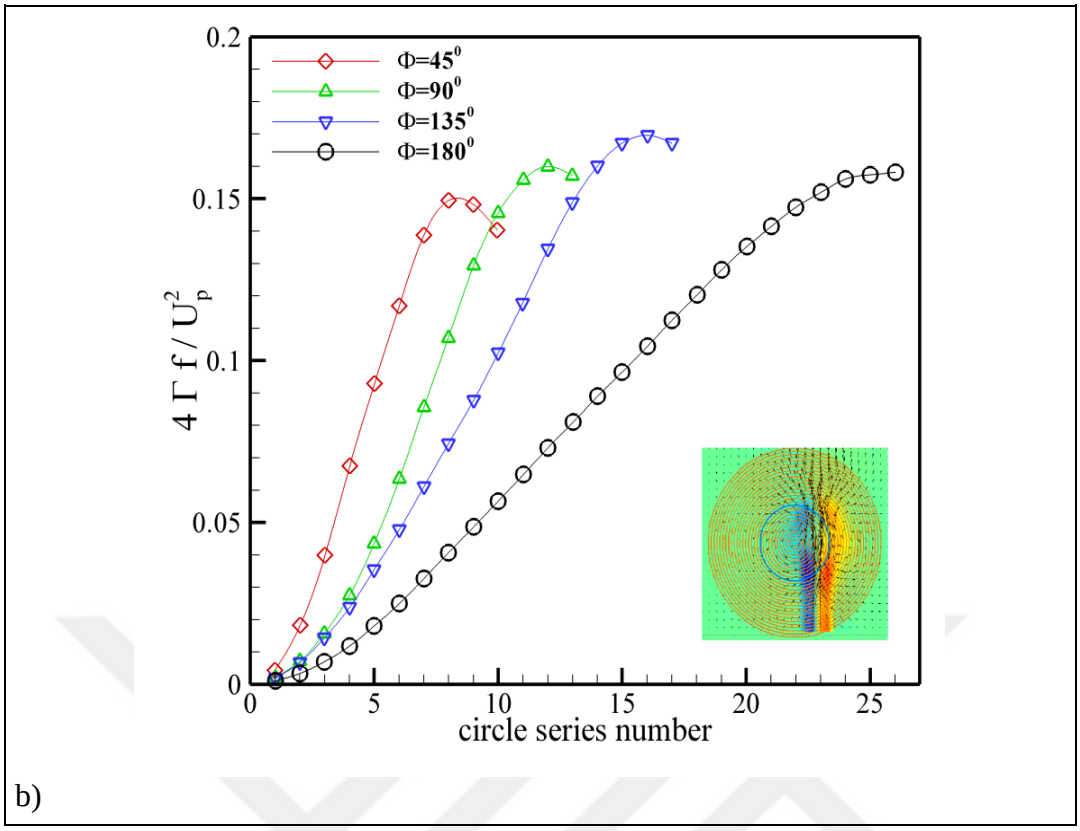

Figure 27:a.) Nondimensional, transverse vorticity profiles at the center of the vortices at different ejection phase angles at H/D_h = 10 and b.) Nondimensional circulation within circles of increasing radii about the left vortex at different phase angles.

Figures 28a and 28b show the time averaged vorticity and velocity contours, respectively, at H/D_h = 10. Much like the free synthetic jet, shown earlier in Figure 22, the flow is symmetric, growing in width as it travels downstream. Unlike the free jet, there are two strong regions of vorticity next to the wall. The peak vorticity magnitudes of this near wall region are nearly the same strength as that of the jet near the orifice.

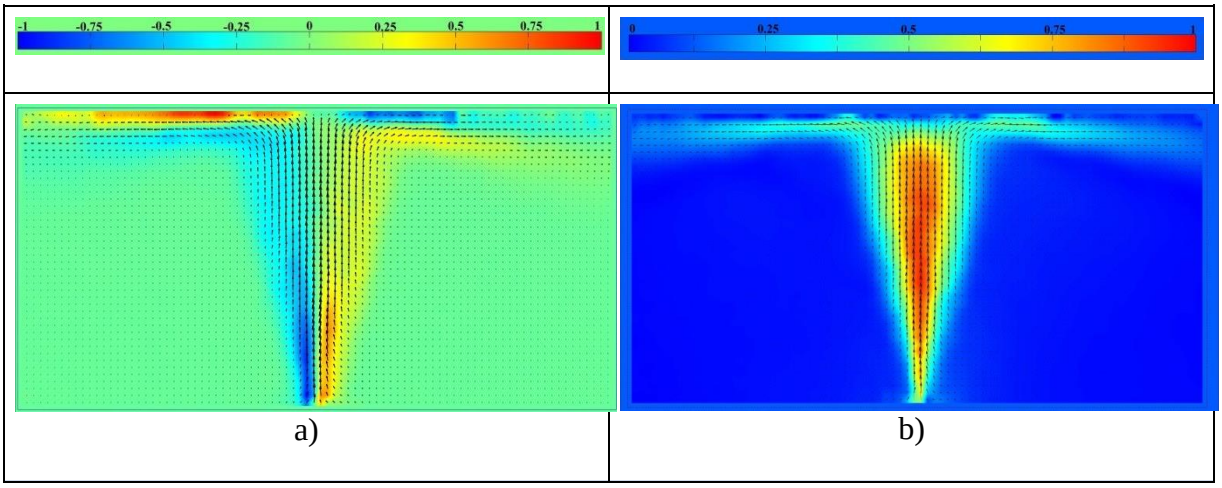

Figure 28a.) Time-averaged vorticity contours, $\omega W/U_0$, and b.) Velocity contours, U/U_0 for an impinging slot synthetic jet at Re_{U0} = 900 at H/D_h=10

For this synthetic jet, the time-averaged velocity contours have considerable differences when compared to a conventional impinging jet. Notably, the centerline velocity does not show degradation for 3.5< y/D_h < 6.5, as displayed in Figure 29a. This is slightly nearer to the plateau seen for the free synthetic jet in Figure 23a, indicating that the wall does influence the time-averaged profile. The velocity experiences a sharp decrease for y/D_h > 8 and reaches zero at the stagnation point. Along the wall, there is a wall jet, as shown in Figure 29b. This plots the distribution of the time-averaged wall jet velocity profile at x/W=15, along with comparisons to self-similar laminar and turbulent wall jets [49,50]In this figure, the velocity is normalized by the local maximum, while the vertical position is normalized by the half-width of the wall jet. The inner region has a steeper slope compared to the laminar jet, and its profile falls between the laminar and turbulent wall jets. The outer region shows similar behavior to the laminar wall jet. Hence, the velocity profile differs from both the laminar and turbulent steady wall jet.

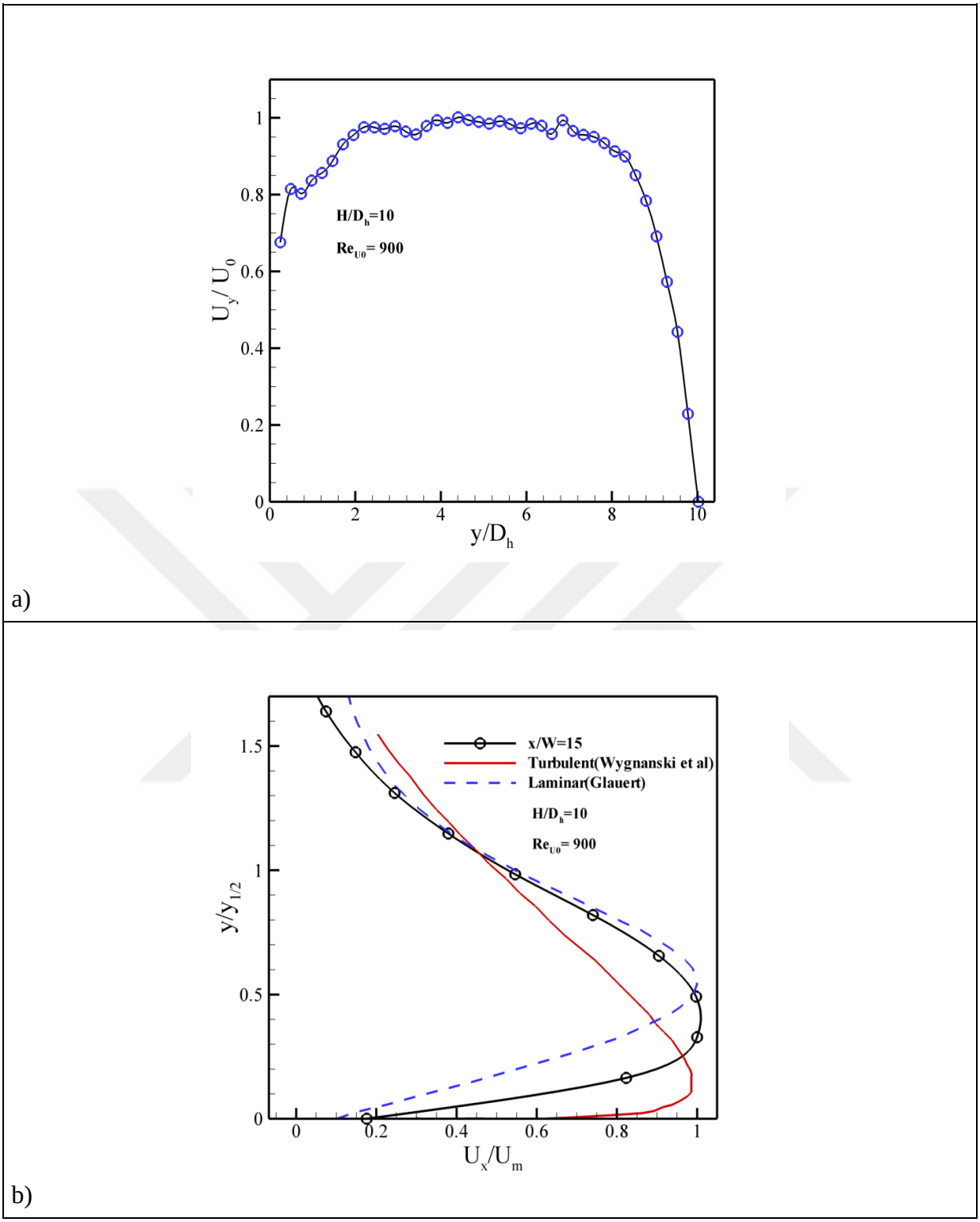

Figure 29: a) Streamwise variation of normalized, time-averaged centerline velocity for the impinging jet at H/D_h = 10 and b.) Normalized wall velocity profile compared to self-similar laminar and fully turbulent wall jets.

The previous PIV measurements consider the resonant response at 450 Hz. However, there is a second peak in the synthetic jet flow response at 2000 Hz, albeit with high acoustic noise. Figure 30 depicts the instantaneous vorticity and velocity profiles for an image pair acquired at f = 2000 Hz and H/D_h = 5. At this condition, Reynolds number, Re_{U0} = 890, is nearly the same, but the Stokes number, S = 50, is much larger. A close examination of the image reveals that there are two sets of strong vortices located between the orifice and impinging plate, as opposed to the single pair at the lower frequency. When comparing the vorticities at f = 450 Hz and 2000 Hz, the peak is higher at the lower frequency, as seen in Figure 8. The instantaneous peak velocity and Re_{Up} are also higher at 450 Hz. However, the increased number of vortices at f = 2000 Hz leads the jet to have almost the same Re_{Uo}. This has an impact on the heat transfer performance, as will be shown later. This reveals that flows with identical Re_{Uo} may have markedly different flow responses, justifying the importance of Stokes number.

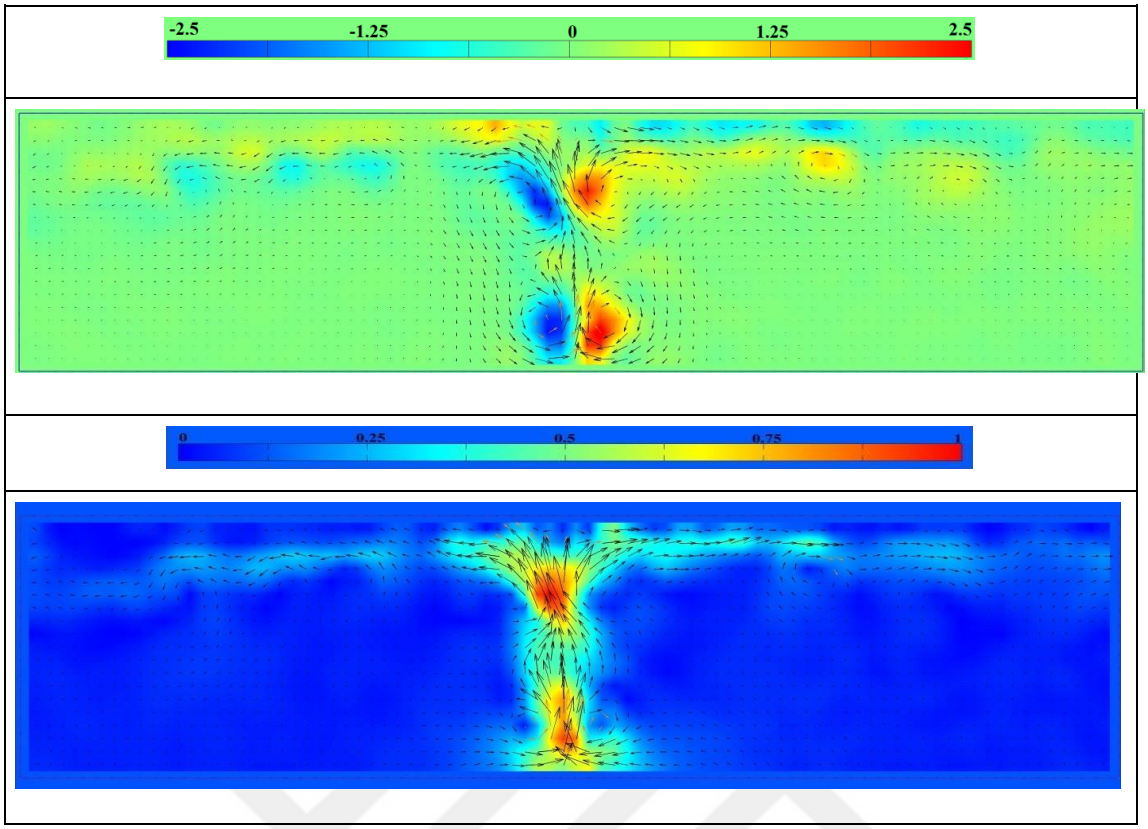

Figure 30: a.) Non-dimensional instantaneous vorticity contours, $\omega D/U_0$, and b.) Velocity (U/U_p) contours for an impinging jet at $Re_{U0} = 890$, $S = 50$, and $H/D_h = 5$.

In the next part we will investigate the effect of the frequency on the flow response of the slot synthetic jet.

3.3 Frequency-dependent flow response

We have conducted an experimental study of the fluid dynamics for a slot synthetic jet at different operating frequencies. Using phase-locked PIV, we have examined the transient flow response of a jet impinging onto a perpendicular surface located at the optimal location for heat transfer. We considered the response at four different frequencies – two cases where the heat transfer reaches a peak, and two cases off of the resonant peak. We particularly examine the motion and strength of the vortex pair generated by the jet, which differs

significantly depending on the frequency. By studying this flow response, we can determine appropriate conditions for slot synthetic jet applications.

3.3.1 Phase-locked resonant flow

The flow response was examined through phase-locked PIV measurements at different actuator frequencies. Figure 31 displays the phase-averaged velocity magnitudes and vectors for the resonant condition at 450 Hz at phases spaced 45° apart. In the figure, the phases begin with the onset of outflow, followed by the ejection of the vortex pair. As noted earlier, the phases are synchronized to the piezoelectric disk deflection, rather than the flow ejection.For this condition, the outflow begins 135° after the mechanical deflection commences.The actuator orifice is located at the bottom center of each image window. A reference vector is shown in the upper right of each sub-figure, depicting a length equal to the average outstroke velocity.At the beginning of the outstroke, shown in Fig. 31a, the initial outflow is seen very near the orifice. There is weak upward flow towards the wall along the centerline, which splits symmetrically at the stagnation point. Two counter-rotating vortices are located approximately $4D_h$ away from the centerline, and another smaller pair of vortices are slightly further out. On either side of the centerline, the eddies have the same rotational direction. As will be seen, these are the remnants of the previous two pulses.

Continuing the outstroke, a vortex pair is generated at the orifice, as seen in Fig. 31b. The peak speed is approximately 26 m/s, which agrees with the hot wire measurements (see chapter 2). At the instant shown, the leading edge of the vortex pair has traveled less than half of the distance to the wall, but speeds remain positive along the entire centerline. This is still a residual flow toward the wall from the previous jet pulses, though. At the wall, the flow stagnates, and there is symmetric outflow along the wall towards the secondary vortices seen earlier.

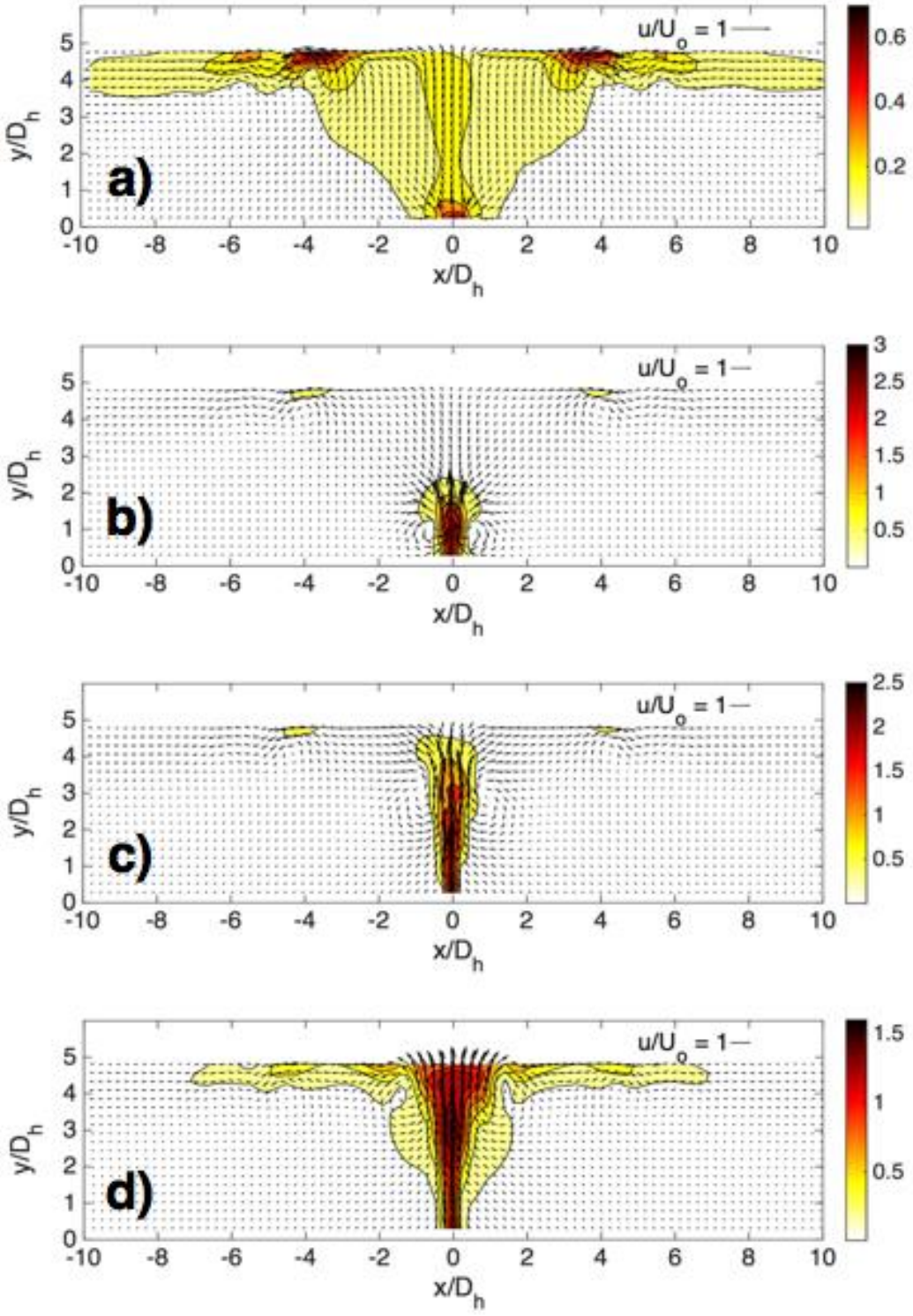
a)
b)
c)
d)
u/U_o = 1
y/D_h
x/D_h

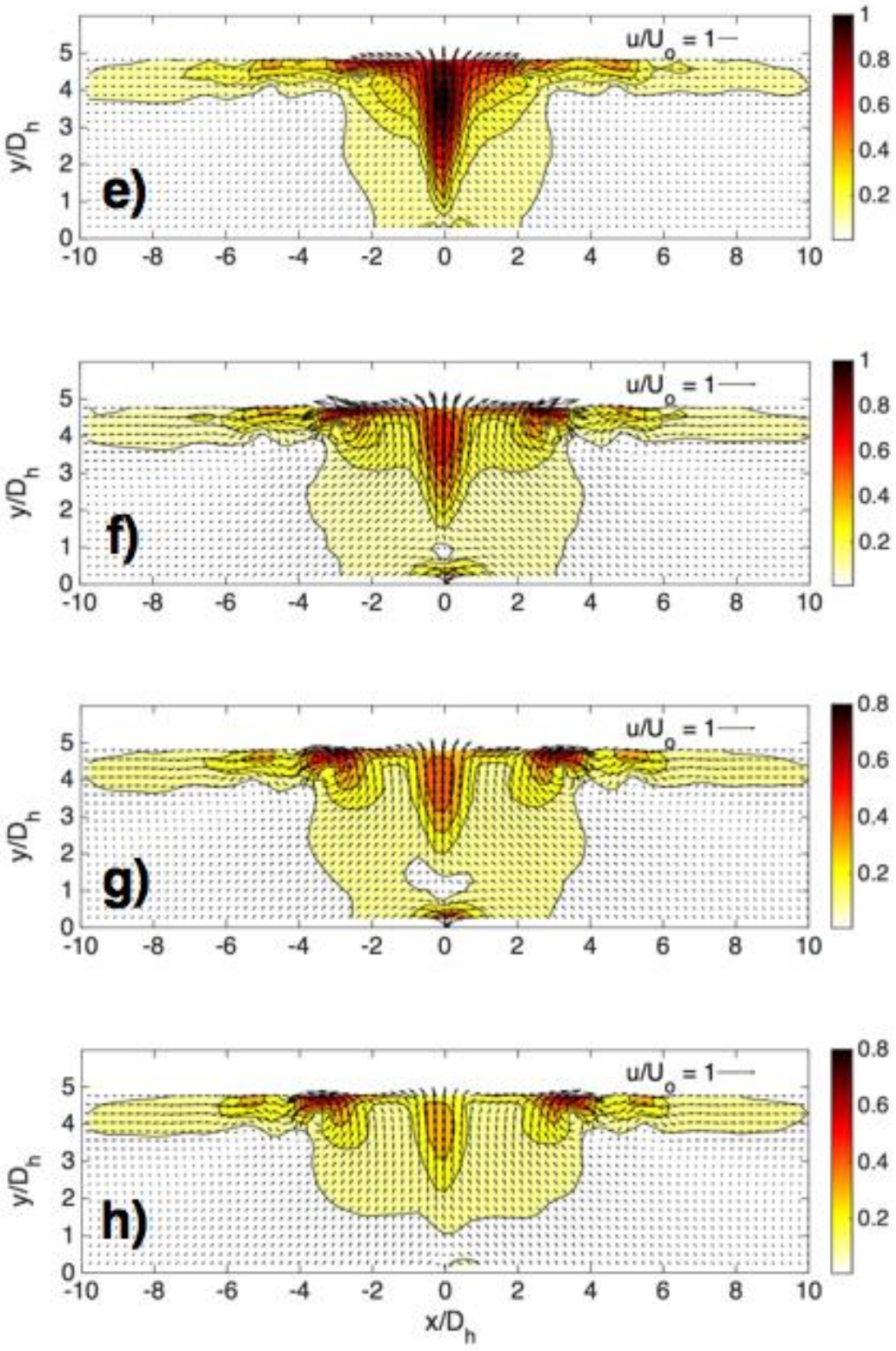

Figure 31.Phase-averaged transient response for the impinging flow from the actuator at the 450 Hz resonant condition. Eight separate phases are shown, spaced 45° apart. The first phase shows the onset of outflow, which occurs 135° out of phase with the piezoelectric

driving signal. Velocity contours and vectors are normalized by the average outstroke velocity, U_o.

In the next phase, shown in Fig. 31c, the vortex pair moves towards the wall, maintaining significant strength. There is a trailing jet attached to the orifice, an indication that the outstroke is continuing to supply momentum. At the wall, there is more significant stagnation flow, and the secondary vortices have traveled slightly further from the centerline. By the subsequent phase, 135° after ejection, the vortex has struck the wall, as seen in Fig. 31d. The trailing jet persists, but its speeds are growing weaker as the outflow tapers off. The outflow has terminated in the next phase, displayed in Fig. 31e, with speeds near zero right at the orifice. The primary vortex pair is distorted as it impinges on the wall, stretching parallel to it and compressing normally. The trailing jet is still present, but it is no longer supplied with fluid at the orifice.

During the instroke, shown in Figs. 31e through 31h, the flow near the wall is distinct from that near the orifice. At the wall, the primary vortices become more concentrated, with smaller radii and higher peak vorticities. Velocities along the wall itself are significant, producing a wall jet that should aid in convective heat transfer. This jet steadily advects the primary vortex pair away from the centerline, and the preceding secondary vortices continue outward as well. The trailing jet continues to supply flow towards the stagnation point during the instroke, though the magnitude gradually weakens. Nearer to the orifice, there is sink flow seen in the middle phases of the instroke, shown most clearly in Figs. 31f and 31g. The sink flow is negligible at 315° of phase after ejection, as seen in Fig. 31h, marking the end of the instroke.

Figure 32 shows the phase-averaged centerline velocities for this resonant case, further displaying the pattern described earlier. As the vortex pair travels towards the wall, the centerline speeds are fairly uniform in the trailing jet, with magnitudes approximately three

times the average outstroke velocity, U_o. The centerline speeds fall gradually due to the decreasing supply and growth of the jet width. At a phase 180° after ejection, corresponding to Fig. 31e, the centerline speed is near zero at the orifice. During the instroke, centerline velocities are negative at the orifice, peaking at approximately half the average outstroke velocity. The downstream velocities are less than one-quarter of this average speed, but still nonzero towards the wall. The difference between peak outstroke and instroke velocities is not an indication of nonzero mass flow, as the jet flow occurs over a smaller cross-sectional area than the sink.

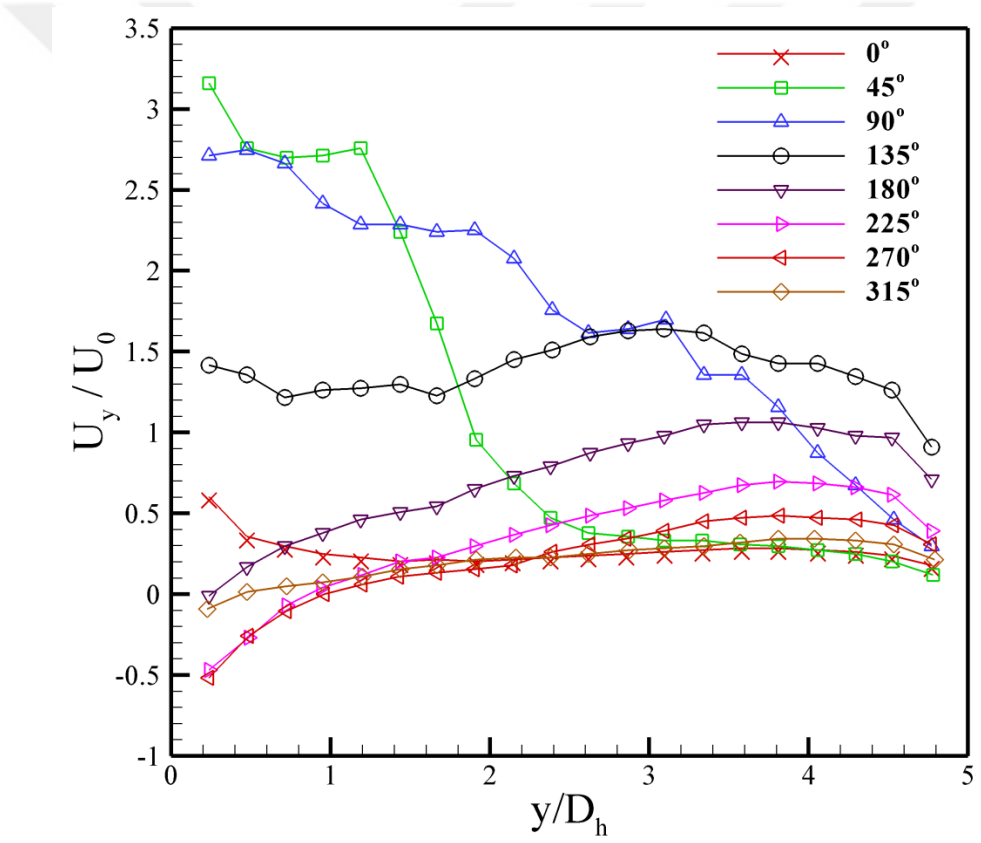

Figure 32Phase-averaged centerline velocities at the resonant condition, 450 Hz, normalized by the average outstroke velocity.

3.3.2 Phase-locked off-resonant flow

The same phase-locked experiments were conducted at two other actuator frequencies, 350 Hz and 600 Hz, which had similar heat transfer in earlier impingement tests. Much of the flow response was comparable to that at 450 Hz, especially for the lower frequency, though some key distinctions will be discussed below. Figures 33 and 34 display the phase-averaged centerline velocities at 350 Hz ("sub-resonant") and 600 Hz ("super-resonant"), respectively. In each case, the phase is defined based on the onset of the outflow, which does not necessarily coincide with the motion of the piezoelectric disk. Here, the outflow begins 90° after the mechanical deflection commences at 350 Hz, while it begins 180° after at 600 Hz.

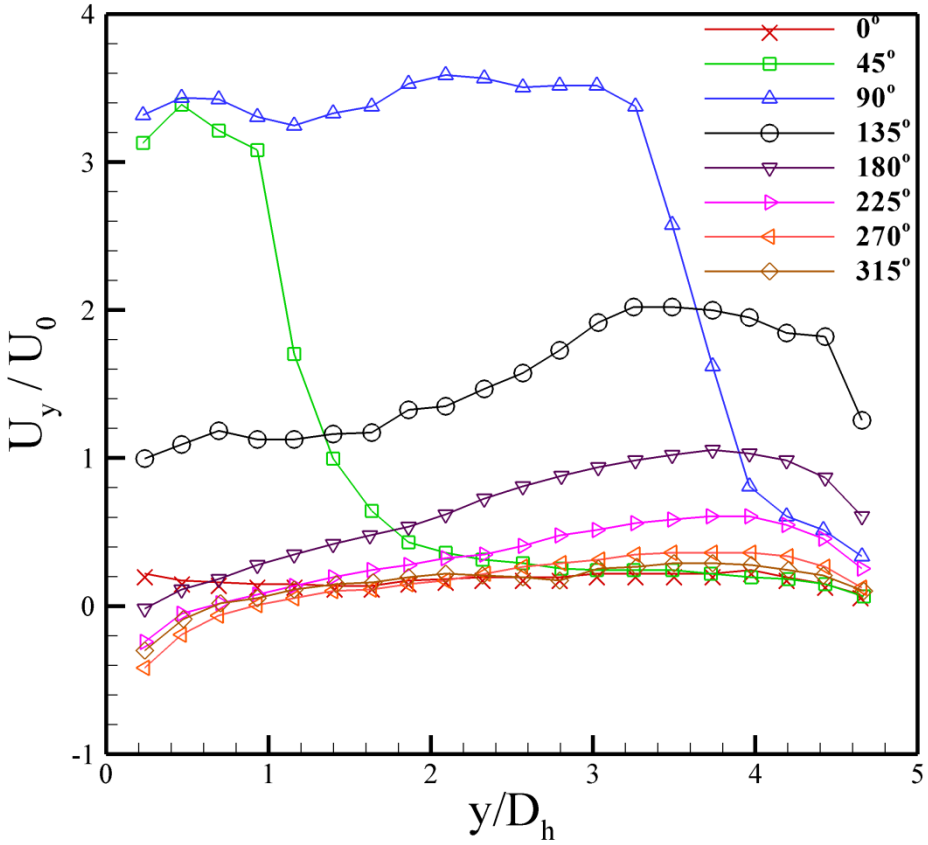

Figure 33.Phase-averaged centerline velocities at a frequency below the resonant condition, 350 Hz, normalized by the average outstroke velocity.

For the case below the resonant frequency, shown in Figure 33, there is a strong initial pulse ejected from the orifice. The peak nondimensional velocity is similar to that at resonance, reaching just over three times the average outstroke velocity. There is a trailing jet behind the leading edge of the pulse, which maintains the same nondimensional speed all the way to the wall. This does deviate slightly from the resonant case, where the trailing jet started to weaken prior to impact. As before, the pulse reaches the wall by 135° after the outflow begins. After impact, the trailing jet continues to impinge on the wall during the instroke, again similar to the resonant case.

In fact, the overall nondimensional behavior seems qualitatively unchanged from resonance. The primary difference, of course, is that the Reynolds number is near 20% lower, as seen in table 4. This should result in a reduced heat transfer, as it will be seen in the next chapter.

Above the resonant frequency, as displayed in Figure 34 the flow response is markedly different. Although the initial pulse has a similar nondimensional velocity at $U_y/U_o \sim 3$, the pulse length is much smaller in the streamwise direction. As opposed to a trailing jet that extends across the entire jet-to-surface spacing, this pulse only extends approximately one hydraulic diameter in length. The pulse weakens gradually as it approaches the wall, with its peak speed less than the average outstroke velocity Uo when it reaches it. In addition, the approach is much slower than at the resonant or sub-resonant conditions, as the pulse does not reach the wall prior to the next outstroke. Thus, at this frequency, there are typically two vortices between the orifice and the impingement surface, rather than just one at lower frequencies. It is likely that this additional vortex aids in sustaining the heat transfer at this super-resonant case, in spite of its lower Reynolds number.

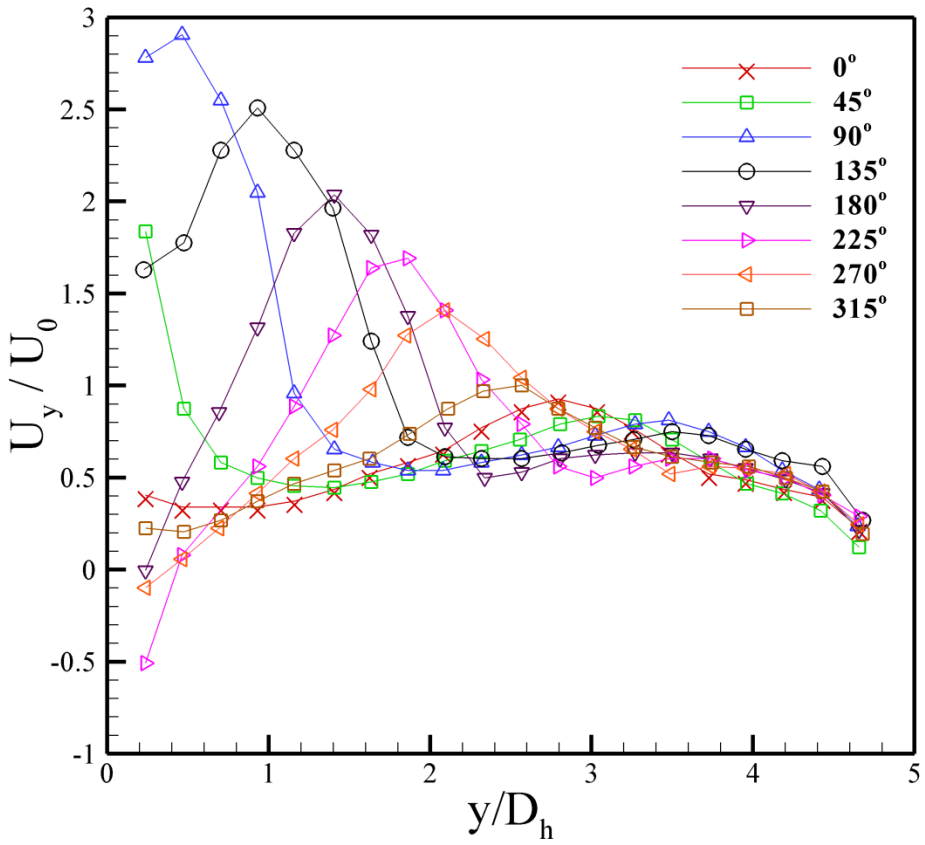

Figure 34. Phase-averaged centerline velocities at a frequency above the resonant condition, 600 Hz, normalized by the average outstroke velocity.

As seen in Table 4, Re_{Uo} is 80% and 50% less than the resonant and sub-resonant cases, respectively. However, the Nusselt number is only 30% less than resonant, while being nearly identical to the sub-resonant case (as we will see in the next chapter).

This response is further elucidated by examining the flow just after the vortex ejection at each of these frequencies. Figure 35 displays the phase-averaged vorticity contours for the phase immediately after vortex ejection for each case. Here, the vorticity is nondimensionalized using the hydraulic diameter, D_h, and the average outstroke velocity, U_o.

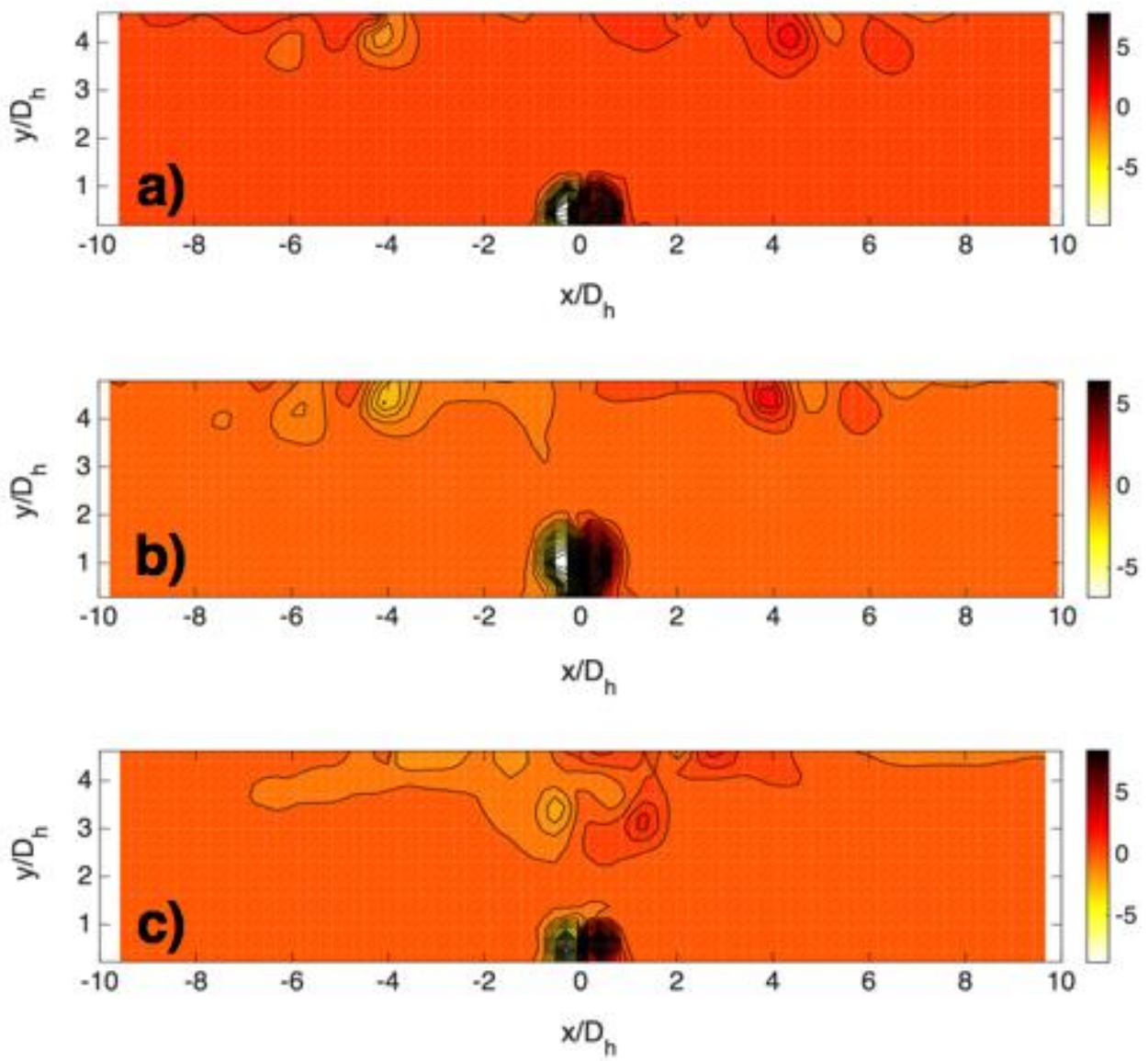

Figure 35.Phase-averaged vorticity contours for the impinging flow from the actuator at the phase just after vortex ejection at a) 350 Hz, b) 450 Hz, and c) 600 Hz (contours are normalized by the hydraulic diameter, D_h, and average ejection velocity, U_o)

The peak vorticities have a similar nondimensional level in all three cases. For the sub-resonant and resonant cases, shown in Figs. 35a and 35b, the secondary vortices are in nearly the same position, along the wall approximately 4 hydraulic diameters from the centerline. The vortex is slightly further out at the lower frequency. Nondimensional vorticities are also

nearly unchanged for these secondary vortices. However, the secondary vortex location is significantly different for the super-resonant case, shown in Fig. 35c. Here, the vortex is still nearly 2 hydraulic diameters away from the wall, and it is only slightly greater than one hydraulic diameter from the centerline. More intriguingly, the next secondary vortex out is still closer to the centerline than those seen at lower frequencies. Clearly, the vortex pairs travel much more slowly at frequencies above resonance, with multiple eddies located close to the centerline.

Figure 36 shows the path for the peak vorticity at each of the three frequencies, which is determined from the phase-averaged vector fields

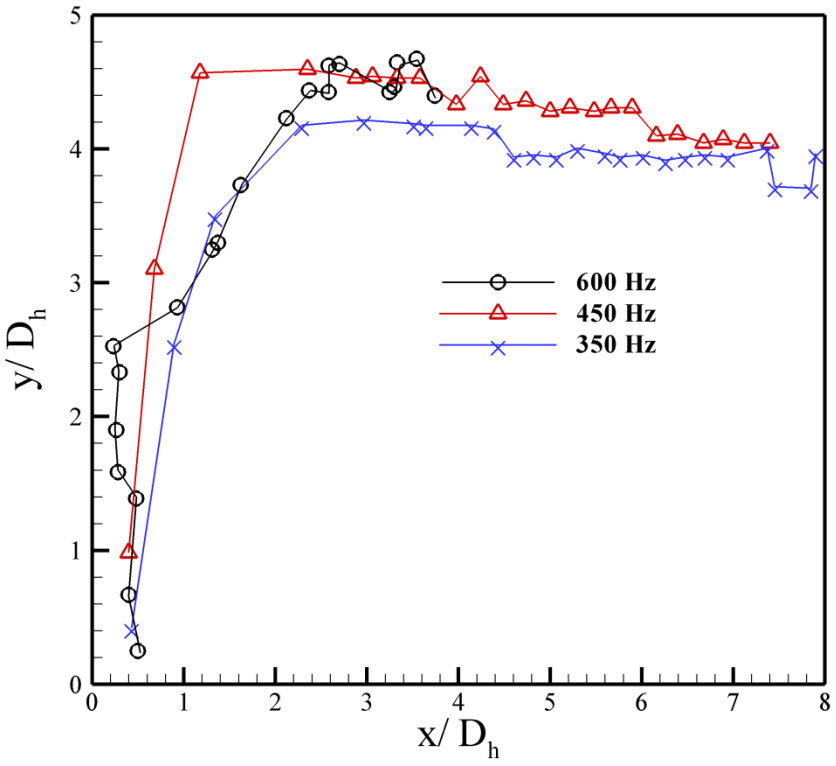

Figure 36.Paths for the location of peak vorticity for each of the three frequencies over three synthetic jet cycles, as determined from the locations of the three highest vorticity peaks in the phase-averaged flow fields.

Although only eight phases were acquired, 24 positions are displayed for each case, using the secondary and tertiary vortex locations to describe the continuing path over two more cycles.

Figure 37 displays the nondimensional vorticity at the peak versus phase, again showing the first three cycles along the vortex path. We follow the motion of the vortex on the right-hand side of the centerline, although the response is nearly symmetric on both sides. Note that peak vorticity should not be construed as the vortex strength, as the spatial extent of the vortex increases during the ejection stroke. When integrating the total circulation about the vortex, the total is essentially constant for the vortex as it travels from the orifice to the wall.

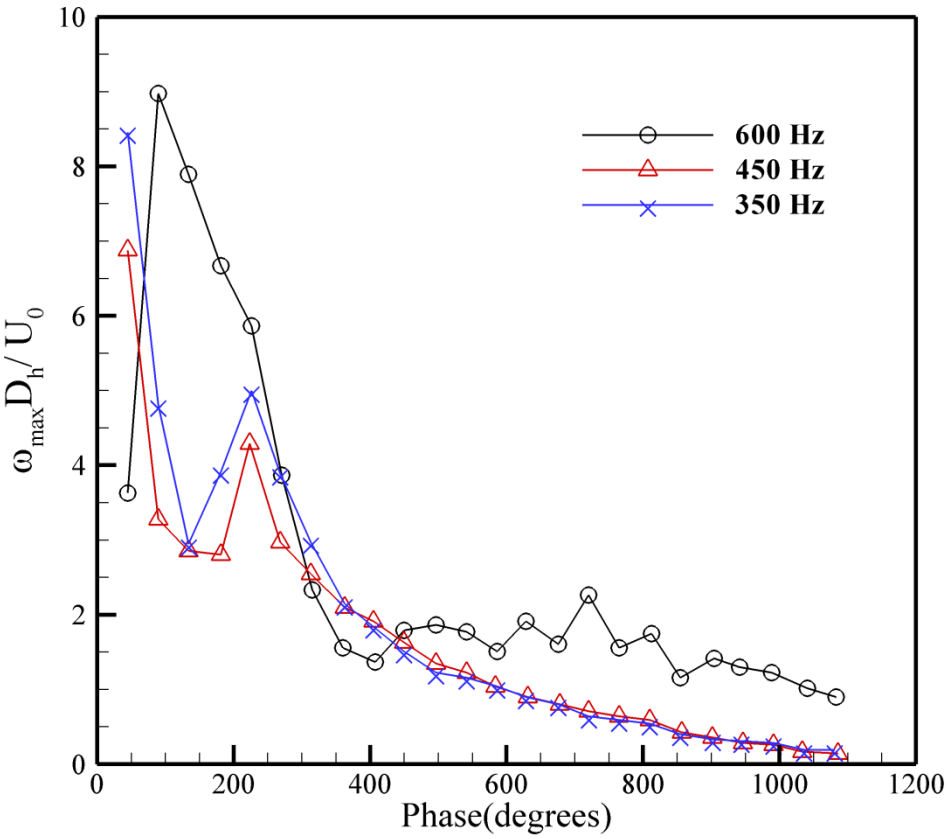

Figure 37:Maximum nondimensional vorticity versus synthetic jet phase for each of the three frequencies.

While these three cases have different Reynolds numbers, the nondimensional vorticity peaks at similar values, with $\omega_{max}D_h/U_o \sim 8$. Once again, the sub-resonant and resonant cases are very similar, with the curves agreeing within the uncertainty of the measurements for all phases after the first 360° cycle. After the initial peak during ejection, the maximum vorticity

falls as the vortex approaches the wall. There is a second peak after impingement, suggesting that the eddy concentrates again to a smaller size, as seen directly in Figure 31f.

The super-resonant case responds quite differently, with its peak vorticity reached at a later phase of 90°. This peak falls more slowly, suggesting that the vortex is remaining more concentrated during this first cycle when compared to lower frequency actuation. Once the peak vorticity falls to the same level as the other frequencies, the magnitude remains relatively constant for the remainder of the phases considered. The lower frequency vorticities are still gradually decreasing; indicating that these eddies would have less influence at later phases.

3.3.3. Time-averaged flow

While the phase-locked response has both jet and sink flows near the orifice, the time-averaged response does display an axial jet. Figure 38 shows the ensemble-averaged velocity profiles in the streamwise direction at several axial positions for the resonant case. These profiles were determined using 500 image pairs acquired at random instants in the motion, although they agree well with the ensemble-average of the eight separate phases shown in Figure 31.

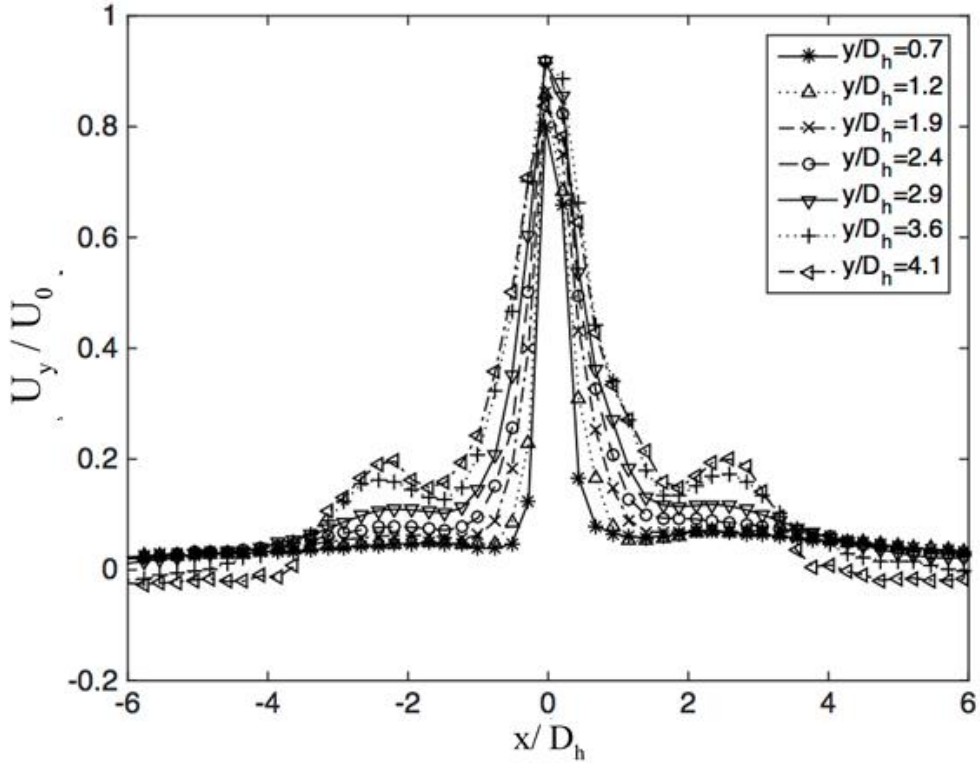

Figure 38. Ensemble-averaged streamwise velocity profiles at various axial locations at the resonant condition, 450 Hz, normalized by the average outstroke velocity.

Along the centerline, there is a clear peak, whose maximum velocity is more than 80% of the average outstroke velocity. This peak speed does not change significantly over the range of axial positions shown here, differing by less than 15%. Hence, along the centerline, there is a nearly constant speed jet in the time average. This jet grows gradually, with its half width nearly tripling between the orifice and the wall. More importantly, the velocity profile has a second peak on either side of the centerline, which grows in strength near the wall. These peaks coincide approximately with the secondary vortices seen during the instroke in Figs. 311e through 311h, as they recirculate flow back towards the wall. This secondary peak is also seen in pressure and heat transfer simulations of a two-dimensional slot jet (seen CFD modeling in the next chapter). Further away from the centerline, the near wall flow is directed back away from the surface, as would be expected in the growing boundary layer.

When comparing to other frequencies, there are distinct differences in cases below and above this resonant frequency, particularly in the transverse profiles. Figure 39 displays time-averaged transverse and centerline profiles at each of the four frequencies considered. This includes measurements from a second resonant peak at 2000 Hz, which has high speeds but also significant acoustic noise.

In the transverse direction, each of the cases has a clear peak near the centerline, as seen in Fig. 39a. At resonance and below, there is a single secondary peak located near the secondary vortices seen during the instroke, with similar nondimensional speeds and positions. Above resonance, the profile is significantly wider near the wall, and more than two velocity peaks are seen on either side of the centerline. At the super-resonant frequency, 600 Hz, this additional peak is located near the tertiary vortex seen in the phase-averaged measurements. These additional vortices produce recirculation towards the wall, widening the impact of the jet to more than 5 hydraulic diameters from the centerline. Hence, the impingement effects are distributed over a larger region when additional vortices are located between the orifice and the wall. Instantaneous velocity fields at the higher resonant frequency, 2000 Hz, also had multiple vortices between along the centerline.

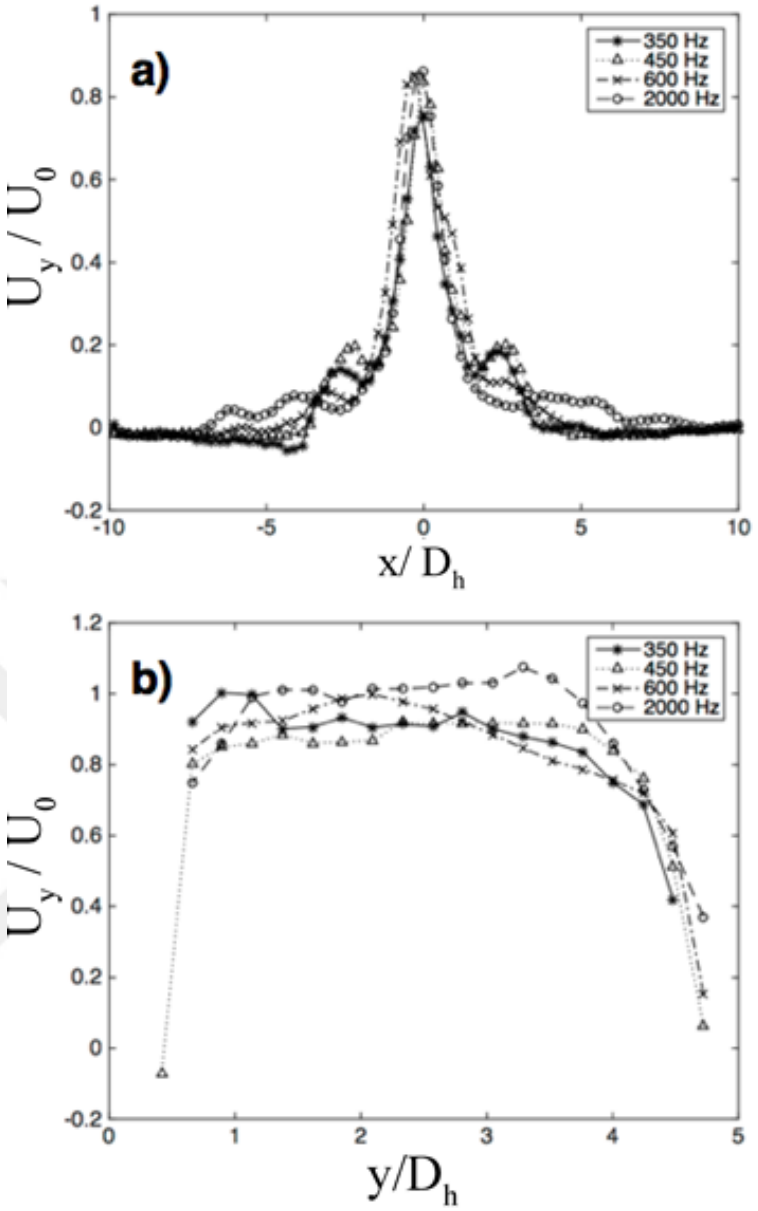

Figure 39.Time-averaged velocity profiles at various frequencies for a) A near-wall transverse location at y/D_h = 4.1 and b) Along the centerline, normalized by the average outstroke velocity

Along the centerline, shown in Figure. 39b, the velocity profile is fairly uniform between the orifice and the wall at all frequencies. The velocities fall sharply to zero at either end, indicative of zero mass flux at the jet orifice and stagnation at the wall. At the two high-speed, resonant cases, the velocity profile remains at a plateau throughout the rest of the

distance. Off of resonance, the velocity profile begins to drop further away from the wall. This is particularly true at the super-resonant case at 600 Hz, where speeds drop approximately two hydraulic diameters from the wall. This is likely because the instroke begins prior to the vortex pair reaching the wall, slowing its approach.

3.3.4 Discussion on frequency-dependent flow response

There are several aspects of the frequency-dependent synthetic jet that warrant further discussion. These include the importance of Reynolds number, sub-resonant and super-resonant response, the corresponding critical conditions, and fluid/structure coupling. Each of these issues will be elaborated below.

First, at the most basic level, the flow measurements demonstrate the direct relationship between Reynolds number and Nusselt number. The highest heat transfer measurements occur at the two resonant peaks (seen in the next chapter), which correspond to the highest Reynolds numbers based on average outflow velocity, Re_{U_o}. As seen in Figure 39b, these speeds are also maintained over most of the jet-to-surface distance. However, a simple correlation between Nu and Re_{U_o} may oversimplify the situation, as there are distinct differences between these cases, shown in Table 4. Notably, their Stokes numbers and peak Reynolds numbers differ by approximately a factor of two. Further, the off-resonant cases have very different Reynolds numbers, yet their Nusselt numbers are nearly identical. Clearly, a general heat transfer correlation must include more variables than simply the Reynolds number, as suggested previously by Persoons et al. [13].

Second, at the resonant condition and below, the nondimensional flow behavior is the same. In each cycle, a single vortex pair is generated. This pair approaches the wall during the outstroke, and then each vortex advects outward along the wall. The vortex path and nondimensional strength are also nearly identical at these frequencies. Although the vortices

travel more slowly off of resonance, they arrive at the wall at a similar phase due to the lower frequency. Hence, there is still only one vortex between the orifice and the wall during each cycle.

Third, at frequencies above the first resonant peak, the flow structure is significantly different. In between the orifice and the wall, there are two vortices present at all phases. These remain nearer to the centerline for a longer time, so they have a more sustained influence on a heated surface during impingement cooling. The jet pulses are shorter and have lower peak speeds, yet the heat transfer is comparable to the sub-resonant condition. This is very likely due to the sustained presence of the vortices, which lead to improved mixing and broader impingement of near-wall fluid onto the wall. Hence, this explains why this off-resonant condition can produce similar thermal performance without the concerns of acoustic noise.

Fourth, this behavior indicates that orifice-to-wall spacing strongly impacts the response, since greater distances may permit additional intermediate vortices. There will be a critical distance demarcating when the flow increases from one vortex pair to two, changing the flow dynamics and cooling behavior. As seen in Figures 32 and 33, the vortex pair reaches the wall at approximately the same phase for the resonant and sub-resonant cases, in spite of the difference in Re numbers. This similarity can be displayed by comparing the time scale for the vortex advection to the wall, $t_{adv} = H/U_o$, to the duration of the outstroke, $t_{out} = \frac{1}{2}f$. The ratio of these scales is a form of the Strouhal number, $St = t_{adv}/t_{out} = 2fH/U_o$. At the resonant and sub-resonant cases, the Strouhal numbers are 1.01 and 0.97, respectively, which clearly shows their similarity. In both of these cases, the vortex should reach the wall right at the end of the outstroke. This provides another reason why the resonant case gives the best heat transfer, as the wall spacing is well tuned to the outstroke duration.

For the super-resonant case, St = 2.4, which indicates that the time required to advect to the wall is significantly longer than the outstroke. Thus, another vortex pair is generated prior to

reaching the wall. In order for the jet to behave similar to the lower frequency cases, the jet-to-wall spacing must be reduced. The critical distance where the behavior changes is approximately $H_{crit} = U_o/2f$, assuming that the flow changes at a Strouhal number of one. Therefore, the super-resonant case would behave similarly if the wall spacing was reduced, with $H_{crit}/D_h = U_o/2fD_h = 2.1$. In principle, this reduction agrees with the findings of Pavlova and Amitay [12], who showed better heat transfer at small distances with higher frequency. However, their study considered two different resonant frequencies, where the flow patterns were already distinctly different. In the case here, the resonant and sub-resonant cases have similar structure and transient behavior. Obviously, this Strouhal number scaling cannot continue indefinitely as frequency increases, since eventually the wall proximity will prevent effective vortex growth [28].

Fifth, there is an intriguing deviation between the measured flows and the mechanical motion of the actuator at each phase. It is not surprising that there is a phase shift between the outflow and the actuator deflection, since the fluid dynamics depend on multiple structural and cavity features. Around the resonant peak, the phase shift changes, suggesting that the fluid/structural coupling is very sensitive to input conditions. On the positive side, this also suggests that this coupling could be exploited through careful selection of actuator driving conditions, as evidenced by the dramatic differences in flow speeds seen with the synthetic jet.

CHAPTER IV

SYNTHETIC JETS HEAT TRANSFER

4.1Slot synthetic jet heat transfer results

Figure 40 shows the experimental results for the average Nusselt number at different jet-to-surface spacings at the resonant condition of 450 Hz. The average Nusselt number is increasing rapidly up to $H/D_h = 5$. There is a fairly flat maximum region for $5 \leq H/D_h \leq 10$, followed by a gradual decay for $H/D_h > 10$. This will create design and placement flexibility in practical applications.

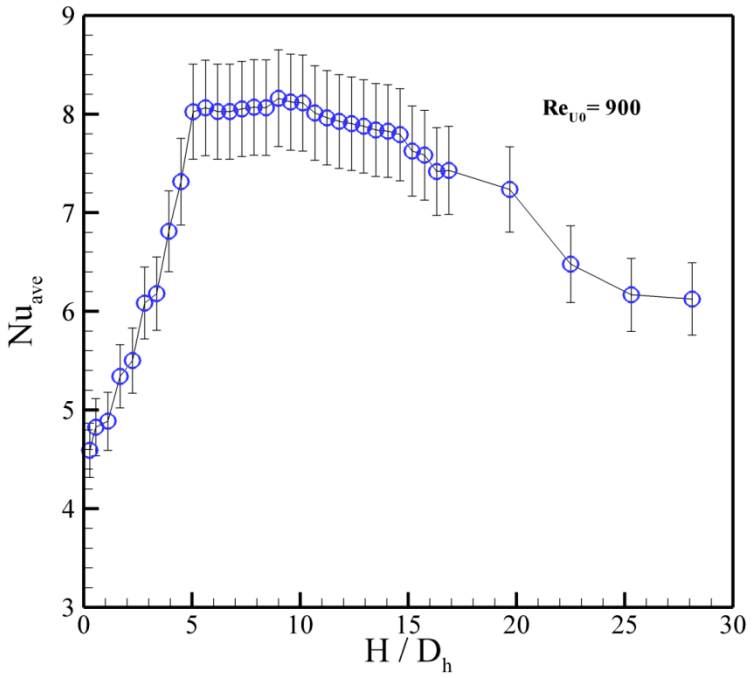

Figure 40.Variation of average Nusselt number with different jet-to-surface spacings at 450 Hz and $Re_{U0} = 900$

The decreased heat transfer near the surface is due to the reduced growth of the vortices, as they strike the wall prior to detachment from the orifice, as seen in Figure 24. In addition,

there is re-entrainment of the warm air next to impinging plate back into the jet flow, and some warm air is sucked by into the orifice during the suction stroke. The maximum heat transfer occurred at $5 \leq H/D_h \leq 10$, which is the region dominated by coherent vortex structures. At these jet-to-surface spacings, the vortex pair does not detach from the orifice prior to striking the wall, resulting in stronger eddies. The vortices have a significant effect on the wall profile, disturbing the boundary layer next to the wall and aiding in convective heat transfer. It is likely that the jet experiences 3-D edge effects for $H/D_h > 10$, reducing the coherence of the ejected structures. Finally, the flow may transition from the regime dominated by coherent structures into a condition dominated by stochastic turbulence, which may affect the mixing scale [51].

Figure 41 shows the variation of average Nusselt number versus frequency at $H/D_h = 5$. The heat transfer peaks at $f = 450$ Hz and 2000 Hz, which match with the first and third peaks observed in the deflection measurements of the actuator. At these two operating conditions, Re_{U0} number is almost the same, but the Stokes number differs. The case with the higher Stokes number, with $S = 50$, had slightly better heat transfer. This is likely because of the more rapid production of coherent vortices, as seen in Figure 30. As a consequence, the wall boundary layer is disturbed more significantly, and heat transfer increases.

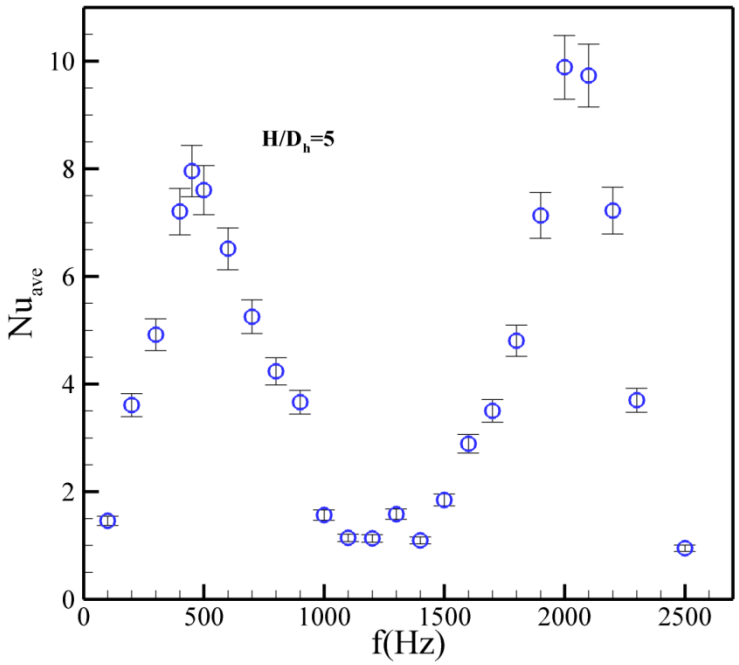

Figure 41.Variation of average Nu number with frequency for an impinging slot synthetic jet at H/D_h = 5

Finally, whenever considering the performance of a new thermal management method, the required energy consumption must also be examined. Ideally, new techniques should require minimal input energy while producing significant heat transfer. This leads to a large coefficient of performance (*COP*) [52], defined as:

$$COP = \frac{\bar{h}A_s.(T_w - T_{amb})}{Driving\ Power} \quad (10)$$

Figure 42 shows the variation of *COP* at different frequencies for H/D_h = 5. Here, the highest *COP* is 14 at *f* = 450 Hz, suggesting that this may be the optimal condition. There is also a second peak at *f* = 2000 Hz, but its magnitude is significantly lower. Thus, even though the heat transfer is higher at *f* = 2000 Hz, the additional power consumption at this operating condition makes it less appealing. Beyond this issue, the noise level at *f* = 2000 Hz was so high that it would be less practical for real life applications.

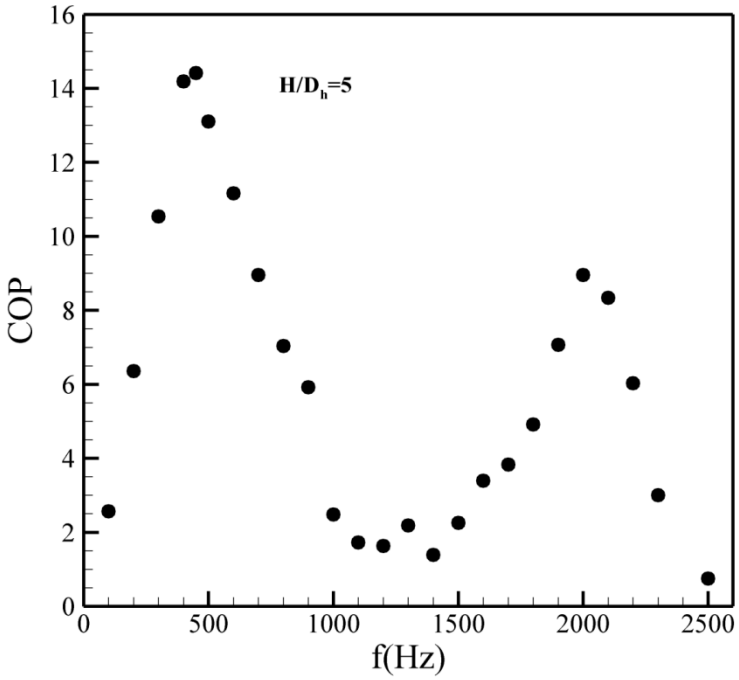

Figure 42.Variation of COP with frequency for a slot synthetic jet at H/Dh = 5

4.2. Heat transfer comparison between a slot and a circular jet

The mass ejected from the nozzle of a synthetic jet in a single period is given as:

$$\int_{m1}^{m2} dm = \int_{0}^{\zeta/2} \rho\, A\, u(t)\, dt \tag{11}$$

where A is the area of the nozzle exit, ρ is the density of the working fluid and $\zeta=1/f$ is period. If the synthetic jet is driven with a sinusoidal wave, the time dependent velocity profile is given as:

$$u(t)=u_{max}.\, sin(2.\pi.f.t) \tag{12}$$

The jet exit velocity at the nozzle exit is assumed to be constant. The ratio of the mass ejected by a synthetic jet in a single period to its impinging jet counterpart during the same time interval is:

$$\frac{m_{syn,j}}{m_{imp,j}} = \frac{\frac{cos(2.\pi.f.t))_{n\zeta+1/2.f}^{n\zeta}}{2.\pi.f}}{\frac{1}{f}} = \frac{1}{\pi} \tag{13}$$

Therefore, Re number for a synthetic jet can be written as:

$$Re_j = \frac{\rho u_{max} D_h}{\pi \mu} \quad (14)$$

The constant average velocity during the ejection phase from the nozzle can be defined as $u_0 = u_{max}/\pi$, and the distance moved by a fluid slug through the ejection phase (stroke length) is given as $L_0 = u_0/2f$.

Figure 43 shows the variation of Re number with a stroke length of L_0/D for both slot and circular jets. Flow physics of a circular synthetic jet and a slot jet are different. While circular synthetic jets create vortex rings, slot jets create vortex pairs. In addition to differences in flow physics of *ART4000* and *ART4000s*, they have different ranges of operating conditions in term of both Re number and stroke length.

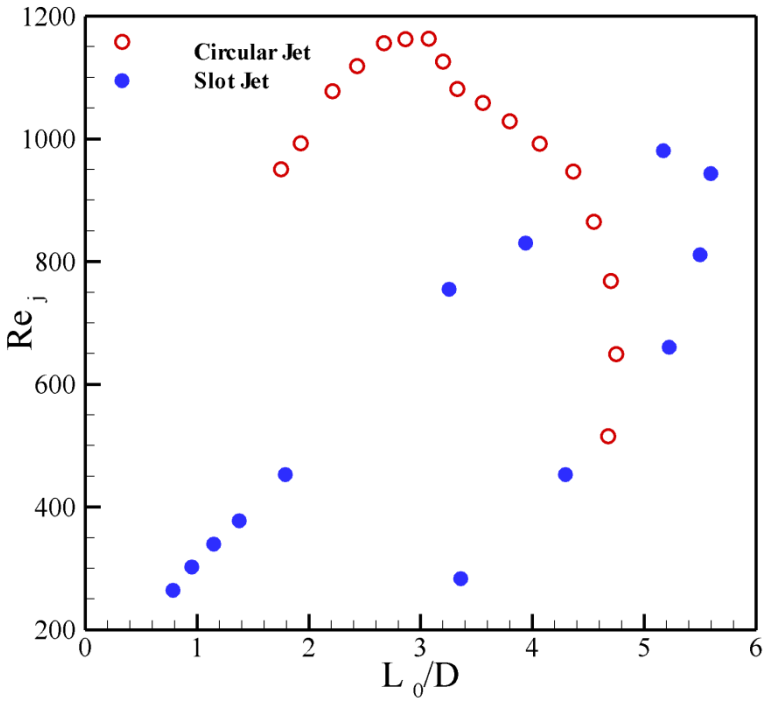

Figure 43.Variation of Re_j number with stroke length

4.2.1 Heat transfer correlation for a semi-confined circular synthetic jet

Figure 44 shows the variation of heat transfer enhancment factor ($EF = \overline{\mathrm{h}}/\bar{h}_{Natural}$) with driving frequency of the synthetic jet. *ART4000* was able to provide about seven times heat transfer more than natural convection for best operating condition at *H/D=4*. While the jet is located at closer locations to the target surface, heat transfer is found to be degraded. This is particularly due to the poor vortex growth and weak air replenishment leading to higher air temperatures. Heat transfer enhancement values are found to be 6.5 and 5.5 for the dimensionless distances of 3 and 2 respectively.

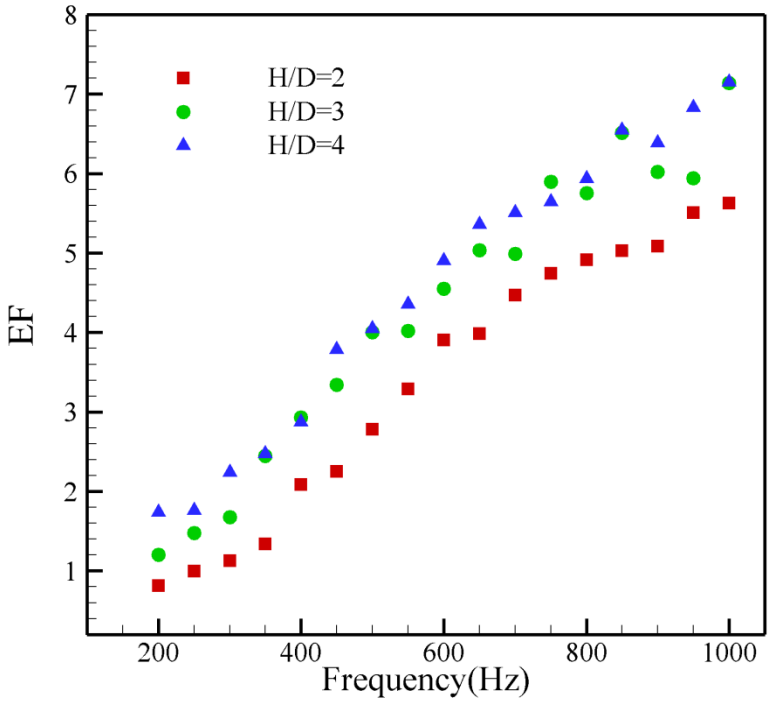

Figure 44.Heat transfer enhancement factor for ART4000

The lowest performance is observed at 200 Hz for *H/D=2* which is slightly less than natural convection. Having a poor heat transfer at jet locations close to the surface is due to recycling warm air during the suction period of jet operation. Figure 45 presents the effect of driving frequency on Nu number for ART4000 jet at different jet-to-heater spacings. Average Nu number ($Nu_{ave} = \overline{\mathrm{h}}D/k_{air}$) increases with an increase in distance and frequency. Maximum heat transfer is not experienced at the structural resonance frequency of the diaphragm (*f=700*

Hz) where the jet reaches to peak velocity and maximum deflection. Average Nu number linearly increases with the increase of jet to surface spacing. It is observed that average Nu number increases about 40% between *H/D=2* and *H/D=4* for *1000 Hz*. Vortex rings demand some spanwise spacing to grow. When the heater is close to the surface, the chance of growing is less,and thus the flow is affected by impinging a plate. Additionally, there may be a chance of re-using the warm air ($T > T_{amb}$) in the suction stage of the synthet jet when jet is close to the surface.

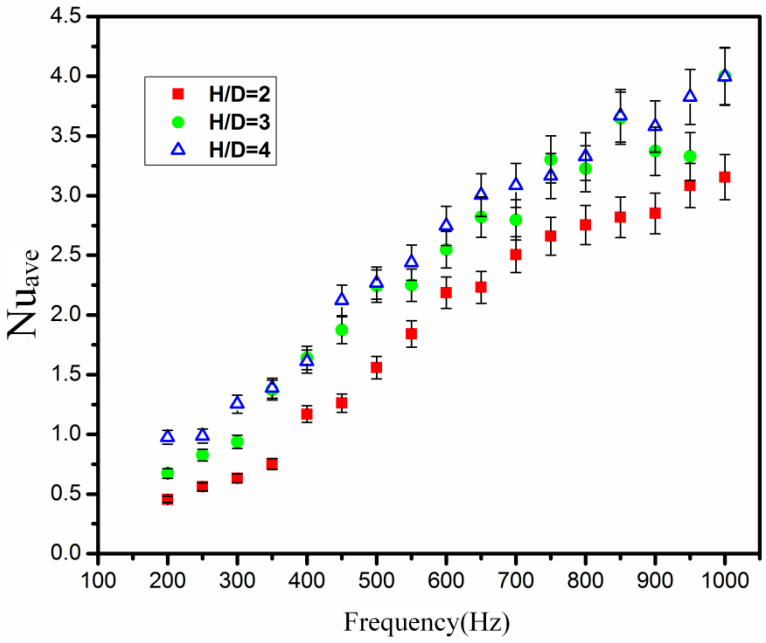

Figure 45.Effect of operating frequency on the average Nu number for a circular jet

Figure 46 shows average Nu numbers as a function of the stroke length and Re number. The stroke length is plotted as L_0/H, relative to the jet-to-surface spacing. These results are obtained for a jet-to-surface distance of *H/D = 2* and *H/D=4*. Nu number is normalized as $Nu_{ave}/Re^{0.5}$ where the power of Re number was gained with least-squares fitting of the data points to a single curve.

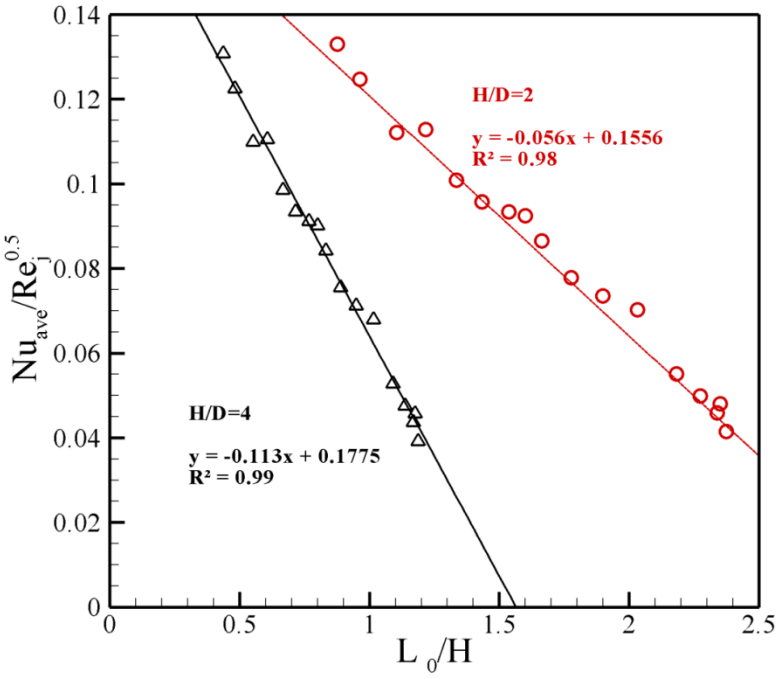

Figure 46.Variation of average Nu number as a function of stroke length L_0/H for circular impinging synthetic jet ($H/D=2$,$1D < L_0 < 4.75D$, $0.9H<L_0 < 2.5H$), $H/D=4$($1D < L_0 < 4.75D$, $L_0 < 1.3H$), $500 < Re_j < 1160$).

The solid lines in Figure 46 represents a least squares power law fit as:

$$\frac{Nu_{ave}}{Re_j^{0.5}} = -0.113\ {}^{L_0}/_{H} + 0.177 \qquad (R^2 = 0.99,\ \frac{H}{D} = 4) \tag{15}$$

$$\frac{Nu_{ave}}{Re_j^{0.5}} = -0.056\ {}^{L_0}/_{H} + 0.156 \qquad (R^2 = 0.98,\ \frac{H}{D} = 2) \tag{16}$$

where R^2 represents the coefficient of determination of the least square fit. The circular markers signify measurements on the constant temperature of the heated surface at $H/D=2$($1 < L_0/D < 4.75$, $0.9H< L_0 < 2.5H$, $500 < Re_j < 1160$). Additionally, the triangular markers represent measurements at H/D=4 ($1 < L_0/D < 4.75$, $L_0 < 1.3H$, $500 < Re_j < 1160$).

4.2.2 Heat transfer performance of a slot synthetic jet

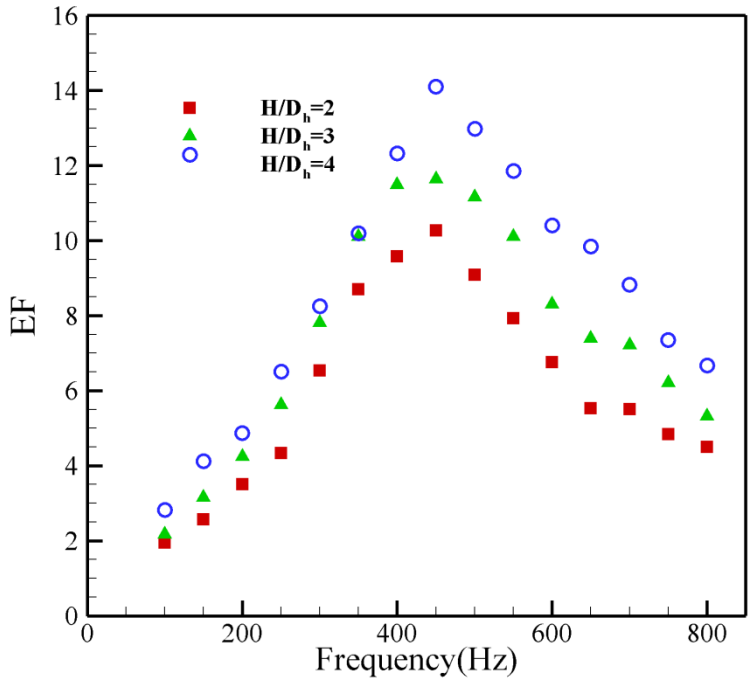

Figure 47:Heat transfer enhancement factor for the slot jet

Figure 47 depicts the effect of driving frequency on the heat transfer enhancement factor (EF) for different jet to heater spacings for the slot jet. Slot synthetic jet gives fourteen and ten times better performance than natural convection at $H/D_h=2$ and $H/D_h=4$ respectively. It is found that resonance frequency is about 450 Hz showing the maximum heat transfer. EF values are found to be 14, 12 and 10 respectively for three jet locations away from the heater surface.

Figure 48 demonstrates the variation of average Nu number over a range of frequencies for a slot synthetic jet. The slot synthetic jet creates vortex pairs and flow physics governed by thee slot jet is different from the circular jet. Unlike a circular jet, the maximum heat transfer occurs at 450 Hz where the jet shows the best performance similar to peak velocities given in Figure 17. Peak Nu number is found to be 7 for a jet air velocity of 26 m/s at a dimensionless distance of 4, and it degraded to a Nu number of 5 at the closest placement of 2.

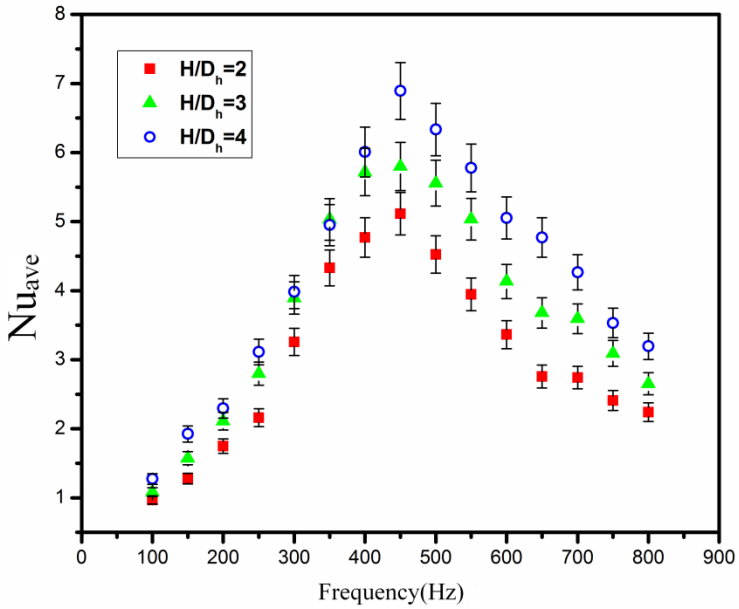

Figure 48.Variation of average Nu number variation with frequency for a slot jet

The slot jet lost around 40 percent of cooling performance by getting closer to the heater from $H/D_h=4$ to $H/D_h=2$ at 450 Hz. The L_0/D_h for 450 Hz is around 5 ($L_0= 2.5\ H$) which means the vortex pair reached to the surface before it completely grew. When the heater is placed close to the surface, the chance of jet growing is less; and the flow is affected by impinging plate.

4.3. Jet Power Consumption and Cooling Efficiency

Figure 49 demonstrates the power consumption of two jets with respect to driving frequency. For a slot jet, power consumption was increasing continuously with frequency. On the other hand, for a circular jet maximum power consumption occurs at the structural frequency of the synthetic jet.

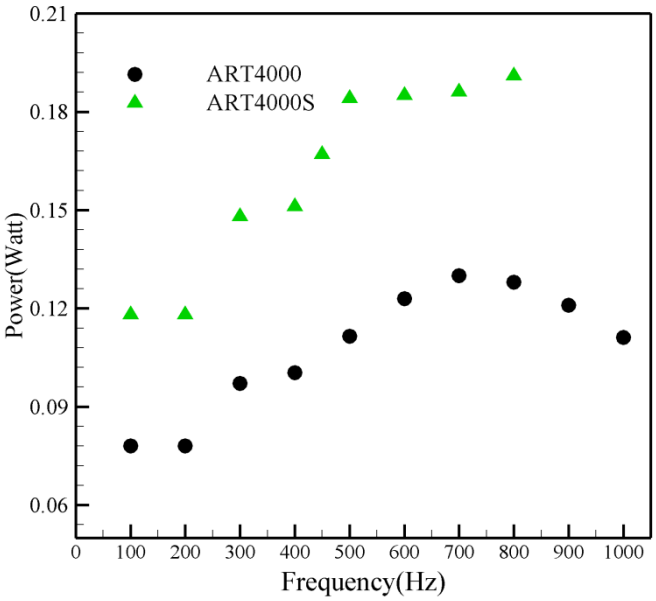

Figure 49.Variation of power consumption for ART4000 and ART4000s with frequency

Differences between flow physics and operating conditions of a slot and a semi-confined circular synthetic jet resulted in different cooling performances. While cooling performance is important, power consumption of the jets should also be considered for the ultimate system efficiency. Therefore, COP of both jet technologies have to be studied carefully. Figure 50 depicts the variation of COP with operating frequency for both *ART4000* and *ART4000s* synthetic jets located at *H/D=2* and *H/D=4*(for a slot jet $H/D_h=2$and 4) respectively.

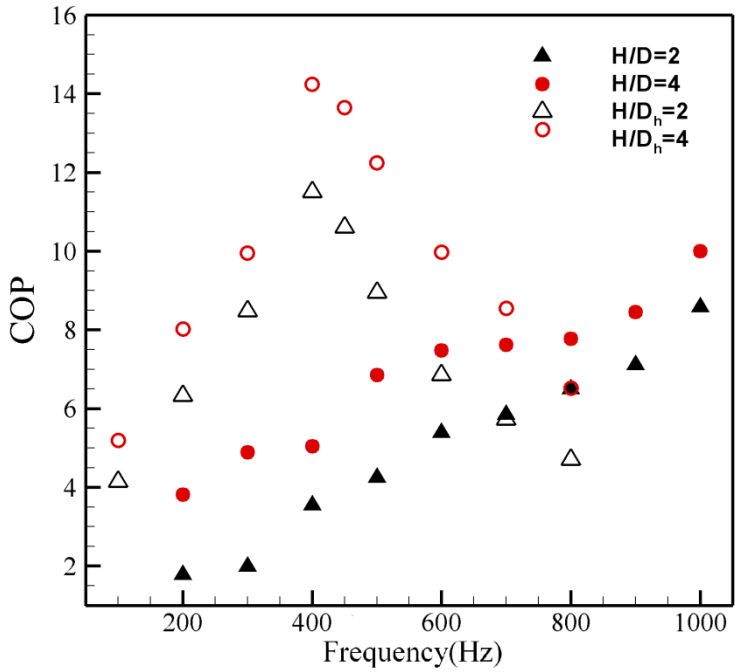

Figure 50.Variation of coefficient of performance with frequency for ART4000 (filled marker) and ART4000S at *H/D*=2and 4(*H/D*$_h$=2,4 for slot jet).

A slot synthetic jet has a better cooling performance compared to a circular jet based on the COP for a range of operating conditions. It is important to mention that the applied voltage to the ART4000 is 20 Volts peak to peak and for ART4000s is 35 V peak to peak. While consuming more power by a slot jet, it did experience a higher heat transfer and COP. As a consequence, the slot jet is a better candidate for electronics cooling applications.

CHAPTER V

COMPUTATIONAL STUDIES

In this chapter, we present the numerical simulation of the slot impinging synthetic jet. We used the moving boundary method in order to model the vibrating diaphragm. The details and results of numerical modeling are explained below.

5.1Modeling criteria and boundary conditions

The most crucial step in numerical simulation of the synthetic jet is the modelling of the vibrating diaphragm. Several approximations including using a velocity inlet boundary condition with an assumed profile at the location of the diaphragm/orifice exit [17,18,31] or using a moving diaphragm/piston boundary condition have been employed [53–55]. The schematic and boundary condition of a typical synthetic jet is shown in Figure51, Tables 5 and 6. The impingement target wall consists of a heated wall and unheated fixed walls.
The swept volume is maintained similar to a vibrating diaphragm. In the present simulations, we have been employing a wall boundary condition in which the diaphragm vibrates sinusoidally, such that the geometry of the wall is parabolic at any instant to simulate the vibrating diaphragm.

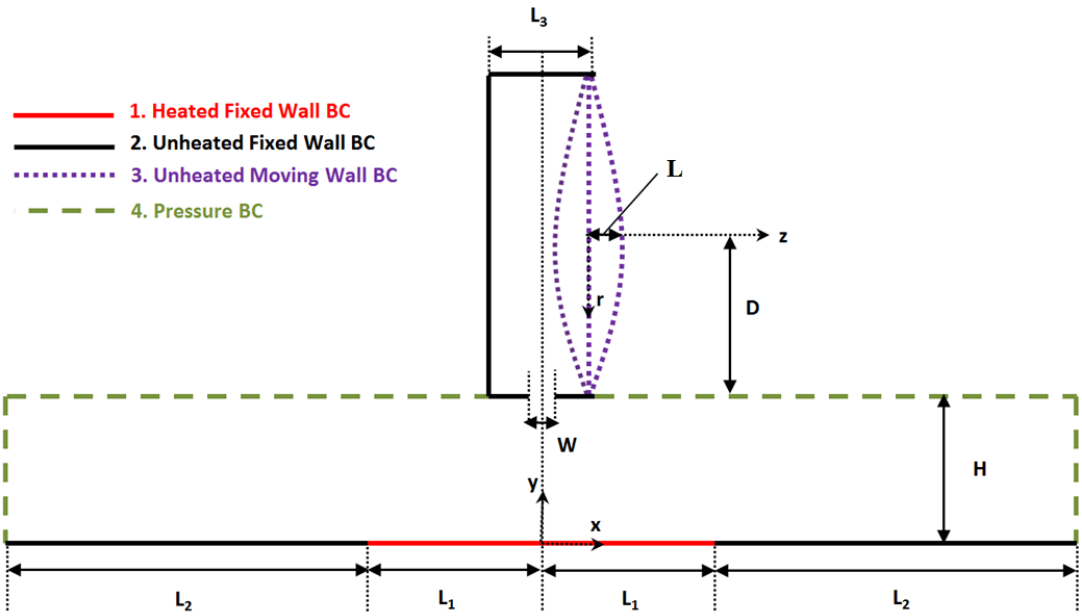

Figure 51. Impinging synthetic jet and boundary condition.

Table 5.Dimensions in modeling

Feature	Dimensions (mm)
W	1
H	8.89
L_1	12.7
L_2	3.3
L_3	1.3
A	0.325
D	19

Table 6.Boundary conditions

Boundary condition	Description	Equation
1	Wall BC	u=0, $T=T_w$
2	Wall BC	u=0, dT/dy=0
3	Moving Wall BC	x=Δ* sin(2*pi*f*t)[1-(r/D)^2], u=dx/dt
4	Pressure BC	P=0

The displacement of the membrane X(t) was assumed to be a parabola such as:

$$X = \Delta(1 - (r/d)\text{^}2)\ sin(2\pi ft) \quad (17)$$

in which Δ is the centerline amplitude and d is the diameter of the diaphragm. To simulate the displacement of the membrane, an actual mesh deformation in the vicinity of the membrane has been applied accordingly to equation (17), so that computational domain has been reconstructed at each time step.

In this study, the incompressible flow and temperature fields created by a synthetic jet emanated from a rectangular shape nozzle are investigated. For an impinging jet, minimum aspect ratio to obtain two-dimensionality is about 6:1 as given in [19]. Therefore at a high aspect ratio of 8:1, a rectangular (slot) synthetic jet can also be treated as two-dimensional (D_h = 1.778 W). Published literature has concluded that, without sacrificing fundamental qualities, the synthetic jet behavior could be adequately described by a 2D treatment of the flow induced by a vibrating membrane [53,55]. A dense structured hex computational grid is generated with appropriate refinements in the vicinity of the target plate and the nozzle. Mesh sensitivity of the model is also checked so that the computational results do not vary with further refinements on the grid. All the computations are performed with a commercially available general purpose CFD package[56]. For the spatial discretization, second-order

upwind schemes are used to determine the momentum and thermal fields. SIMPLE algorithm is implemented for pressure-velocity coupling and a *k-ω* turbulence model is used in the computations. For the temporal discretization, a second order implicit scheme is used for stability.

The time stepping is performed at a fixed interval of $6.17\ \mu s$ in order to have 360 time steps per cycle and fulfill the limits of CFL (Courant–Friedrichs–Lewy condition) condition[57]. Initially, the temperature at the nozzle-exit ($T(x,0)$) is equal to the ambient temperature of 25 °C, and the heated wall is kept at a fixed temperature of $T_w = 60\ °C$. Only the forced convection heat transfer is taken into consideration and radiation between the heated wall and its surroundings is neglected. The radiation heat transfer from the front surface of the heater by assuming emissivity equal to one is $(Q_r=\sigma.\epsilon.S\ (T_w^4-T_{amb}^4))$ 0.09 watts which is less than 3% present of the heat removal from the heater at forced convection conditions in CFD.

This section presents the validation results. As observed from Figure 52, the expulsion stroke agrees well with our experimental results; however, the velocity during the suction stroke is somewhat under predicted. Later we made a comparison of surface average Nusselt number between computational results and experiments (see table7).Results showed 15% deviation from the experiments.

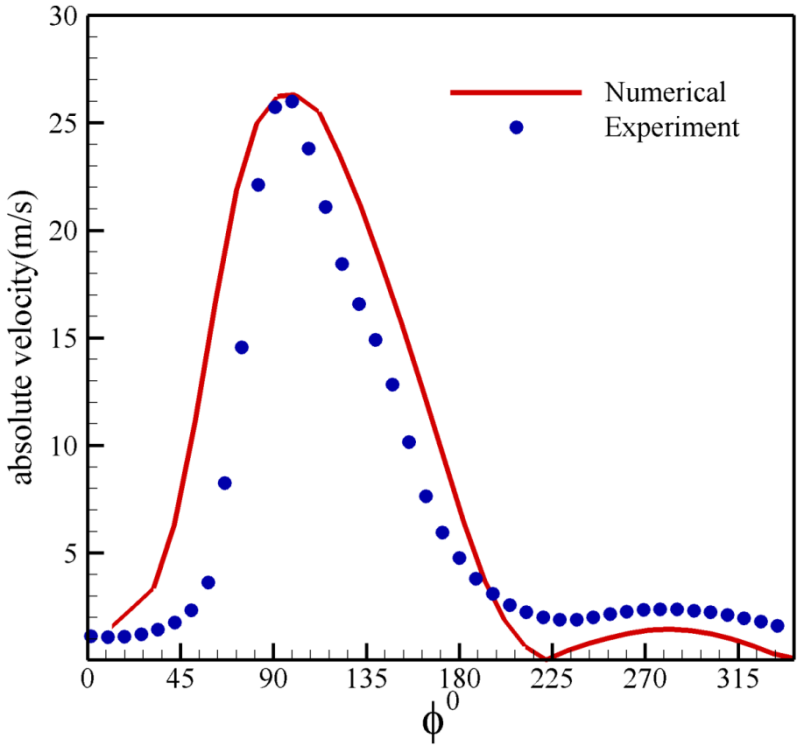

Figure 52.Comparison of CFD with the absolute instantaneous exit velocities measured at the center of the orifice of at *y/W*=1 in one cycle.

5.2 CFD results

Figure 53 demonstrates the non-dimensional streamwise velocity profiles near the target wall at different *x/W*. As can be seen, the wall jet produced by a synthetic jet differs considerably from its impinging jet counterpart. The maximum value of the non-dimensional streamwise velocity is a function of the phase angle and varies between 0.05 and 0.65. It is noteworthy that the highest of these maximum values (u_x / u_{max} = 0. 65) is obtained exactly in the *1/4*$_{th}$ of the inhale phase, i.e. φ = 225° at *x/W*=2 and the lowest of these (u_x / u_{max} = 0.05) is obtained exactly in the 1/4$_{th}$ of the ejection phase, φ = 45° at *x/W*=1. The large variation in the maximum streamwise velocity values starts reducing while the jet translating far away from the stagnation area. As shown in Figure 6, at *x/W* = 8, the variation of u_x /u_{max} is narrowed

down to $0.183 \leq u_x / u_{max} \leq 0.32$, but still dependent on the phase angle. The angles (times) at which the highest and smallest of the maximum velocity values in the ejection and inhale phases are seen also change with the streamwise distance (for example the maximum velocity occurs at $\varphi = 225°$ for $x/W = 2$ vs. $\varphi = 270°$ for $x/W = 4$).

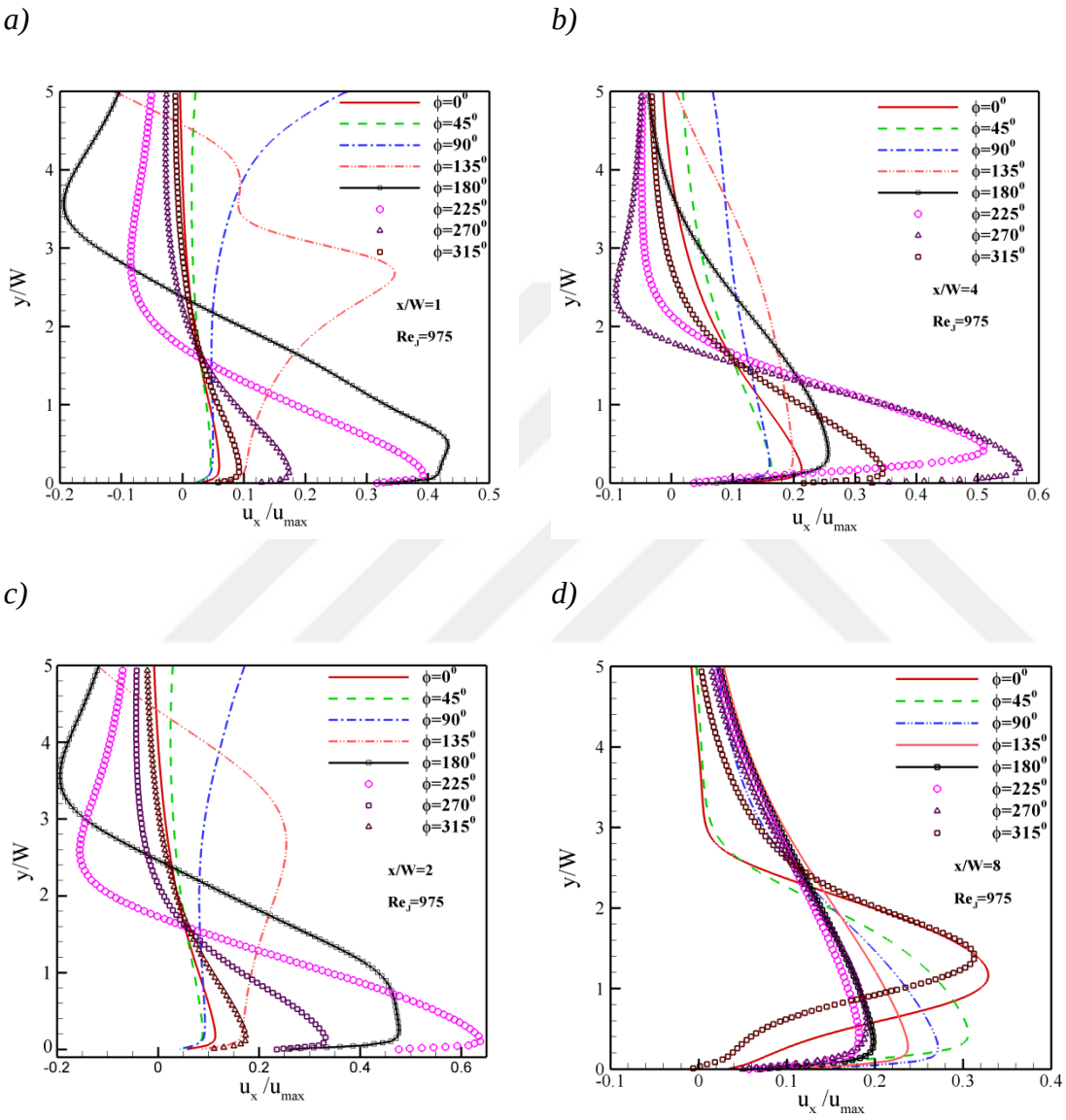

Figure 53.Distribution of non-dimensional axial velocity of a slot synthetic jet near the wall at various phase angles, a) x/W=1, b) x/W=2, c) x/W=4, d) x/W=8.

Figure 54 demonstrates the non-dimensional time average streamwise velocity profiles near the target wall at various x/W. It can be seen that after impingement, the mean velocity

profiles gradually exhibit the wall jet features as the vortex expanding along the streamwise direction. The maximum local velocity u_m, half-width $y_{1/2}$, and their variations can be obtained from Figure 54.

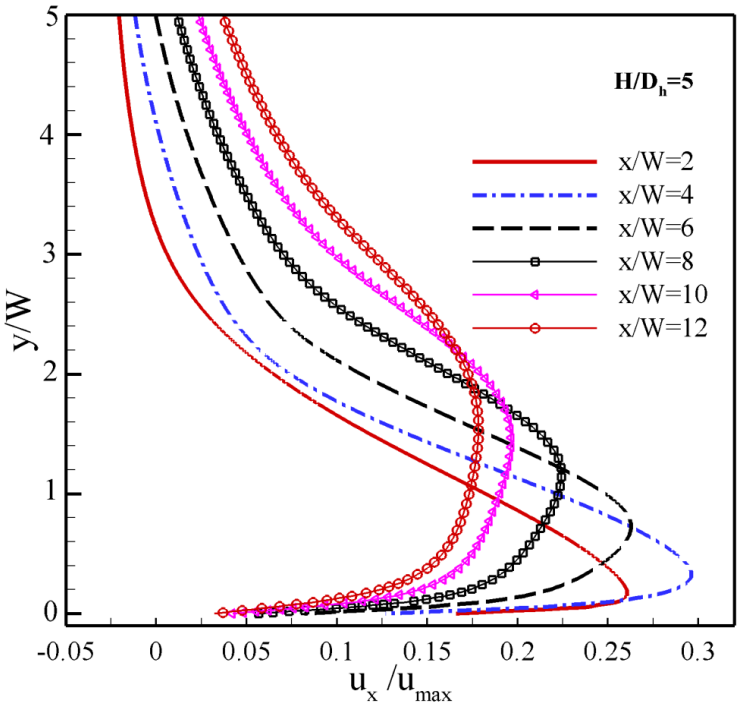

Figure 54.Distribution of time average non-dimensional axial velocity profile in different streamwise direction.

The distribution of the non-dimensional mean velocity is plotted in Fig. 55. Here, the mean velocity is normalized by the local maximum velocity while the streamwise location is normalized by the half-width of the wall jet. Fig. 55shows that all the velocity profiles have large differences with the theoretical laminar solution[49]. The Profile shows three regions; One is close to the stagnation point $1< x/W<4$, a developing region exists between $4< x/W<8$ and downstream from the jet exit $x/W>8$ a developed region is observed where the profiles collapse. The inner region of wall jet is totally different from the laminar solution, while the outer region shows almost similar behavior at $x/W>8$.At $x/W=2$ the wall profile more

resembles the turbulent one[50] .The velocity profile in developed region *x/W*>8 is neither laminar nor turbulent.

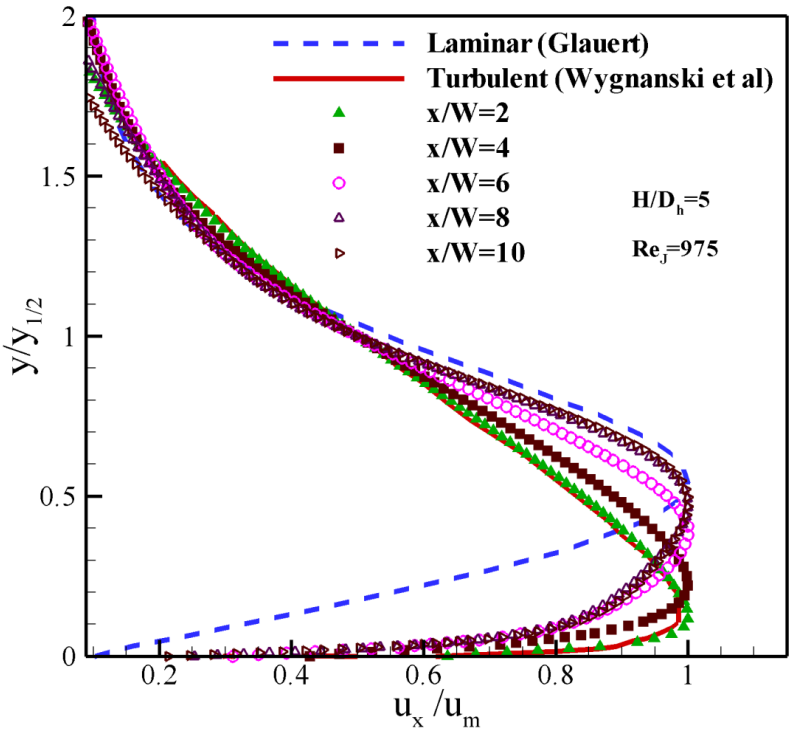

Figure 55. Normalized mean velocity profiles compare to developed turbulent and laminar profiles.

Figure 56 shows the non-dimensional turbulence kinetic energy profiles near the target wall at different *x/W*. As can be seen, in the outer region, the highest turbulence kinetic energy levels are obtained at *x/W* = 1 for $\varphi = 135°$. More of interest, the highest turbulence kinetic energy value in the inner region (i.e. approximately up to *y/W* = 0.4) is obtained at *x/W* = 1 at the beginning of the inhale phase. At higher streamwise distances from the stagnation area, the maximum values of turbulence kinetic energy decrease both in inner and outer region for all phase angles.

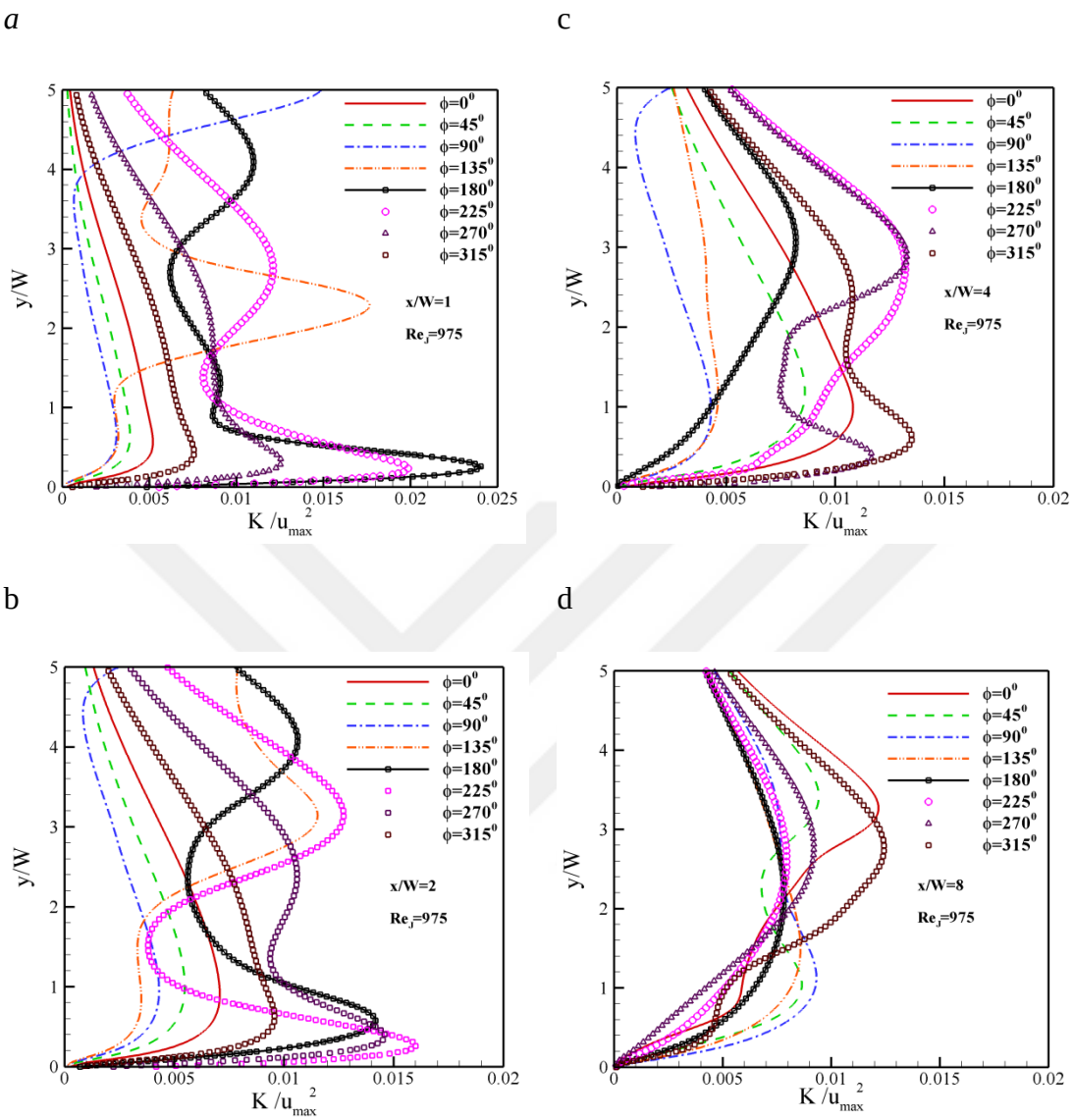

Figure 56.Non-dimensional turbulence kinetic energy profiles at various phase angles for Re_j = 975 and H/D_h = *5*. a) *x/W=1*, b) *x/W=2*, c) *x/W=4*, d) *x/W=8*.

Figure 57 demonstrates the non-dimensional pressure profiles of a synthetic jet on the target plate at various times (phase angles) for f = 450 *Hz*, Re_j = 975 and H/D_h = 5 (H/W = 8.89). As it can be seen, independent of the phase angle, the pressure coefficient value at the stagnation point is always positive whether the inhale and/or suction period takes place. The time

dependent synthetic jet experimental data demonstrates the jet centerline velocity is always towards the target plate, therefore the positive pressure coefficient values shown here are well-correlated with that. However, the sub-ambient pressure values (or negative pressure coefficient values) are observed at all of the phase angles except at the first half of ejection phase. An instantaneous maximum value of the pressure coefficient value around 0.4 is obtained at the jet centerline and at a phase angle of φ = 180° at which the vortices detached from the nozzle approach to the target plate (later shown in Figure 59). This non-monotonic behavior of turbulence kinetic energy and pressure along with strong pressure gradients translates into a non-monotonic behavior for the surface heat transfer coefficient as well as skin friction distribution.

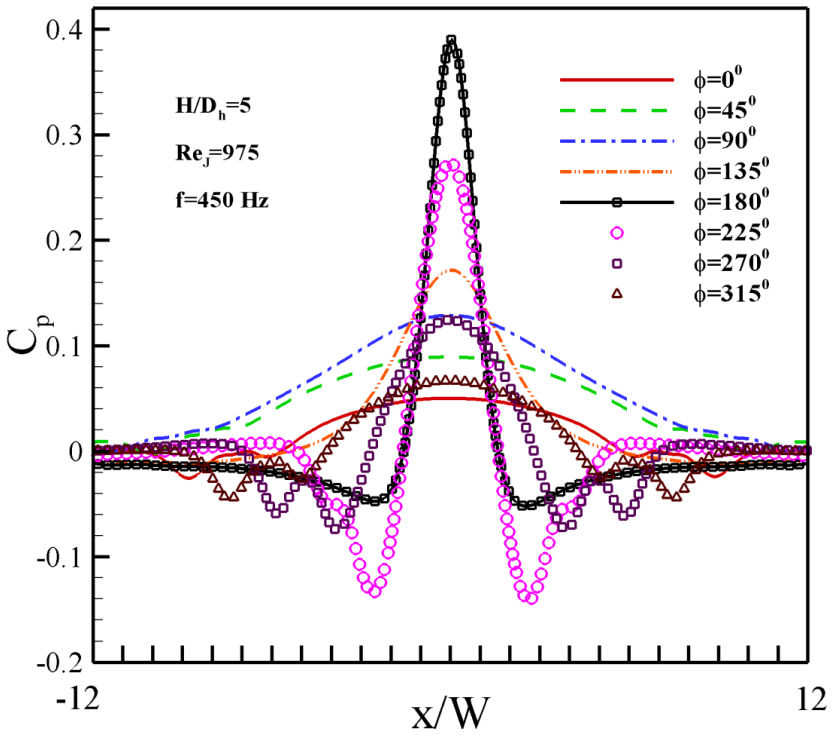

Figure 57.Non-dimensional pressure coefficient on the target plate at various phase angles (times).

Fig 58shows the skin friction distribution on the target surface at various phase angles. The maximum skin friction coefficient values are obtained within the first half of the inhale phase and at streamwise distances in the range of $1 \leq x/W \leq 3$.

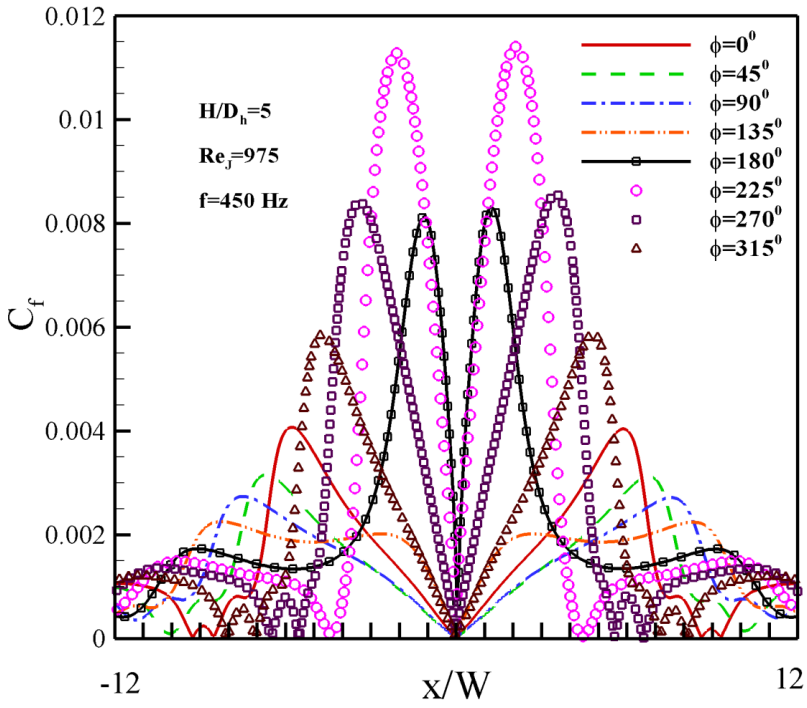

Figure 58. Friction coefficient distribution on the target plate at various phase angles (times)

Figure 59 shows the vorticity contours in a full period during the jet's normal operation. The vortex pair produced at the nozzle exit at the beginning of the ejection phase keeps attached to the nozzle for the most of this phase. While the vortex pair being attached at the ejection phase, it keeps growing in size and in strength with the entrainment from the surrounding fluid. Consequently, the vortex pair gets detached form the nozzle exit at the beginning of the suction phase. In time, the vortices grow in size however they are not as strong as they were in the ejection phase possibly due to turbulence dissipation.

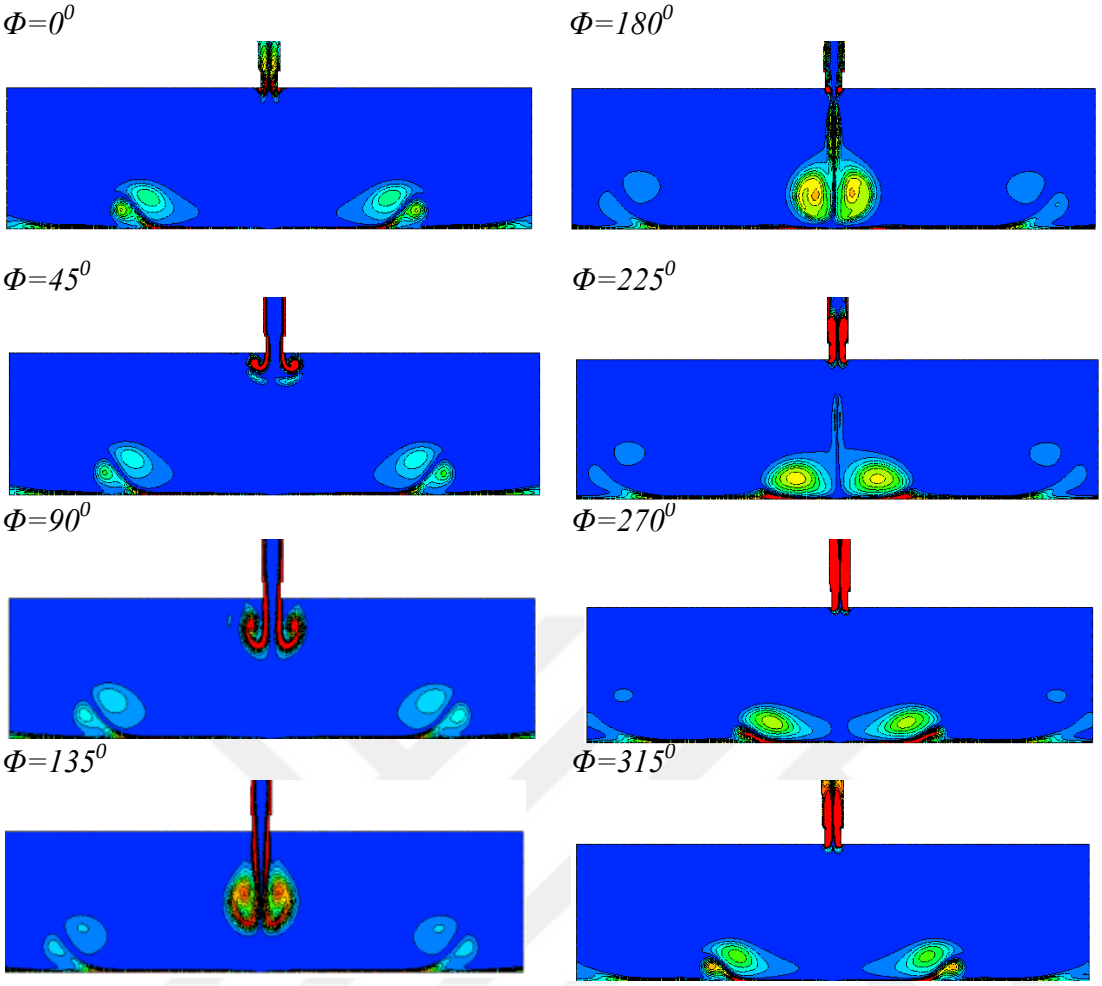

Figure 59. Vorticity contour plots during the injection and suction periods, f = 450 Hz, H/D_h = 5 (H/W = 8.89), Re_j = 975, and $-10W \leq x \leq +10W$.

Fig 60 shows the Nu number distribution on the target surface at various phase angles. Due to vortex wall interaction and its effects on wall boundary layer and consequently changing the wall profile we can see a wavy profile of Nu profile in this region. As can be seen, the wall distribution demonstrates two off-center peaks with the second being smaller in magnitude with the increasing distance from the stagnation point. These off center peaks become also smaller in magnitude with the increasing phase angle, where towards of the beginning of the cycle the first off center peak becomes more of a plateau. In addition, it is noteworthy that the overall maximum

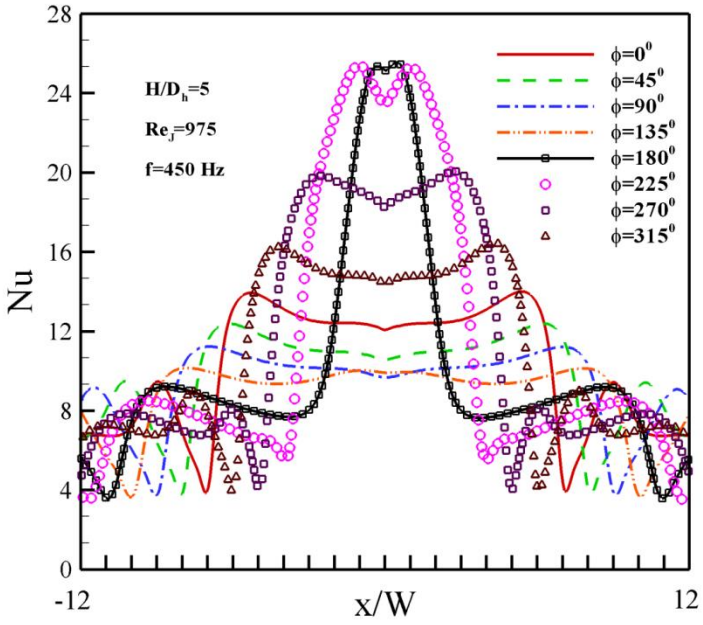

a)

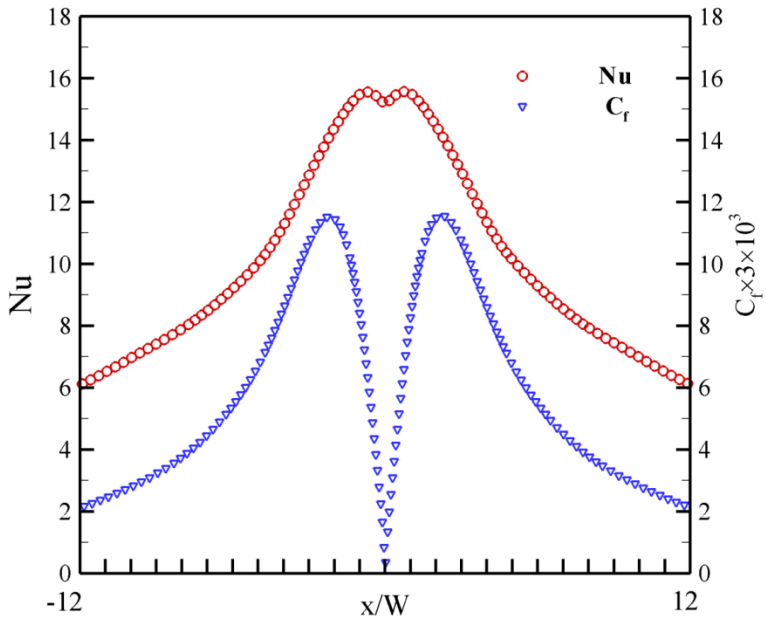

b)

Figure 60. a) Nu distribution on the target plate at various phase angles (times), Re_j = 975 and H/D_h = 5, b) Distribution of time average wall profiles.

heat transfer coefficient is obtained at the stagnation point within the first half of the inhale phase. However, when the time averaged values are plotted, the off-center peaks seen for any phase angle completely vanish.

Table7 show a comparison of average Nusselt number between synthetic jet and impinging jet at constant Re and different jet to surface spacing. The synthetic jet showed 30% better heat transfer performance at $H/D_h=5$.At $H/D_h=10$ synthetic jet shows a little advancement compared to impinging jet .At $H/D_h=20$ impinging jet has higher heat transfer than Synthetic jet. Thus synthetic jet has better performance only in the region which is dominated by coherent vortex structure.

Table 7. Comparison of average Nusselt number between synthetic jet and impinging jet

Re_j=975	H/D_h=5	H/D_h=10	H/D_h=20
CFD	Nu =9.5	-	-
Exp	Nu=8.2	Nu=8.5	Nu=7.8
Exp Imp [4]	Nu=6.2	Nu=8.4	Nu=9

CHAPTER VI

ULTRASONIC MICROFLUIDIC JETS

In this chapter, we have studied high frequency synthetic jets. We examined the velocity in two different shapes of the jet in order to investigate the device velocity measurements and pulsatile nature of the flow. The velocity measurements were performed with and without exhaust nozzle. Figure 61a shows the velocity measurements for the jet without exhaust nozzle. The measurement was taken at 1mm away from the Nozzle. Flow has a pulsating nature with the frequency match with the diaphragm excitation frequency which is f=25 kHz. Figure 61b shows the velocity measurements of the jet with Exhaust nozzle.

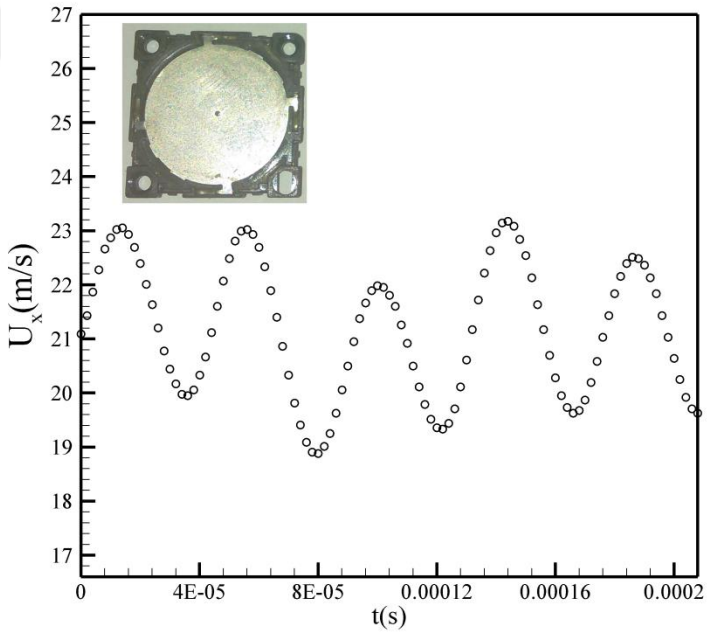

a)

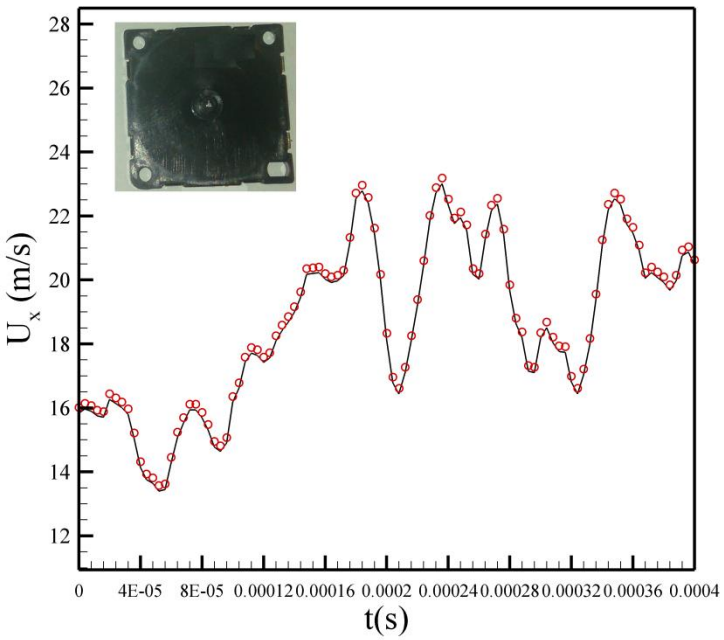

b)

Figure 61. Instantaneous velocity measurement a) Jet without exhaust nozzle. b) Jet with exhaust nozzle

Considering the fact that the commercial jet has an exhaust nozzle, the rest of the study considering deflection , heat transfer and PIV measurements was performed on the jet with exhaust nozzle.

Figure 62 shows the power spectrum of both cases. In case of the jet without exhaust nozzle there is strong peaks occurs at the jet forcing frequency which is f=25 kHz. There are some other pecks in the curves, but it seems these are not harmonics of the oscillation. In the case of jet with exhaust nozzle, it seems the peak is not strong at the forcing frequency and the noise level is higher than previous case revealing that the exhaust nozzle somehow decreases the pulsating nature of the flow.

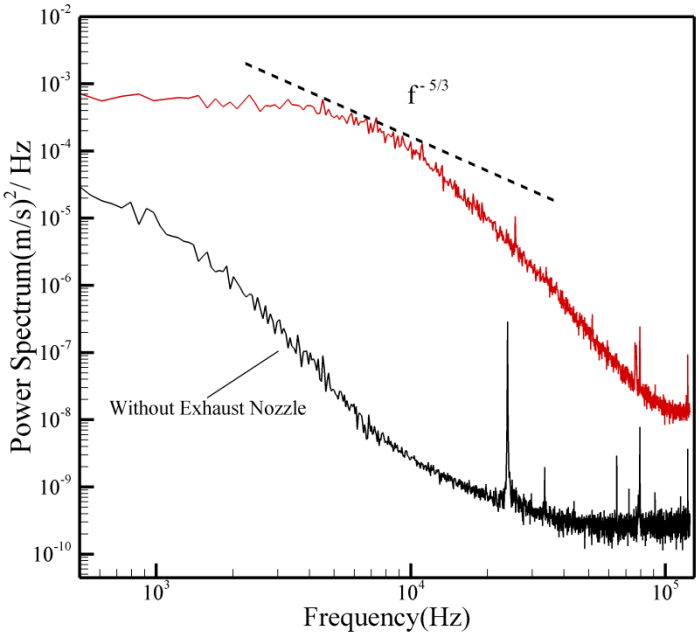

Figure 62.Power spectrum vs frequency for the jet with and without exhaust nozzle.

6.1.PIV flow visualization

In order to understand the flow field associated with micro-blower impingement cooling, the flow behavior was investigated using PIV measurements. In this section, we first present the time-averaged results for a free synthetic jet. Then, we present the time-averaged results for an impinging blower jet. For each case, a total of 500 image pairs were acquired, and the resulting flow fields were ensemble-averaged.

The PIV measurements examine a 2-D slice along the centerline of the jet. Figure 63 shows the schematic of the impinging jet, where *H* is the jet-to-surface spacing.

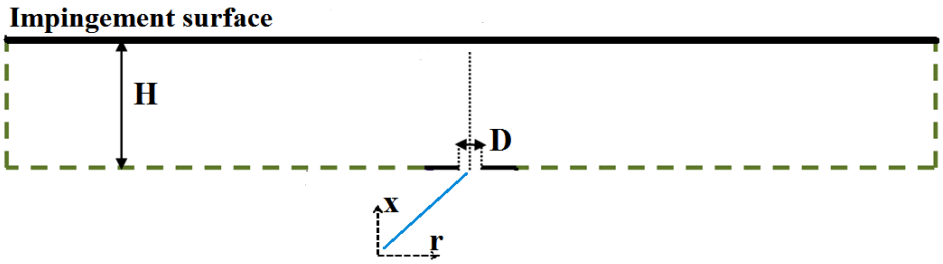

Figure 63. Geometry of a round impinging jet

Figure 64 shows the time-averaged velocity vectors and vorticity contours for an upward-directed, free jet. Here, the jet operates at a Re number of 1300 at 25 kHz. Vorticity is normalized by the jet diameter. The jet spreads slightly as it travels upward, and it has a symmetric behavior along its centerline. Jet speeds are near zero with the first 5 diameters downstream for two reasons. First, the inflow and outflow speeds balance during the oscillating jet motion. Second, there were some artifacts due to reflection of laser light near the exit, which impacts the PIV cross-correlation accuracy.

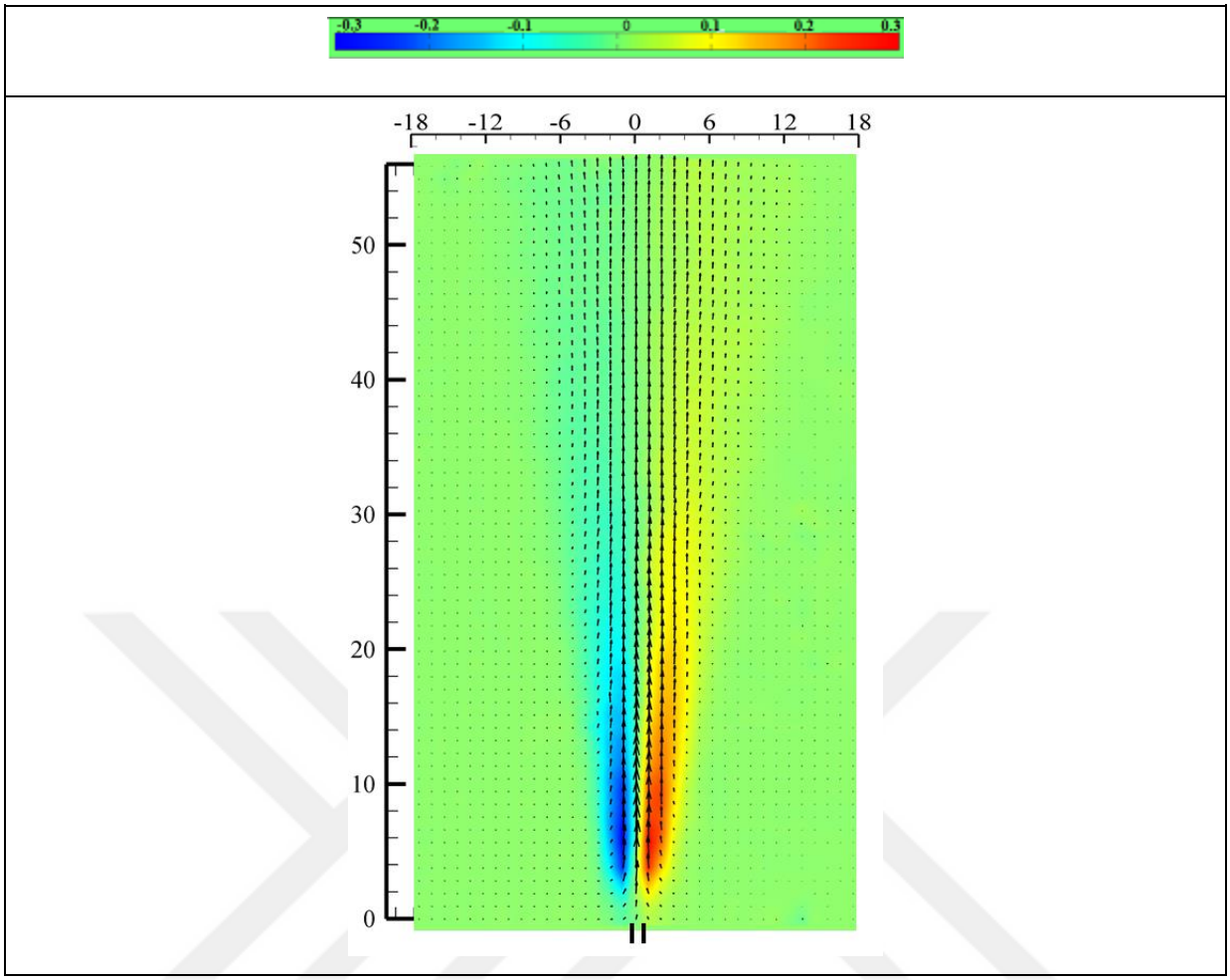

Figure 64. Velocity vectors and dimensionless vorticity ($\omega W/U_0$) for a free, ultrasonic micro-blower jet at Re = 1300.

Figure 65a shows the streamwise variation of normalized centerline velocity in the free jet at axial position $x/D \geq 5$. The velocity shows continuous decay as jet moves upward. The jet spreads in the transverse direction, which results in a decrease of the centerline velocity. Ultimately, the decrease in the far field deviates slightly from $1/x$, as might be expected from a steady, axisymmetric jet. Figure 65b shows the transverse distribution of streamwise velocity at different locations downstream from the nozzle. By comparing between different axial locations, we can see how the jet spreads away from the nozzle. Between x/D = 5 and

50, the jet half-width increases by a factor of approximately 6, and it becomes more bell-shaped.

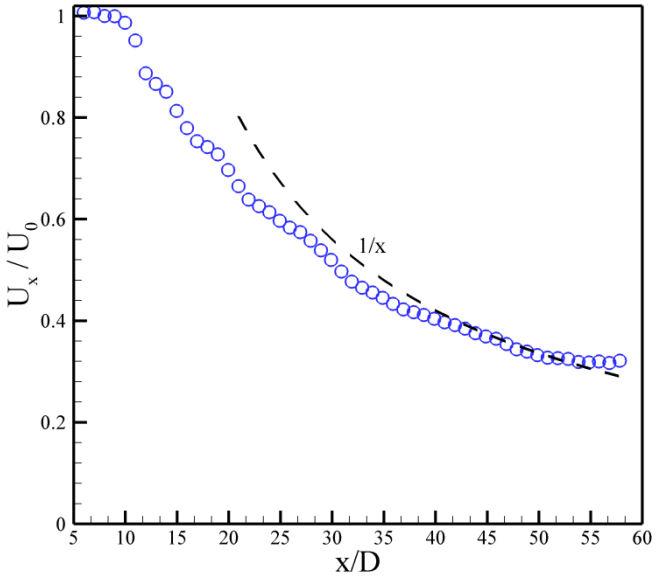

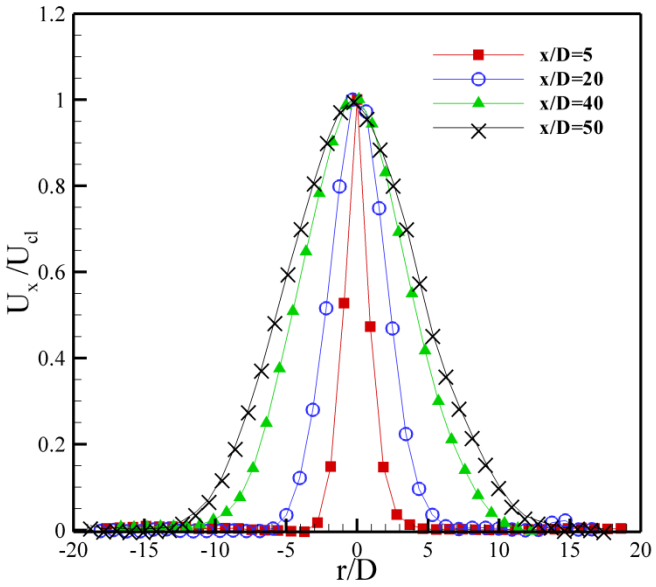

Figure 65. a)Streamwise variation of normalized centerline velocity in the free micro-blower jet and b). Transverse distributions of streamwise velocity in the free jet

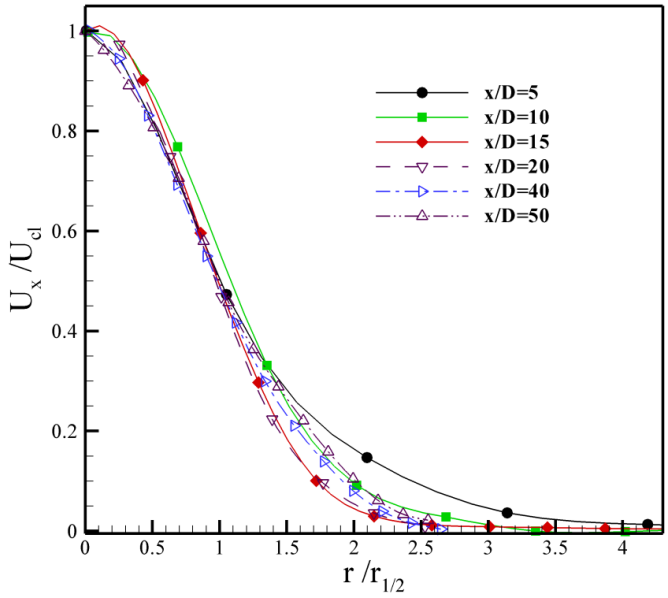

a)

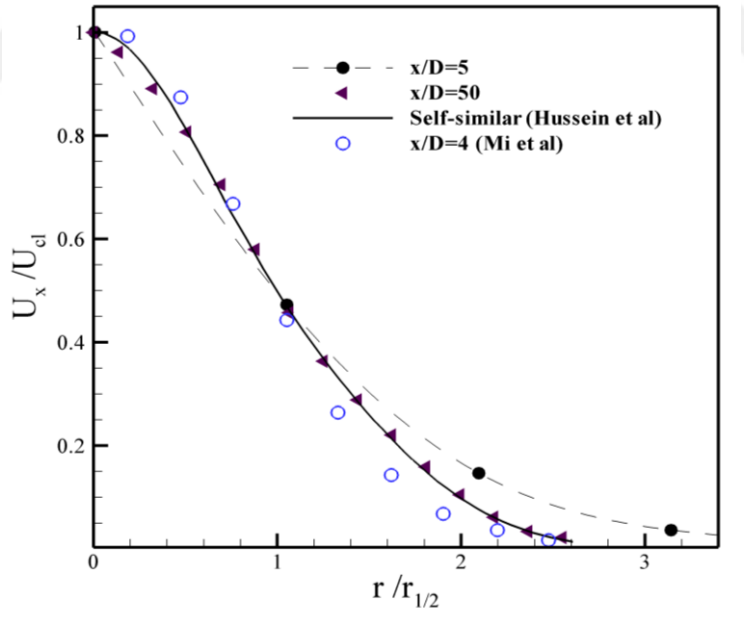

b)

Figure 66. Time-averaged, nondimensional axial velocity versus normalized radial position.

Figure 66 shows the time-averaged axial velocity profile, varying with radial position. The jet axial velocity is normalized by the local centerline velocity, and the radial position is normalized by the half-width, $r_{1/2}$, of the profile. Here, the half-width is defined as the position where the axial velocity is half of the centerline speed. In the downstream region, $x/D > 30$, a high-Reynolds number turbulent round jet should be self-similar, with a Gaussian profile for Re ~ 10^4 and above [58,59]. The micro-blower velocity profile shows excellent agreement with the self-similar turbulent round jet profile. Interestingly, the micro-blower operates at a much lower Re of 1300, yet the velocity profile is almost self-similar. This suggests that one can assume the far field ($x/D>40$) of the jet behaves similar to a turbulent round jet. But the near field of the micro blower profile differs largely compered to near field of turbulent free jet[60]. Hence, a continuous jet CFD model [61]is likely a significant over-simplification with the ultrasonic micro-blower.

Figure 67 shows the time-averaged vorticity contours for an impinging jet with a jet-to-wall spacing ratio of $H/D = 40$. Much like the free micro-blower jet, shown earlier in Figure 64, the flow is symmetric, growing in width as it travels downstream. Unlike the free jet, there are two additional regions of vorticity next to the wall. The peak vorticity magnitudes of this near wall region are less than the levels in the jet near the orifice.

Figure 68 shows the streamwise variation of the normalized, time-averaged centerline velocity for the impinging jet at $H/D = 40$.The centerline velocity shows almost similar behavior with free jet till $x/D = 30$, but after that the flow is affected by the impingement wall. The velocity experiences a sharp decrease for $x/D > 30$, and it reaches zero at the stagnation point.

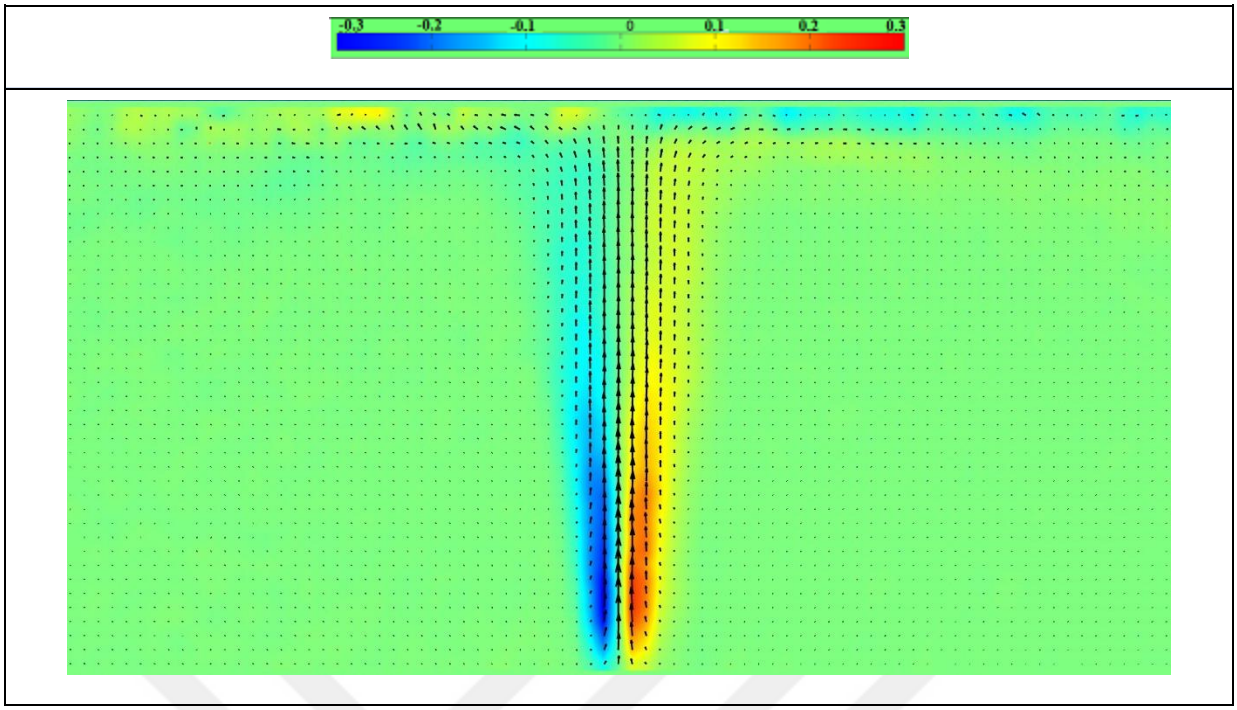

Figure 67.Time-averaged velocity vectors and vorticity contours, $\omega D/U_0$ for an impinging slot synthetic jet at Re = 1300 at H/D = 40.

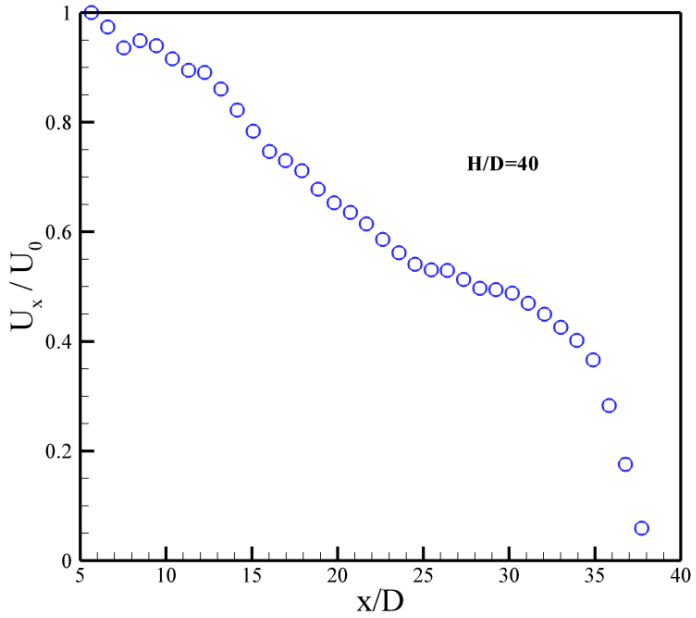

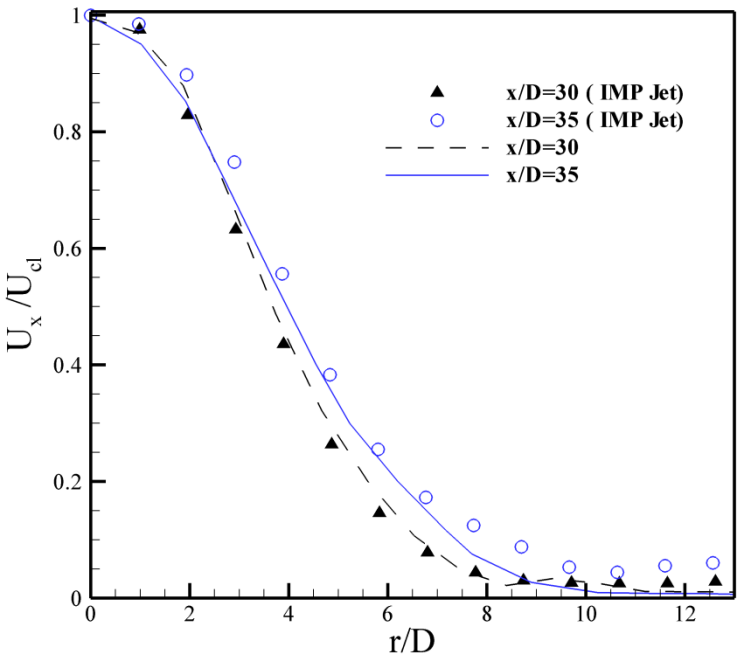

Figure 68. a)Streamwise variation of normalized, time-averaged centerline velocity b) Time-averaged, nondimensional axial velocity versus normalized radial position for the impinging jet at $H/D = 40$ and free jet

6.2. Heat transfer

Figure 69 shows the experimental results for the average Nusselt number at different jet-to-surface spacings at $f = 25$ kHz. The average Nusselt number increases sharply up to $H/D = 10$, and then it shows a gradual rise till $H/D = 15$. There is a fairly flat maximum region for $15 \leq H/D \leq 30$, followed by a gradual decay for $H/D > 30$. The heat transfer increases more than threefold by moving the jet from $H/D = 2$ to $H/D = 10$. This reveals that the jet performance is highly sensitive to the jet to surface spacing, and it decreases significantly for small jet to surface spacings. This sets a practical limit on the design and placement flexibility in applications, especially for compact systems.

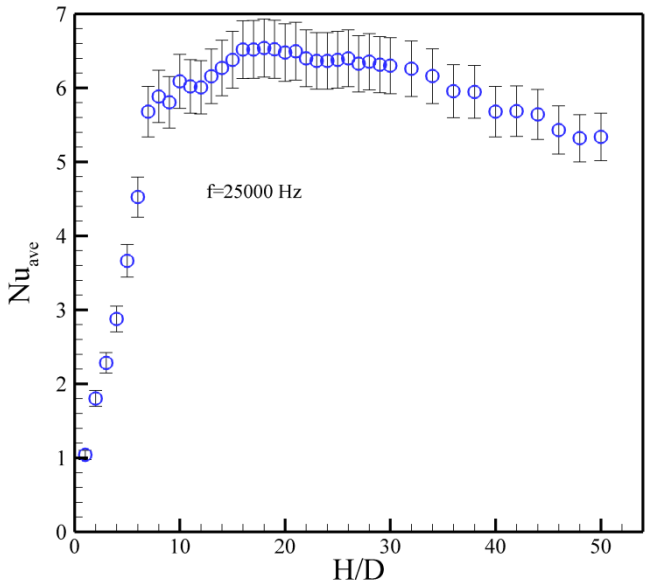

Figure 69. Variation of average Nu number with different jet-to-surface spacings at f = 25 kHz and Re = 1300.

An impinging synthetic jet typically has the maximum heat transfer performance at jet-to-surface spacings from $5 \leq H/D \leq 10$ [11,12]. However, for continuous jets [44,62]there is a monotonic decay of heat transfer with increasing jet-to-surface spacing at this Reynolds number. Much like the synthetic jet, the micro-blower has different heat transfer behavior within its near field of operation, although the peak response is further from the jet orifice. These differences suggest that the mechanism of jet development and response is significantly altered in the near field. Hence, a continuous jet CFD model [37,61]is likely a significant over-simplification with the ultrasonic micro-blower.

Figure 70 shows the variation of average Nusselt number versus frequency at H/D = 10. The heat transfer peaks at f = 25 kHz, which coincides with the peak observed in the deflection measurements of the actuator in Figure 7. This further suggests that the jet has its maximum flow rate here. Off of this peak frequency, the heat transfer decreases by less than 10% between 24.5 kHz and 25.5 kHz. However, the performance decreases rapidly below 24 kHz

and above 26 kHz. Thus, while there is some flexibility with the operating condition near the peak, the blower effectiveness is strongly dependent on frequency.

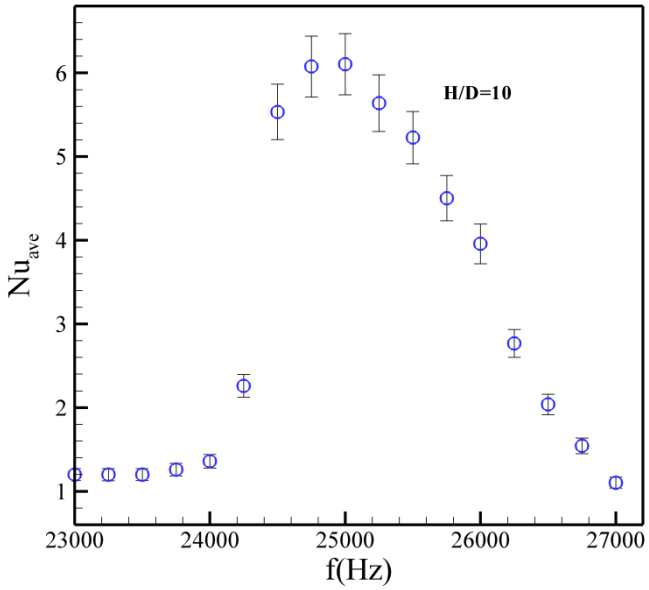

Figure 70. Variation of average Nu number with frequency for an impinging round jet at *H/D* = 10

Finally, whenever considering the performance of a new thermal management method, the required energy consumption must also be examined. Ideally, new techniques should require minimal input energy while producing significant heat transfer. This leads to a large coefficient of performance (*COP*).

Figure 71 shows the variation of COP at different frequencies for *H/D* = 10. Here, the highest COP is 3 at *f* = 26 kHz, suggesting that the jet has best COP at a frequency higher than its best heat transfer operating condition at *f* = 25 kHz. Thus, even though the heat transfer is higher at *f* = 25 kHz, the additional power consumption at this operating condition makes it less appealing. The COP at 25 kHz is around 2, which is much less than the values seen with slot

synthetic jet, which have COP ~ 14 [2]. Thus, while this micro-blower can greatly reduce noise, it has a significant performance penalty.

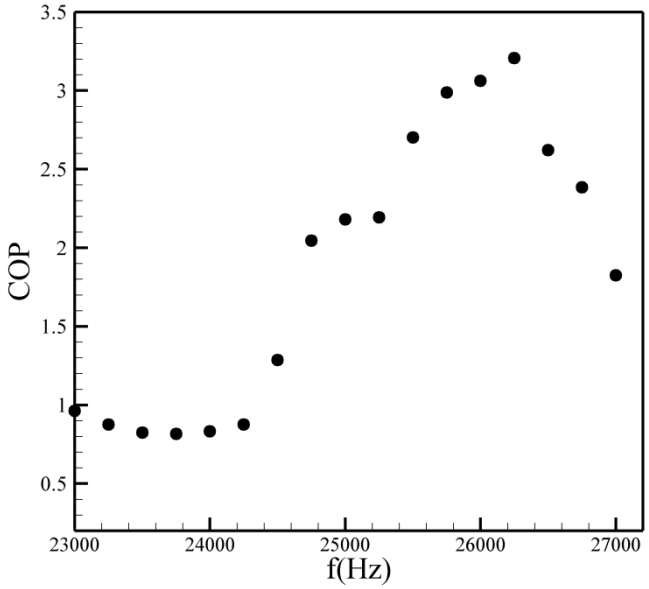

Figure 71. Variation of COP with frequency for a micro-blower jet at *H/D* = 10

CHAPTER VII

CONCLUSIONS AND FUTURE RESEARCH

An experimental and computational study has been completed as a part of current research. While a number of open questions are addressed there is certainly more work for future research. This chapter will outline the basic conclusions drawn from this research first and then provide a number research points for future research.

7.1Slot synthetic jets

We performed a series of experiments and CFD analysis to examine the performance of our novel designed slot synthetic jet. Along with measurements of deflection and thermal performance, we used time-averaged and phase-locked PIV to study the flow physics and their effects on heat transfer. We focused on slot synthetic jet behavior at several frequencies, both on and off resonant conditions, which may help in selecting device conditions with lower acoustic noise. Specifically, the findings in this study can be summarized as:

- The degradation of heat transfer for small jet-to-surface spacings, like $H/D_h = 2$, was due to the reduced growth of the vortices. In addition, there was re-entrainment of warm air next to the impinging plate by the vortex back into the jet flow, and some warm fluid was sucked back into the orifice.
- The heat transfer is maximum for jet-to-surface spacings from $5 \leq H/D_h \leq 10$, which is associated with flow dominated by coherent vortices that grow to full strength before detachment or impact with the wall.
- Results showed that near wall velocity profiles have large differences from the theoretical laminar solution in the inner region of the profile, further demonstrating how this synthetic jet differs from conventional steady impingement.

- At the diaphragm resonant condition and below, the flow structure was similar at all phases, with a single vortex present between the orifice and the wall. This response suggests that there is a critical jet-to-surface spacing for this behavior, $H_{crit} = U_o/2f$, which should relate to the optimal thermal condition. By tuning the actuator frequency to the wall spacing, the vortices can reach the wall in phase at the end of the outstroke. When well-tuned, the thermal response is governed primarily by the Reynolds number.
- Above the diaphragm resonant condition, there are two vortices present between the orifice and the wall, as $H > H_{crit}$. These eddies remain closer to the centerline, and they maintain their peak vorticity for a longer duration than at lower frequencies. As a result, this slightly super-resonant case has nearly identical thermal performance to the sub-resonant case, even though its peak Reynolds number is only about half as large. Hence, it should be possible to use slightly off-resonant actuation conditions to produce similar thermal response, which should lead to lower acoustic noise.
- There is superior cooling performance at high Stokes number with the same Re_{U0} number. However, even though the heat transfer is higher at f = 2000 Hz, there is more power consumption at this operating condition, resulting in a lower COP compared to the first structural resonance at f = 450 Hz.

7.2Comparison between a slot and a circular synthetic jet

An experimental and theoretical study has been performed to investigate the cooling performance of two different synthetic jets made up of piezoelectric actuators cooling a vertical heater for a range of jet to surface spacing. Based on the experimental and analytical results, the following conclusions can be drawn for the present study:

- The maximum cooling performance of a circular synthetic jet was not observed at the structural frequency of the jet where the maximum velocity occurs. It occurs at frequencies greater than the structural frequency.
- A correlation is proposed to predict heat transfer from a circular synthetic jet accounting the effects of Re number ($500 \leq Re_j \leq 1150$), jet-to-surface spacing ($H/D=2$ *and* $H/D=4$) and the stroke length ($1.75 \leq L_0/D \leq 4.75$ *and* $L_0/H < 2.5$).
- The correlation showed a linear behavior between $\frac{Nu_{ave}}{Re_j^{0.5}}$ and L_0/H for a specific condition for semi-confined impinging synthetic jet.
- A degradation of heat transfer when jets are close to the surface was observed (40% degradation between $H/D=2$ and $H/D=4$). Vortex rings/pairs need more spanwise spacing to grow.
- When the heater is close to the surface the flow is affected by impinging plate. Additionally, there may be a chance of recycling warm air in suction stage of synthetic jet located close to the surface.
- Based on COP comparison, slot synthetic jet has a better cooling performance compared to a semi-confined circular jet due to the difference in the flow physics of the two jets, so slot synthetic jet is a better candidate for electronics cooling applications.

7.3Ultrasonic microfluidic jets

We performed a series of experiments to examine the performance of an impinging ultrasonic micro-blower jet. Along with measurements of deflection and thermal performance, we used time-averaged PIV to study the flow physics and their effects on heat transfer. Specifically, the findings in this study can be summarized as:

- The preferred operating frequency of the piezoelectric actuator occurs at an ultrasonic frequency of 25 kHz, meaning that this device can function with low noise.
- The secondary exhaust nozzle reduces the sinusoidal, pulsating nature of the flow, producing a broad-scale frequency response with similar average speed
- The micro-blower axial velocity profile shows similar behavior to high Reynolds number turbulent free jets in the far field, including a self-similar profile. But in the near field it has significant deviation with turbulent free jet.
- The average Nusselt number increases sharply up to $H/D = 10$, and then it shows a gradual increase till $H/D=15$. There is a fairly flat maximum region for $15 \leq H/D \leq 30$, followed by a gradual decay for $H/D > 30$. The heat transfer increases more than three times by moving the jet from $H/D = 2$ to $H/D = 10$. This reveals that the jet performance is highly sensitive to the jet-to-surface spacing.
- The jet cooling performance is sensitive to the frequency, though there is a 1 kHz wide band of similar thermal response about the peak.
- The coefficient of performance at the best operating heat transfer condition is about 2, which is less than the value of 14 seen for a slot synthetic jet [2]. Thus, while this micro-blower can greatly reduce noise, it has a significant performance penalty.

7.4 Future research

A brief list of suggestions for future work can be given as the following:

1. Coupling synthetic jets with heat sinks is an interesting problem. Since the flow is vortex dominated flow and has major differences compared to tradition jets and fans there is a need for:

- Understanding vortex interaction with the heat sink and developing this concept for three different jets that we mentioned in this study.
- Design and optimization of novel heat sink based on the new concept.

2. Since the PIV is not able to resolve near wall velocity measurements. There is need for Direct Numerical Simulation (DNS) to provide the complete understanding of vortex wall interaction and its effect on heat transfer augmentation.

3. There is need for DNS to capture the details of unsteady behavior of ultrasonic micro blower.

4. Try to embed the synthetic jet in devices cooled by dielectric liquids.

5. There might be another application of synthetic jet in coating the surfaces which needs to be test.

APPENDIX A

Synthetic Jet Formation Criteria

Most of this appendix is extracted from the work done by Holman et al[5] to give background information. Jet formation is defined as the appearance of a time-averaged outward velocity along the jet axis and corresponds to the generation and subsequent convection or escape of a vortex ring. The governing parameters for a synthetic jet based on a simple "slug-velocity-profile" model include a dimensionless stroke length, L_0/D and a Reynolds number $Re_{U0} = U_0 D/\nu$ based on the velocity scale:

$$U_0 = fL_0 = f\int_0^{T/2} U_0\,(t)dt \tag{1}$$

where D is the diameter of the orifice (or the width of the slot), ν is the kinematic viscosity of the fluid, $u_0(t)$ is the centerline velocity at the exit, $T = 1/f$ is the period, f is the frequency of oscillation, and L_0 is the distance that a slug of fluid travels away from the orifice during the ejection portion of the cycle or period. Smith and Swift[64] argued that because the spatial velocity profile can deviate significantly from the assumed slug shape the centerline velocity profile $u_0(t)$ is more generally defined as the spatial-averaged velocity ,at the exit.

Alternatively, a jet Reynolds number can be defined in terms of an average jet velocity during the expulsion stroke:

$$Re_{\bar{u}} = \bar{U}\,D/\upsilon \tag{2}$$

where $\bar{U}$ is the time- and spatial-averaged exit velocity

$$\bar{U} = \frac{2}{T}\,\frac{1}{A}\iint_0^{T/2} u(t,y)dtdA \tag{3}$$

Here, A is the orifice exit area, and y is the cross-stream coordinates (See Fig. 1). Equations (1) and (3) reveal that the two velocity scales are related by$\overline{U} = 2U_0$.

Furthermore, note that $L_0/D=U_0/(f\,D)$is closely related to the inverse of Strouhal number via

$$\frac{1}{sr} = \frac{\left({}^{L_0}/_{D}\right)}{\pi} = {}^{\overline{U}}/_{\omega D} = \left(\frac{\overline{U}}{v}D\right)\Big/\left(\frac{D^2\omega}{v}\right) = Re/S^2 \tag{4}$$

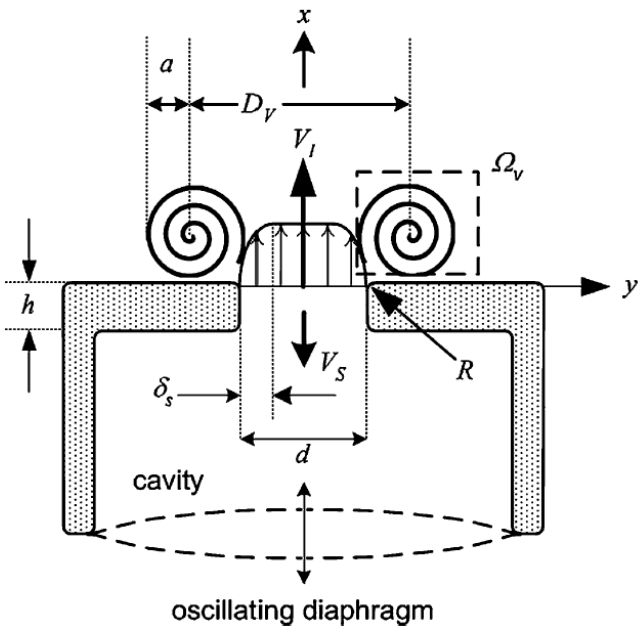

Figure.A1. Schematic of a synthetic jet

Where S is the Stokes number given by

$$S = \sqrt{\frac{\omega D^2}{v}} \tag{5}$$

and $\omega=2\pi f$ is the radian frequency of oscillation. The ability of a ZNMF actuator to impart momentum to its surroundings is highly dependent on these nondimensional numbers and, in addition, on the slot/orifice geometry.

Vortex-Based Jet Formation Criterion

Smith and Swift[64] and Rampunggoon [65] independently proposed a jet formation criterion for two-dimensional synthetic jets. Smith and Swift[64] argued that a threshold stroke length L_0/D exists for jet formation. On the other hand, Rampunggoon[65]used a simple order-of-magnitude analysis to show that the ratio of the Reynolds number to the square of the Stokes number must be greater than some constant to ensure jet formation.

The order-of-magnitude analysis is summarized next.

Figure A1 illustrates a vortex ring emanating from a slot (or orifice). The ability of the ring to overcome the suction velocity during the ingestion stroke depends on its self-induced velocity, which in turn is a function of the vortex strength. The strength of each shed vortex has been shown by Didden[66] to be related to the flux of vorticity through a (x, y) planar slice of the half-slot during the ejection phase of the cycle.

$$\int_0^{T/2} \int_0^{D/2} \xi_z(y,t) u(y,t) dy dt \tag{6}$$

Where $\xi_z(y, t)$ is the spanwise (or azimuthal) vorticity component at the exit for a two dimensional (or axisymmetric) case and u(y, t) is the exit jet x velocity. In Figure 1, δ_s is the size of the shear flow region characterized by nonzero vorticity. The induced velocity of the dipole V_I is thus proportional to Ω_v/d, where d is the slot width.

An order-of-magnitude analysis of Eq. (6) results in

$$\Omega_v \sim \left(\frac{\bar{U}}{\delta_s}\right) \overline{U}\, \delta_s \left(\frac{1}{\omega}\right) \sim \bar{U}^2/\omega \tag{7}$$

If it is assumed that a jet will form when the induced velocity of the dipole V_I is somewhat larger than the average jet suction velocity $V_s \sim \bar{U}$, it follows that the ratio of the induced dipole velocity to the suction velocity is

$$V_I/V_s \sim \frac{(\Omega_v/d)}{\overline{U}} \sim \overline{U}/\omega d = 1/sr = \frac{d\overline{U}/\upsilon}{\frac{\omega d^2}{\upsilon}} = \frac{Re}{S^2} > K \quad (8)$$

where K is an O(1) constant.

Equation (8) states that a vortex escapes or a jet is formed when the Strouhal number is below a critical value.

The data support the jet formation criterion $1/Sr = Re/S^2 > K$, where the constant K is approximately 1 and 0.16 for two-dimensional and axisymmetric synthetic jets, respectively.

APPENDIX B

PIV Post Processing Procedure

Digital particle image velocimetry (DPIV) is a non-intrusive analysis technique that is very popular for mapping flows quantitatively. To get accurate results, in particular in complex flow fields, a number of challenges have to be faced and solved: The quality of the flow measurements is affected by computational details such as image pre-conditioning, sub-pixel peak estimators, data validation procedures, inter- polation algorithms and smoothing methods[47,48]. In this study we used GUI-based open-source tool (PIVlab)[48] for DPIV analyses in MATLAB (MathWorks, Natick, Massachusetts) is presented. The tool takes advantage of several built-in MATLAB features, and eases subsequent data processing by providing a close link to the popular MATLAB user interface.

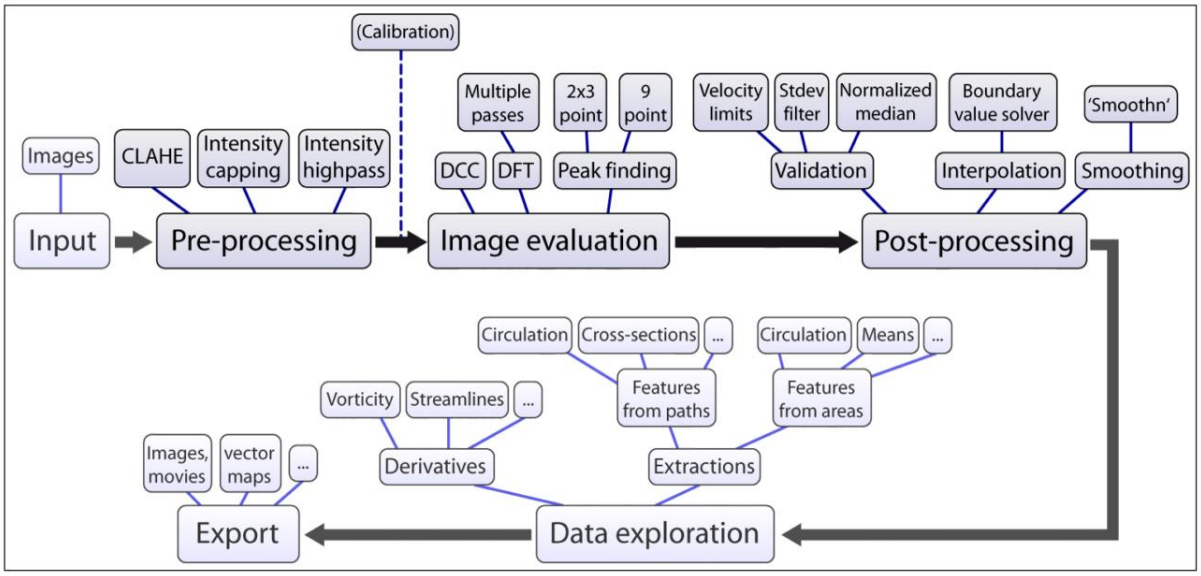

Figure B1.DPIV analyses in PIVlab. Overview of the workflow and the implemented features.

A DPIV analysis typically consists of three main steps (image pre-processing, image evaluation, post-processing, see Figure B1). All of these steps are accessible from the GUI of PIVlab. The workflow is menu-based, starting at the left with image input and pre-processing

options, and then continuing to the right of the menu (image evaluation / PIV analysis, post-processing, data exploration).

In this study for free and impinging synthetic jet we used the flowing options:

1. Pre-processing

- Contrast limited adaptive histogram equalization (CLAHE) used to increase the readability of image data.
- Inhomogeneous lighting can cause low frequency back- ground information which can be removed by applying a high-pass filter that mostly conserves the high frequency information from the particle illumination
- The DPIV method assumes that all particles within an interrogation window have the same motion. This will not be the case in reality, as perfectly uniform flow does hardly exist. Bright particles or bright spots within the area will contribute statistically more to the correlation signal, which may bias the result in non-uniform flows.The intensity capping filter circumvents this problem.

2. Image evaluation

The most sensitive part of a DPIV analysis is the cross correlation algorithm: Small sub images (interrogation areas) of an image pair are cross correlated to derive the most probable particle displacement in the interrogation areas.

In this part we used DFT with multiple passes.

3. Post processing

Post processing of DPIV data is generally required to obtain reliable results .In this section due to sharp velocity changes for impinging jet cases we only used velocity limits filter.

After the removal of outliers, missing vectors should be replaced by interpolated data.In this regards we used interpolation based on boundary value solver.

APPENDIX C

UNCERTAINTY ANALYSIS

Reliability of an experimental study relies on the repeatability and low uncertainty. Therefore, over the last three decades researchers have given an increasing amount of attention so more reliable data has been generated. In 1988, Moffat [45] mentioned that experimental data will not be accepted without mentioning the uncertainty involves in the experiments. Uncertainty analysis is not only essential in writing experimental data but also more useful to point out the possible cradles of residual error at the first stage of an experiment build-up. A number of sample analyses was collected and described different parameters. Equation (1) and (2) presents the same equation mentioned by the Moffat for Nu and Re numbers.

$$\delta Nu = \left[(a_1\delta Q_s)^2 + (a_2\delta D)^2 + (a_3\delta A_s)^2 + \left(a_4\delta(T_s - T_{amb})\right)^2 + (a_5\delta k)\right]^{\frac{1}{2}} \quad (1)$$

$$\delta Re = [(b_1\delta\rho)^2 + (b_2\delta U)^2 + (b_3\delta D)^2 + (b_4\delta\mu)^2]^{\frac{1}{2}} \quad (2)$$

Where a_i(i=1…5) and b_j(j=1…4) are the sensitivity coefficients as shown in equation (1) and (2). δ shows the uncertainty in front of corresponding variable in equation (1) and (2). Major sources of uncertainty for the experiments were identified as the heat losses through the heater holder, temperature measurements and heater power measurements. A set of separate heat loss experiments was performed for the heater to quantify the heat losses through the substrate using guard heater. Table C1 is enlisted with the calculated sensitivity coefficient for the equation (1) and (2). In the current study, RMS (root mean square) method is used to analyze the uncertainty in the experiments.

Table C1: The sensitivity coefficient given in equation (1) and (2)

Sensitive coefficient	Value	Sensitive coefficient	Value
a_1	$\frac{d}{A_s(T_s - T_{amb})k}$	b_1	$\frac{Vd}{\mu}$
a_2	$Nu = \frac{Q_s}{A_s(T_s - T_{amb})k}$	b_2	$\frac{\rho d}{\mu}$
a_3	$-\frac{Q_s d}{{A_s}^2(T_s - T_{amb})k}$	b_3	$\frac{\rho U}{\mu}$
a_4	$-\frac{Q_s d}{A_s(T_s - T_{amb})^2 k}$	b_4	$-\frac{\rho V d}{\mu^2}$
a_5	$-\frac{Q_s d}{A_s(T_s - T_{amb})^2 k^2}$		

The final calculated quantities are Nu and Re numbers for the current heat transfer study. In Nu number two different types of uncertainties are possible;

- Uncertainty propagated from the measured primary variables.
- Uncertainty including the effect of all variable mentioned by Moffat [45].

Propagation of uncertainty is measured using the RMS method using the uncertainty in the primary measured variables listed in Table C2. The values of uncertainty are taken from the least value that can be measured from the equipment. For current study, it is assumed that values of air properties like density, conductivity and viscosity are fixed.

Table C2: The uncertainty and the range of the primary variables measured

Primary variables	Absolute uncertainty	Relative uncertainty
$T_{Thermocouple}$ (K)	±0.1	-
Current(A)	±0.001	-
Voltage(V)	±0.01	-
Density(kg/m^3)	Fixed value (1.225)	-
Air conductivity (W/m-K)	Fixed value (0.0257)	-
Air viscosity(Pa.s)	Fixed value	-
Velocity(m/s)	-	2%
Length, Width, Diameter(mm)	±0.01	

Second type of uncertainty is measured by repeating the experiment several times for different operating conditions. Table shows some of the experimental sampling that had been made in order to calculate the standard deviation and error (%) in Nu number.

Table C3: Experimental results and (%) error in measured Nu numbers

Hz,mm,Volts	Test 1	Test 2	Test 3	Test 4	Standard Deviation	%Error
0,10,20	11.22	10.90	12.27	11.36	0.58	5.15
100,10,20	17.41	14.21	15.37	18.90	0.99	5.62
200,10,20	26.57	26.44	25.69	28.31	1.10	4.14
300,10,20	51.79	54.34	56.93	54.85	2.11	3.87
400,10,20	85.05	84.86	87.24	84.31	1.28	1.50
500,10,20	80.77	80.14	80.68	81.75	0.67	0.83
600,10,20	46.47	44.62	50.06	46.62	2.27	4.83
700,10,20	31.15	33.42	33.22	30.33	1.53	4.78
800,10,20	20.22	22.02	19.83	21.72	1.08	5.18

The maximum error found related using standard deviation method is 5.2%, while error from uncertainty propagation is 4.6%. Error calculated from sampling is greater than uncertainty propagation which is why uncertainty in heat transfer using standard deviation is greater that is why 5.2% experimental uncertainty is taken as our uncertainty. Propagation of uncertainty is also included in the uncertainty calculated by the sampling. Similarly in Re number the measured variables are diameter of the orifice and velocity. It is mentioned by the manufacturer that there is 2% uncertainty in velocity measurements and maximum uncertainty found in Re number is around 4%.

REFERENCES

[1] Garg, J., Arik, M., Weaver, S., Wetzel, T., and Saddoughi, S., 2005, "Meso Scale Pulsating Jets for Electronics Cooling," J. Electron. Packag., 127(4), p. 503.

[2] Ghaffari, O., Ikhlaq, M., and Arik, M., 2015, "An Experimental Study of Impinging Synthetic Jets for Heat Transfer Augmentation," Int. J. Air-Conditioning Refrig., 23(3), p. 1550024.

[3] Mahalingam, R., Rumigny, N., and Glezer, A., 2004, "Thermal Management Using Synthetic Jet Ejectors," IEEE Trans. Components Packag. Technol., 27(3), pp. 439–444.

[4] He, X., Lustbader, J. A., Arik, M., and Sharma, R., 2015, "Heat transfer characteristics of impinging steady and synthetic jets over vertical flat surface," Int. J. Heat Mass Transf., 80, pp. 825–834.

[5] Holman, R., Utturkar, Y., and Smith, B. L., 2005, "Formation Criterion for Synthetic Jets," 43(10).

[6] Albright, S. O., and Solovitz, S. A., 2014, "Development of a Variable Diameter Synthetic Jet Actuator," Volume 1: Advances in Aerospace Technology, ASME, p. V001T01A002.

[7] Mohseni, K., 2006, "Pulsatile vortex generators for low-speed maneuvering of small underwater vehicles," Ocean Eng., 33(16), pp. 2209–2223.

[8] Mittal, R., and Rampunggoon, P., 2002, "On the virtual aeroshaping effect of synthetic jets," Phys. Fluids, 14(4), p. 1533.

[9] Lardeau, S., and Leschziner, M. A., 2011, “The interaction of round synthetic jets with a turbulent boundary layer separating from a rounded ramp,” J. Fluid Mech., 683, pp. 172–211.

[10] Ghaffari, O., Dogruoz, M. B., and Arik, M., 2014, “An investigation into momentum and temperature fields of a meso-scale synthetic jet,” Fourteenth Intersociety Conference on Thermal and Thermomechanical Phenomena in Electronic Systems (ITherm), IEEE, pp. 889–896.

[11] Gillespie, M. B., Black, W. Z., Rinehart, C., and Glezer, A., 2006, “Local Convective Heat Transfer From a Constant Heat Flux Flat Plate Cooled by Synthetic Air Jets,” J. Heat Transfer, 128(10), p. 990.

[12] Pavlova, A., and Amitay, M., 2006, “Electronic Cooling Using Synthetic Jet Impingement,” J. Heat Transfer, 128(9), p. 897.

[13] Persoons, T., McGuinn, A., and Murray, D. B., 2011, “A general correlation for the stagnation point Nusselt number of an axisymmetric impinging synthetic jet,” Int. J. Heat Mass Transf., 54(17-18), pp. 3900–3908.

[14] Fang, R., and Khan, J. A., 2013, “Active Heat Transfer Enhancement in Single-Phase Microchannels by Using Synthetic Jets,” J. Therm. Sci. Eng. Appl., 5(1), p. 011006.

[15] Yu, Y., Simon, T. W., Zhang, M., Yeom, T., North, M. T., and Cui, T., 2014, “Enhancing heat transfer in air-cooled heat sinks using piezoelectrically-driven agitators and synthetic jets,” Int. J. Heat Mass Transf., 68, pp. 184–193.

[16] Smith, B. L., and Glezer, A., 1998, “The formation and evolution of synthetic jets,” Phys. Fluids, 10(9), pp. 2281–2297.

[17] Ghaffari, O., Dogruoz, M. B., and Arik, M., 2014, “An Investigation into Momentum and Temperature Fields of a Meso-Scale Slot Synthetic Jet for a Small Jet-to-Surface

Spacing," Proceedings of the 15th International Heat Transfer Conference, Begellhouse, Kyoto,Japan.

[18] Silva, L. A., and Ortega, A., 2013, "Convective Heat Transfer in an Impinging Synthetic Jet: A Numerical Investigation of a Canonical Geometry," J. Heat Transfer, 135(8), p. 082201.

[19] Martin, H., 1977, "Heat and Mass Transfer Between Impinging Gas Jets and Solid Surfaces," Adv. Heat Transf. Acad. Press. New York, 13, pp. 1–60.

[20] Smith, B. L., and Swift, G. W., 2003, "A comparison between synthetic jets and continuous jets," Exp. Fluids, 34, pp. 467–472.

[21] Krishnan, G., and Mohseni, K., 2010, "An experimental study of a radial wall jet formed by the normal impingement of a round synthetic jet," Eur. J. Mech. - B/Fluids, 29(4), pp. 269–277.

[22] Krishnan, G., and Mohseni, K., 2009, "An Experimental and Analytical Investigation of Rectangular Synthetic Jets," J. Fluids Eng., 131(12), p. 121101.

[23] Yassour, Y., Stricker, J., and Wolfshtein, M., 1986, "Heat Transfer from a Pulsating Jet," Proceedings of the Eighth International Conference, San Francisco, CA, Aug. 17–22, Vol. 3, pp. 1183–1186, pp. 1183–1186.

[24] Gutmark, E., Yassour, Y., and Wolfshtein, M., 19825, "Acoustic Enhancement of Heat Transfer in Plane Channels," Proceedings of the Seventh International Heat Transfer Conference, Munich, Germany, Sep. 6–10, pp. 441–445.

[25] Minichiello, A. L., Hartley, J. G., Glezer, A., and Black, W. Z., 1997, "Thermal Management of Sealed Electronic Enclosures Using Synthetic Jet Technology," Adv. Electron. Packag, 19(2), pp. 1809–1812.

[26] Arik, M., and Utturkar, Y. V, 2014, "A Computational and Experimental Investigation of Synthetic Jets for Cooling of Electronics," ASME J. Electron. Packag.

[27] Xu, Y., and Feng, L., 2013, "Influence of orifice-to-wall distance on synthetic jet vortex rings impinging on a fixed wall," Sci. China Technol. Sci., 56(7), pp. 1798–1806.

[28] Valiorgue, P., Persoons, T., McGuinn, A., and Murray, D. B., 2009, "Heat transfer mechanisms in an impinging synthetic jet for a small jet-to-surface spacing," Exp. Therm. Fluid Sci., 33(4), pp. 597–603.

[29] Jalilvand, A., Mochizuki, M., Singh, R., Saito, Y., Kawahara, Y., and Wuttijumnong, V., 2014, "Air Impingement Cooling by Synthetic Jet," J. Therm. Sci. Eng. Appl., 6(3), p. 031008.

[30] Chaudhari, M., Puranik, B., and Agrawal, A., 2010, "Effect of orifice shape in synthetic jet based impingement cooling," Exp. Therm. Fluid Sci., 34(2), pp. 246–256.

[31] Ghaffari, O., Dogruoz, M. B., and Arik, M., 2014, "An Investigation into Momentum and Temperature Fields of a Meso-Scale Synthetic Jet," IEEE Intersociety Conference on Thermal and Thermomechanical Phenomena in Electronic Systems (ITherm), Orlando, FL, USA.

[32] Ikhlaq, M., Ghaffari, O., and Arik, M., 2014, "Effect of actuator deflection on heat transfer for low and high frequency synthetic jets," Thermal and Thermomechanical Phenomena in Electronic Systems (ITherm), 2014 IEEE, Orlando, FL, USA, pp. 882–888.

[33] Lasance, C. J. M., Aarts, R. M., and Ouweltjes, O., 2008, "Synthetic jet cooling part II: Experimental results of an acoustic dipole cooler," Annu. IEEE Semicond. Therm. Meas. Manag. Symp., pp. 26–31.

[34] Arik, M., 2007, "An investigation into feasibility of impingement heat transfer and acoustic abatement of meso scale synthetic jets," Appl. Therm. Eng., 27, pp. 1483–1494.

[35] Jabbal, M., and Kykkotis, S., 2014, “Towards the Noise Reduction of Piezoelectrical-Driven Synthetic Jet Actuators,” 32nd AIAA Applied Aerodynamics Conference,16-20 June 2014, Atlanta, GA, pp. 1–21.

[36] Kurihara, K., 2013, “United States Patent Fujisaki et al. Patent N0.: (45) Date of Patent: US 8,596,998 B2 Dec. 3, 2013,” 2013,” 2(12).

[37] Fukue, T., Matsuura, Y., Hirose, K., and Terao, H., 2014, “Evaluation of cooling performance of a piezoelectric micro blower in narrow flow passage,” 2014 Int. Conf. Electron. Packag., pp. 69–73.

[38] Fukue, T., Hirose, K., Matsuura, Y., and Terao, H., 2013, “Effects of obstruction in front of a piezoelectric micro blower on performance characteristics,” Ieee, pp. 0–3.

[39] Blevins, R. D., 1995, Formulas for Natural Frequency and Mode Shape, Krieger, Florida.

[40] Eastep, F. E., and Hemmig, F. G., 1982, “Natural frequencies of circular plates with partially free, partially clamped edges,” J. Sound Vib., 84(3), pp. 359–370.

[41] 2012, ANSYS, User’s Guide, Icepak. 14.5., Canonsburg, PA.

[42] Habibi, K., Amiri, S., and Ashjaee, M., 2010, “Characterization of thermal field in mixed-convection cooling of a flat plate by an impinging slot jet,” 2010 12th IEEE Intersociety Conference on Thermal and Thermomechanical Phenomena in Electronic Systems, IEEE, pp. 1–10.

[43] Habibi, K., Amiri, S., and Ashjaee, M., 2013, “Study of mixed convection characteristics of confined planar jet impingement using the direct temperature gradient interferometric method,” Int. J. Therm. Sci., 71, pp. 205–215.

[44] Zuckerman, N., and Lior, N., 2006, “Jet Impingement Heat Transfer : Physics , Correlations , and Numerical Modeling,” 39(06), pp. 565–631.

[45] Moffat, R. J., 1988, “Describing the uncertainties in experimental results,” Exp. Therm. Fluid Sci., 1(1), pp. 3–17.

[46] 2010, IFA 300 Constant Temperature Anemometer System Operation Manual, TSI Incorporated.

[47] Raffel, M., Willert, C. E., and Kompenhans, J., 1998, Particle Image Velocimetry: A Practical Guide, Springer,Berlin.

[48] Thielicke, W., and Stamhuis, E. J., 2014, “PIVlab – Towards User-friendly, Affordable and Accurate Digital Particle Image Velocimetry in MATLAB,” J. Open Res. Softw., 2.

[49] Glauert, M. B., 1956, “The wall Jet,” J. Fluid Mech., 1(6), pp. 625–643.

[50] Wygnanski. I, Y. K. and E. H., 1992, “On the applicability of various scaling laws to the turbulent wall jet,” J. Fluid Mech., 234, pp. 669–690.

[51] Tesař, V., and Kordík, J., 2011, “Spectral analysis of a synthetic jet,” Sensors Actuators A Phys., 167(2), pp. 213–225.

[52] Solovitz, S. A., and Arik, M., 2011, “System-Level Metrics for Thermal Management Technology,” J. Therm. Sci. Eng. Appl., 3(3), p. 031009.

[53] Jagannatha, D., Narayanaswamy, R., and Chandratilleke, T. T., 2009, “Analysis of a Synthetic Jet-Based Electronic Cooling Module,” Numer. Heat Transf. Part A Appl., 56(3), pp. 211–229.

[54] Jain, M., Puranik, B., and Agrawal, A., 2011, “A numerical investigation of effects of cavity and orifice parameters on the characteristics of a synthetic jet flow,” Sensors Actuators A Phys., 165(2), pp. 351–366.

[55] Navaratnam, K., Lee, D.-D., and Parameswaran, S., 2006, “Application of a Novel Moving-Grid Methodology to Model the Interaction of a Synthetic Jet with a Turbulent Boundary Layer,” Numer. Heat Transf. Part B Fundam., 49(2), pp. 105–123.

[56] 2012, ANSYS, User’s Guide, CFX v. 14.5., Canonsburg, PA.

[57] Ferziger, Joel H., Peric, M., 2002, Computational Methods for Fluid Dynamics, Springer,Berlin.

[58] Hussein, H. J., Capp, S. P., and George, W. K., 2006, “Velocity measurements in a high-Reynolds-number, momentum-conserving, axisymmetric, turbulent jet,” J. Fluid Mech., 258(-1), p. 31.

[59] Pope, S. B., 2000, Turbulent Flows, Cambrige university press.

[60] J. Mi , P. Kalt , G. J. Nathan, C. Y. W., 2007, “PIV measurements of a turbulent jet issuing from round sharp-edged plate,” Exp. Fluids, 42, pp. 625–637.

[61] Fukue, T., Hirose, K., and Terao, H., 2015, “Cooling performance of impinging jet from piezoelectric micro blower mounted in narrow flow passage,” 2015 Int. Conf. Electron. Packag. iMAPS All Asia Conf., pp. 605–610.

[62] Wen, M., and Jang, K., 2003, “An impingement cooling on a flat surface by using circular jet with longitudinal swirling strips,” Int. J. Heat Mass Transf., 46, pp. 4657–4667.

[63] Ikhlaq, Muhammad.Ghaffari, omidreza., A. mehmet, 2016, “Predicting Heat Transfer for Low and High Frequency Central Orifice Synthetic Jets,” IEEE Trans. Components .Packaging IEEE Components, Packag. Manuf. Technol.

[64] Smith, B., and Swift, G., “Synthetic Jets at Large Reynolds Number and Comparison to Continuous Jets,” AIAA, pp. 2001–3030.

[65] Rampunggoon, P., Interaction of a Synthetic Jet with a Flat Plate Boundary Layer, Ph.D. Dissertation, Dept. of Mechanical Engineering, Univ. of Florida, Gainesville, FL,.

[66] Didden, N., “On the Formation ofVortex Rings: Rolling-Up and Production of Circulation,” J. Appl. Math. Physics, 30, pp. 101–116.

VITA

Omidreza Ghaffari received his high school diploma from NODET at Shiraz (Shiraz is historical city located in the southwest of Iran.). He won the 3rd prize of 5th National Khwarizmi Festival (Highest experimental competition in Iran) in the field of applied physics.

He graduated from IAU Shiraz as a first rank bachelor student. He received the M.S. degree in mechanical engineering from the University of Sistan and Baluchestan, Zahedan, Iran, in 2011.His master thesis was awarded by Iran Nanotechnology Initiative Council.

Currently pursuing the Ph.D. degree with the Department of Mechanical Engineering, Özyegin University, Istanbul, Turkey. He joined Özyegin University in 2012. His previous research interests included turbulent mixed convection of Nanofluids. His current research interests include experimental heat transfer and fluid dynamics for advanced cooling of electronics. He published five journal and seven conference papers and two journal papers are pending.

Mr. Ghaffari serves as a reviewer of the ASME Journal of Electronics Packaging.